DMS – RE 2011

The twenty-first joint seminar

DEVELOPMENT

OF MATERIALS SCIENCE

IN RESEARCH AND

EDUCATION

PROCEEDINGS OF THE 21th JOINT SEMINAR

August 29 - September 2, 2011

Kežmarské Žľaby

DMS – RE 2011

The twenty-first joint seminar

DEVELOPMENT OF MATERIALS SCIENCE IN RESEARCH AND EDUCATION

August 29 – September 2, 2011

K e ž m a r s k é Ž ľ a b y

Organized by

Slovak Expert Group of Solid State Chemistry and Physics
Czechoslovak Association for Crystal Growth
Faculty of Chemical and Food Technology STU
Faculty of Materials Science and Technology STU
Crystallographic Society
Slovak Society for Industrial Chemistry
Regional Committee of Czech and Slovak Crystallographers

Sponsors of **DMS-RE 2011**

Slovak Society for Industrial Chemistry
Koceľová 15, 815 94 Bratislava, Slovak Republic

ROFA Slovensko, spol. s. r. o.
Vlčie hrdlo, P.O. Box 16, 820 03 Bratislava, Slovak Republic

ITES Vranov, s. r. o.
Čemernianska 137
093 03 Vranov nad Topľou, Slovak Republic

Anamet Slovakia s.r.o. instruments for material testing
1.mája 29, 900 01 Modra, Slovak Republic

Rigaku Innovative Technologies Europe s.r.o.
Novodvorska 994, 142 21 Praha 4, Czech Republic

ISSBN 978-80-8134-002-4

GUARANTEES

Prof. Ing. Marian Koman, DrSc., STU Bratislava

Ing. Karel Nitsch, PhD., Institute of Physics AS CR, Prague

PROGRAM COMMITTEE

M. Koman (chairman)

M. Behúlová

M. Rodová

ORGANIZING COMMITTEE

B. Papánková (chairman)

M. Behúlová

M. Koman

V. Jorík

Secretary

Ľ. Dlháň

Department of Inorganic Chemistry, FCHPT STU Bratislava

e-mail: lubor.dlhan@stuba.sk

Editors

M. Koman

V. Jorík

FOREWORD

The seminar "Development of Materials Science in Research and Education" is already the twenty-first in the series started at Gabčíkovo in 1991 by the initiative of the Czechoslovak Association for Crystal Growth and the Slovak Expert Group of Solid State Chemistry and Physics.

The objective of this meeting is to offer an opportunity to Czech and Slovak teachers and scientists as well as guests from other countries who are working in the field of Materials Science to present their recent results and experience and to exchange new ideas and information.

The scientific session will cover the following topics on materials science:

- Trends in development of material research
- Education in materials science at the universities
- Information on research program of individual institutions
- Information on equipments for preparation and characterization of materials
- Results of materials science research

This workshop is aimed at creation of a stimulating atmosphere of cooperation and at the support of patient dissemination of scientific ideas and propagation of materials science in education.

M. Koman and V. Jorík

CONTENTS

FRACTAL GROWTH IN COMPARISON WITH CRYSTAL GROWTH

V. Bouda and D. Puncman

Faculty of Electrical Engineering, Czech Technical University in Prague, Technická 2, 166 27 Praha, Czech Republic

The aim of our research is the development of the new processing technologies of composite materials. The topical issue is a theoretical and experimental research of directed self-organization of functional nanoparticles imbedded in polymeric or silicate matrix (e.g. electrically conductive composite materials or some complex materials inspired by nature). We are studying the formation of internal functional networks of nano-particles by the mechanism of their diffusion limited aggregation (DLA). Structure and mechanism of fractal growth by DLA will be described in comparison with crystal growth. Figure 1 describes the mechanism of fractal growth by DLA preferentially on its tips. The surroundings of the tip is influenced by the electrical field concentration that induces relatively very high ionic concentration. The van der Waals attraction overcomes in this locality the electrostatic repulsion and the particles are trapped. The effective concentration of building blocks trapped on the surface is zero because the trapped particles lose their heat vibration and ability of diffusion. In the tip surroundings, the gradient of concentration dc/dx and the diffusion flux $j = -D\ (dc/dx)$ reach maximum. The growth mechanism explains in details recent colloidal diagrams.

Although there are countless technology applications for self-assembled structures comprised of individual nanoparticle building blocks, the mechanism behind self-assembly is not so clear. However, directed self-assembly typically occurs when a stable system is pushed from equilibrium by an external factor, such as the change of local electrical field, ionic concentration, temperature or combination of these factors.

Original method of the new 3-D state diagram (Figure 2) computation of the system of nano-particles in vapor (V), liquid (L), and solid (S) states, respectively, will be presented. It is based on the calculations of the extremes of interaction energy between particles energy (the sum of electrostatic repulsion and van der Waals attraction energies) for various kinds of particles with various surface charges, various matrix compositions and their properties, and various temperatures. The three coordinates are the bulk concentration of ions in the liquid matrix (x), the electrical potential on the surface double layer of particles (y), and the temperature of the system (z). The state diagrams provide the research and technological tool to control the directed self-organization of internal structure of any system, whether the system is made of nano- or microscopic objects or molecular species like polymers, DNA and proteins. As examples, three applications of the state diagram will be presented [1,2].

References:

[1] V. Bouda, ASME Int. Mechanical Engineering Congress 1997 Dallas, TX, Proceedings: CAE and Intelligent Processing of Polymeric Materials, p.281-298, ASME 1997

[2] Bouda, V. Boudová, L. Haluzíková, D.: Biomimetic Actuator. In Proceedings of SPIE, Smart Structures and Materials 2005-Electroactive Polymer Actuators and Devices. Bellingham, 2005, The International Society for Optical Engineering, p. 340 – 351.,

The Research Scheme of Czech Technical University in Prague MSM Project "Diagnostics of Materials No. 210000021 gave their support to this work.

Figure 1. Growth of Fractal by Diffusion Limited Aggregation (DLA)

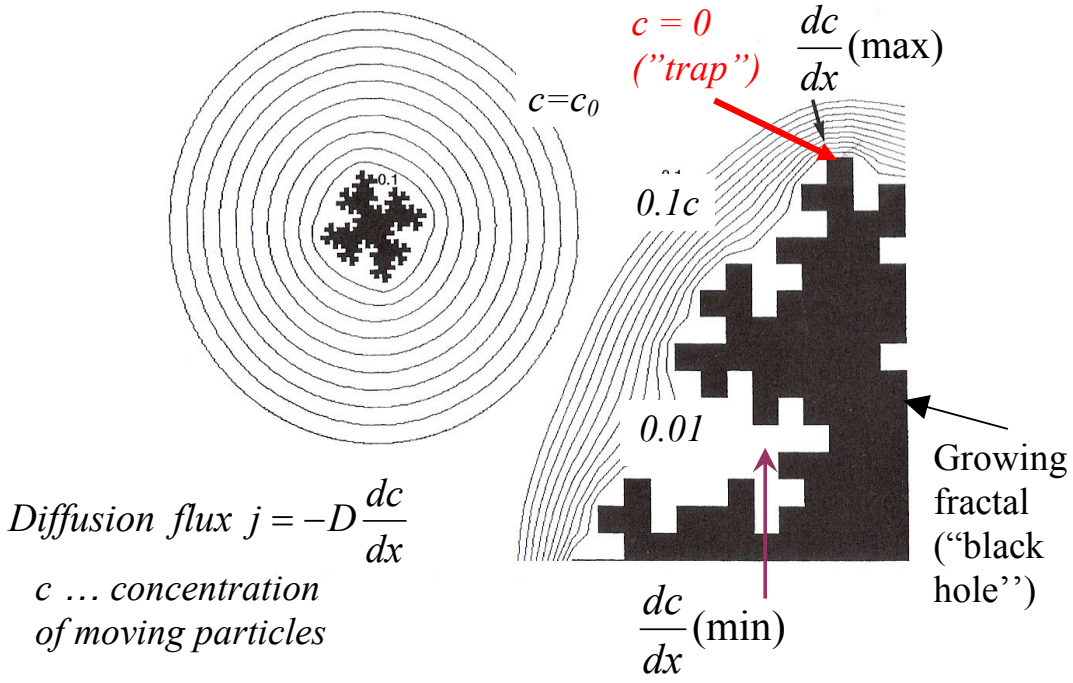

Figure 2 Colloidal phase diagram

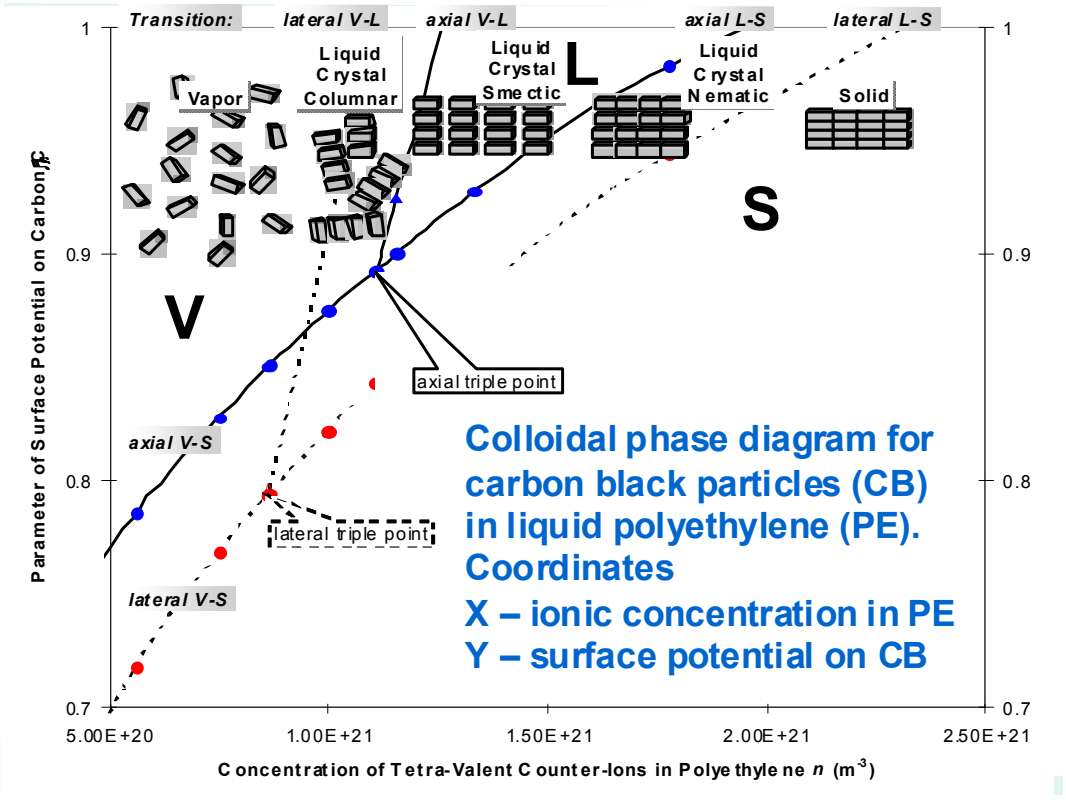

STABILISATION OF METALLIC NANOPARTICLES

Z. Bureš and M. Vlček

Faculty of Chemical Technology, University of Pardubice, 532 10 Pardubice, Czech Republic

Nanoscale particles, since they have large surface areas, can easily agglomerate to form either small clusters or larger particles to minimize the total surface or interfacial energy of the whole system. Agglomeration of fine particles can occur either during their synthesis, or during their drying as well as during subsequent processing of the particles. Thus particles must be protected against unwanted agglomeration at each step of their production and powder processing. Van der Waals attractive force and/or the driving force that tends to minimize the total surface energy of the system are responsible for agglomeration of fine particles. It is necessary to ensure repulsive interparticle forces to prevent the agglomeration of these particles. It is well known that there are in principle two basic methods commonly used, namely, electrostatic and steric stabilization (Fig. 1) [1].

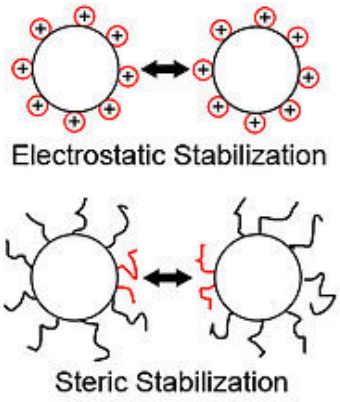

Fig. 1 *Electrostatic and steric stabilisation*[2]

The most frequently used are the waterbased methods due to well known ability of water to solubilize a variety of ions as well as to stabilize molecules. Various polymers, surfactants, and coordinative ligands, which are able to protect the nanoparticles from their agglomeration, to acquire highly stable and well-dispersed metal nanoparticles, are mainly used as stabilizers in waterbased methods.[1,3]

Nanometal particles such as gold - Au and silver - Ag have recognized big importance in chemistry, physics, biology and medecine due to their unique optical, electrical, magnetic and photothermal properties. These nanoparticles have potential applications in analytical chemistry and have been used in surface enhanced Raman scattering, as probes in mass spectroscopy, as well as in the detection for proteins and DNA molecules. Besides other nanoparticles they can have applications in catalysis, as well as antistatic and antibacterial materials, or as a cryogenic superconducting materials [1,3].

The strong optical extinctions of conductive metal nanoparticles arise from an electrodynamic phenomenon known as surface plasmons, which are generated by the collective excitation of free electrons in response to a characteristic electromagnetic frequency. From the shape of absorption bands, the size of prepared metal nanoparticles can

be determined and from time dependence changes of this spectra stability of metal nanoparticles can be checked.

Silver and gold nanoparticles were prepared by direct reduction of silver nitrate $AgNO_3$ respectively tetrachloroauric acid $H[AuCl_4]$ in aqueous solutions using various types of reductants. For silver-nanoparticles synthesis, sodiumborohydride $Na[BH_4]$, sodium citrate, ascorbic acid, gallic acid were used as reducing agents. Gold-nanoparticles were prepared by using two methods (i) reduction of tetrachloroauric acid by sodium citrate at elevated temperature (100°C); (ii) reduction by ascorbic and/or gallic acid at room temperature.

Prepared colloids of nanometall particles were stabilised using different stabilisers. Polyvinylpyrrolidone, polyvinylalcohol, polyethylene glycol, tween 20, agar-agar were used as sterical stabilisers. Sodium chloride as electrostatic stabiliser. The obtained nanoparticles were characterized by position and intensity of plasmonic resonance band in absorption spectra of prepared colloids (Fig. 2).

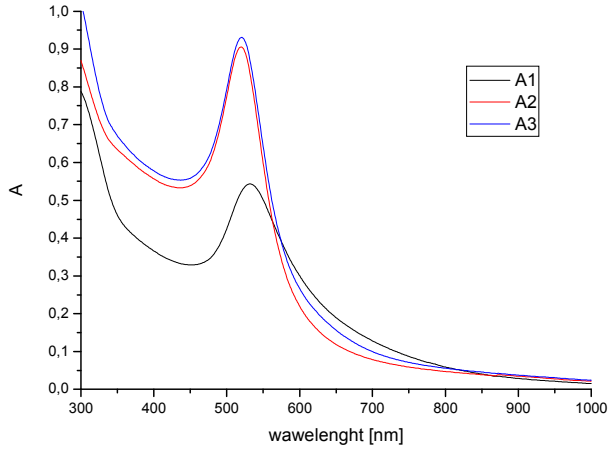

Fig. 2 *Absorption spectra of unstabilised silver nanoparticles, prepared by reduction using ascorbic acid (increasing concentration A1-A3)*

Suitable method for synthesis of high stable Ag-nanoparticles was found method using sodium borohydride as reductive agent with consequent stabilisation by PVP+NaCl mixture. For synthesis of long term stabile colloidal Au-nanoparticles can be successively applied method starting from tetrachloroauric acid which is reduced by ascorbic acid. For stabilisation of this colloid either PVP or Tween 20 are the best from all studied stabilisers.

This work was supported by the grant P204/11/0832 from the Czech Science Foundation and by the grant 0021627501 from the Czech Ministry of Education, Youth and Sports.

[1] Guangyin Lei, Synthesis of Nano-Silver Colloids and Their Antimicrobial Effects, Diploma thesis, Virginia Polytechnic Institute and State University, (2007).

[2] http://en.wikipedia.org/wiki/Polyelectrolyte_adsorption

[3] M. M. Kemp, A. Kumar, S. Mousa et al., Synthesis of Gold and Silver Nanoparticles Stabilized with Glycosaminoglycans Having Distinctive Biological Activities, Biomacromolecules (2009), 10, 589–595.

SQUID MAGNETIC STUDIES OF BASAL GANGLIA EXTRACTED FROM HUMAN BRAIN

Ľ. Dlháň [(a)], R. Boča [(a)], M. Kopány [(b)]

(a) Institute of Inorganic Chemistry (FCHPT), Slovak University of Technology, 812 37 Bratislava, Slovakia
(b) Institute of Pathology, Faculty of Medicine, Commenius University, Bratislava, Slovakia

The *basal ganglia* play an important role in neurological dysfunctions, among which the Parkinson's disease is the most notable. An accumulation of nanoparticles of iron(III)-oxide minerals is well documented at present [1].

The samples were extracted from the *basal ganglia* of human brain of nine donors of different age and sex. They were dried under vacuum and weighted into the gelatin-made containers (ca 20 mg). For magnetization studies the SQUID apparatus has been used (MPMS-XL7, Quantum Design) in the RSO mode of the detection.

The samples can be classified into three classes when inspecting the χT product function: the dominating paramagnetism – class I, the dominating diamagnetism with a paramagnetic admixture paramagnetism – class III, and the intermediate behavior – class II.

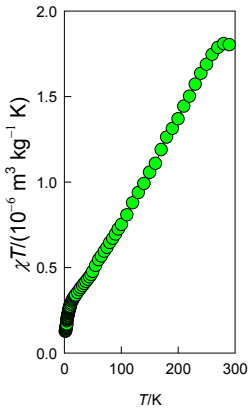

Class I

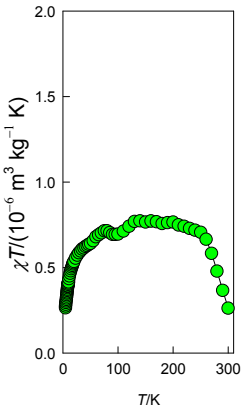

Class II

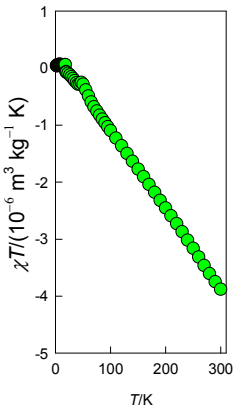

Class III

The magnetization studies for a number of samples revealed that the magnetic hysteresis occurs at the low temperature and this survives until the room temperature. However, the hysteresis loop shows a rather unusual form.

The field-cooled magnetization and zero-field-cooled magnetization curves intercept at the room temperature indicating that the ordering temperature lies above the room temperature.

In addition to bulk diamagnetism due to the tissues, a ferromagnetic impurity is present (probably maghemite and/or magnetite).

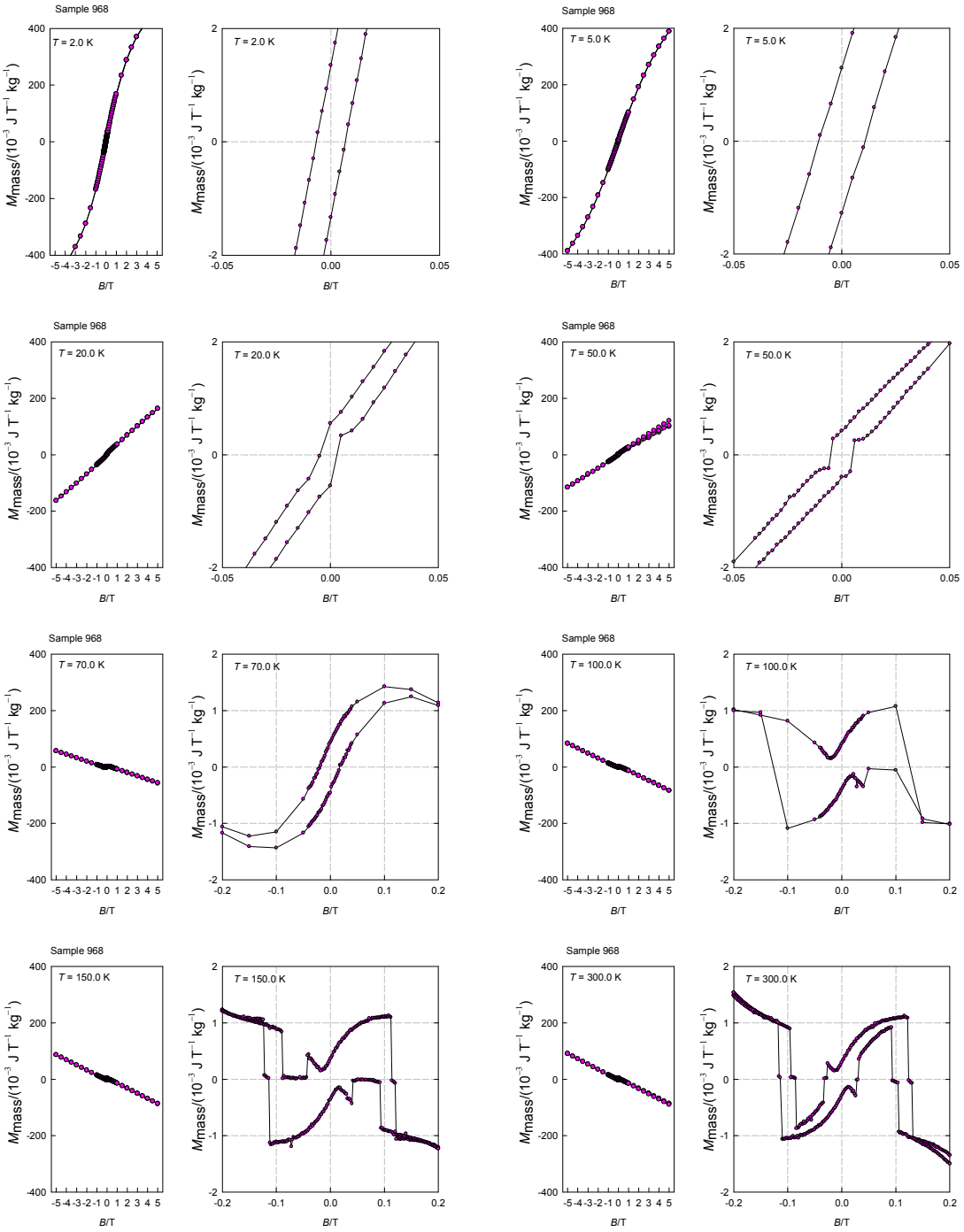

Grant agencies are acknowledged for the financial support: VVCE 0004 07 and VEGA 1/0052/11.

[1] J.L. Kirschvink, A. Kobayashi-Kirschvink, B.J. Woodford, Proc. Natl. Acad. Sci. USA, 89 (1992) 7683.

DATA STORAGE - CURRENT AND APPROACHING TECHNOLOGIES, PHYSICAL PRINCIPLES & USED MATERIALS

J. Gutwirth [(a)], T. Wágner [(a, b)], M. Frumar [(a)]

(a) University of Pardubice, Faculty of Chemical Technology, Department of General and Inorganic Chemistry - Research Centre LC 523, nám. Čs. legií 565, 532 10 Pardubice, Czech Republic; e-mail: Jan.Gutwirth@upce.cz
(b) University of Pardubice, Centre for Material Science, Studentská 95, 532 10 Pardubice, Czech Republic

Demands on long time data archiving lead to development of several data storage technologies. These data storage technologies utilize different physical principles which result in different properties of particular memories.

There are some crucial factors which determine application potential of memories. Acessibility (Read Only Memories (ROM) / Write Once Read Many Memories (WORM) / Read and Write Memories (RAM/RWM)), archival lifetime and restrictions on ambient conditions should be mentioned for example. Practical aspects like as capacity/storage density, read/write data throughput, rewritability (maximum of write-erase cycles), energy consumption, heat dissipation, price/price per bit, etc. are additional limiting factors for memory application.

The most widespread data storage technologies are hard disc drives (HDD), optical discs and Flash memories nowadays.

HDD (together with floppy disc drives (FDD), streamer tapes, etc.) belong to the magnetic data storage technologies. This technology is based on domain magnetization of recording film (usually nanoparticles ferromagnetic metals like Co, Ni, Fe diluted in paramagnetic matrix (Pt, C, SiO_2)) and detection of remanent magnetic induction orientation.

Optical discs (CD, DVD, HD-DVD, Blu-ray Disc) belong to the optical data storage technologies. This technology is based on different intensity of reflected laser beam. This intensity change is achieved by different methods: i) by change of reflection plane position (i.e. by pressing data pits into substrate) in case of read only discs (ROM), ii) by change of reflectivity of recording film - ii-a) caused by decomposition of organic dye (e.g. copper phtalocyanine) in case of write once (recordable) (R) discs or ii-b) caused by amorphisation/crystallization of Te-based alloys (usually from Ge-Sb-Te or Ag-In-Sb-Te system) in case of rewritable (RW/RE) discs, respectively. It means that recordable discs could be classified as a memory utilizes change of chemical identity of storage material while rewritable discs are phase change memories in principle.

Flash memory is commercial acronym for kind of Electrically Erasable Programmable Read Only Memory (EEPROM). This technology utilizes unipolar Metal Nitride-Oxide Semiconductor (MNOS) transistors with floating gate. Data writing consist in charging/discharging of the floating gate which results in change of the ohmic resistance of the memory cell. This difference is used for detection.

As new approaching technologies should be mentioned especially Solid State Drives (SSD), Magnetoresistive RAM (MRAM), Ferroelectric RAM (FeRAM), SONOS (Silicon Oxide Nitride Oxide Silicon) memory, Phase Change/Phase/Chalcogenide RAM (PC-RAM/P-RAM/C-RAM), Programmable Metallization Cell/Conductive Bridge RAM (PMC/CB-RAM), Resistive RAM (RRAM).

SSD utilizes the same technology as Flash memories (i.e. EEPROM), but its architecture is proposed to be able to emulate HDD interface.

MMRAM belongs to magnetic data storage technologies. This spintronic technology utilizes spin valves - i.e. two ferromagnetic layers (e.g. Fe, Ni, Co) spaced by dielectric layer (e.g. Al_2O_3). Ohmic resistance of such structure is different for parallel and antiparallel orientation of remanent magnetic induction of ferromagnetic layers for spin polarized current. Thus the detection resides in measurement of resistance while data recording is done by change of magnetization of one of the ferromagnetic layers by current pulse.

FeRAM is electronic memory derived from volatile Dynamic RAM (DRAM). DRAM cell consists of transistor and capacitor; data writing resides in capacitor charging/discharging driven by transistor, while data reading consists in detection of capacitor charge. In FeRAM, dielectric layer of capacitor is replaced by ferroelectric layer (e.g. PZT perovskites ($Pb[Zr_xTi_{1-x}]O_3$; $0 \leq x \leq 1$)). Principle of FeRAM is the same as for DRAM, but using of ferroelectric material leads to nonvolatility of the memory.

SONOS memory is electronic memory derived from the Flash memory by addition of next nitride layer into the floating gate structure. This addition leads to enhance of charging-discharging characteristics.

PC-RAM/P-RAM/C-RAM belongs to the phase change memories. Data recording takes place via electrically induced phase change of active material (usually Ge-Sb-Te alloy) between amorphous and crystalline state due to Joule heating. Detection embody in electrical resistivity difference between amorphous and crystalline state.

PMC/CB-RAM is memory based on change of chemical identity of memory cell material. Principle of recording is electrically induced dissolution or separation of Ag in the chalcogenide matrix (usually Ge-S or Ge-Se alloy). Detection consists in electrical resistivity difference between Ag doped and Ag undoped material.

RRAM is next kind of the memory based on change of chemical identity of memory cell material. RRAM utilizes dielectric materials such as oxides of transition metals (e.g. TiO_2, NiO). Data recording principle is electrically induced formation/disaggregation of conducting channel of suboxides and/or elementary metal in memory cell material, while detection resides in change of ohmic resistivity.

Overview of current and approaching data storage technologies was done. Physical principles of particular memories will be summarized together with description of applied materials and memory cell structures. Application benefits (e.g. archival lifetime, data storage density, rewritability, energy consumption, scalability, etc.) and restrictions given by technology and by ambient conditions (vibrations, temperature, electric and magnetic fields, electromagnetic radiation, etc.) together with near future perspectives will be mentioned.

The authors thank to the Ministry of Education, Youth and Sports of the Czech Republic for Research Centre LC 523 project.

LITHIUM NIOBATE PREPARED BY SOL-GEL METHODS AS TARGETS FOR PULSED LASER DEPOSITION

V. Jakeš[(a)], J. Erben[(a)], K. Rubešová[(a)], P. Nekvindová[(a)], M. Jelínek[(b)]

(a) Institute of Chemical Technology Prague, Technická 5, 166 28 Prague 6, Czech Republic

(b) Department of Applied Optics, Institute of Physics AS CR, v. v. i., Na Slovance 2, 182 21 Prague 8, Czech Republic

Lithium niobate is a very important material due to its optical properties and as such it has been widely studied for possible photonic applications[1]. It can be used either as bulk material or in the form of thin layers. With a view to the pulsed laser deposition (PLD) of niobate thin layers, the bulk density of target is one of the crucial parameters that influence the quality of prepared film. To achieve the maximal bulk density of a target, precursor grain size should be minimal to enhance solid state reaction and densification at a sintering process. Sol-gel methods are well applicable in powder precursor preparation. The precursors have the advantage of high chemical homogeneity and also of smaller grain size, in comparison to the precursors prepared by solid state reaction. The particle size of precursor can be further decreased by decomposition of the gel in appropriate atmosphere.

$LiNbO_3$ precursor powders were prepared by the sol-gel method using Pechini polyesterification. The solution of niobium(V) was prepared in the following way: Nb_2O_5 was first dissolved in concentrated hydrofluoric acid and then precipitated in form of $Nb_2O_5.xH_2O$ by addition of concentrated ammonia. The precipitate was filtered; fluoride anions were removed by washing in diluted ammonia and then thoroughly washed in water. After filtration and washing, $Nb_2O_5.xH_2O$ was immediately dissolved in water solution of citric acid (molar ratio Nb:citric acid = 1:4) at 90 °C. After complete dissolution, Li_2CO_3 and ethylene glycol were added (molar ratio citric acid:ethylene glycol = 1:4) and the solution was heated first at 80 °C to remove water and then at 130 °C to promote polyesterification reaction. Subsequent thermal processing is summed up in Figure 1.

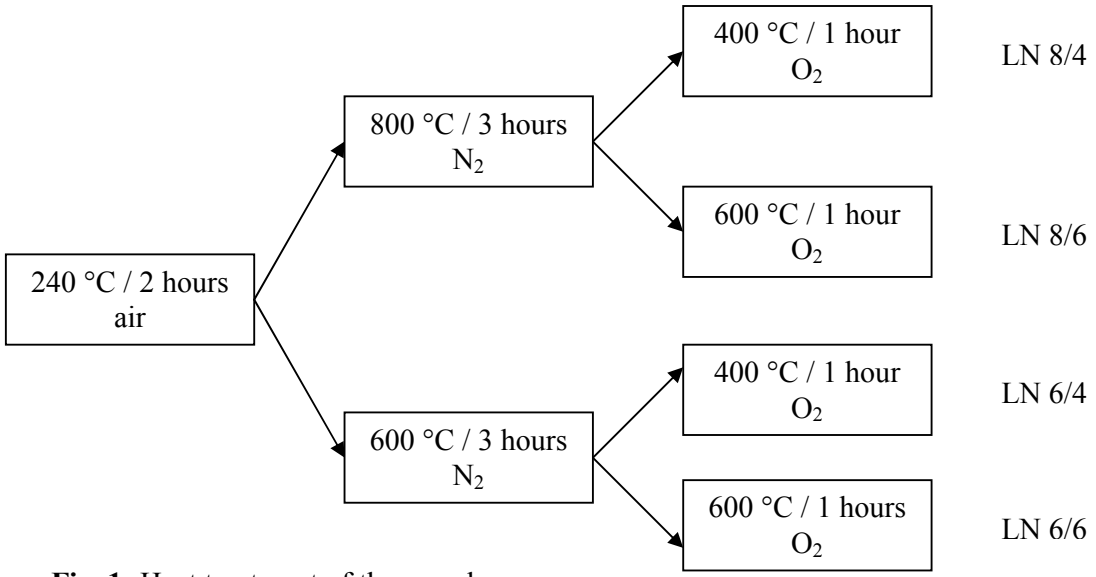

Fig. 1: Heat treatment of the samples

In addition to samples prepared from precursors decomposed in certain atmosphere, blind sample was prepared under standard conditions (heat treatment in ambient atmosphere at 240 °C, 500 °C and 700 °C, 2 hours each step) and named LN-Air.

From all precursors, pellets were pressed and sintered at 700 °C. The phase composition of all samples was determined by XRD and it was confirmed to be monophase $LiNbO_3$.

The microstructure of precursors was evaluated by SEM and selected micrographs are presented on Figure 2. The precursor prepared on air exclusively (LN-Air) contains aggregates of grains whereas precursor LN-8/4 is formed by individual grains of much smaller dimension.

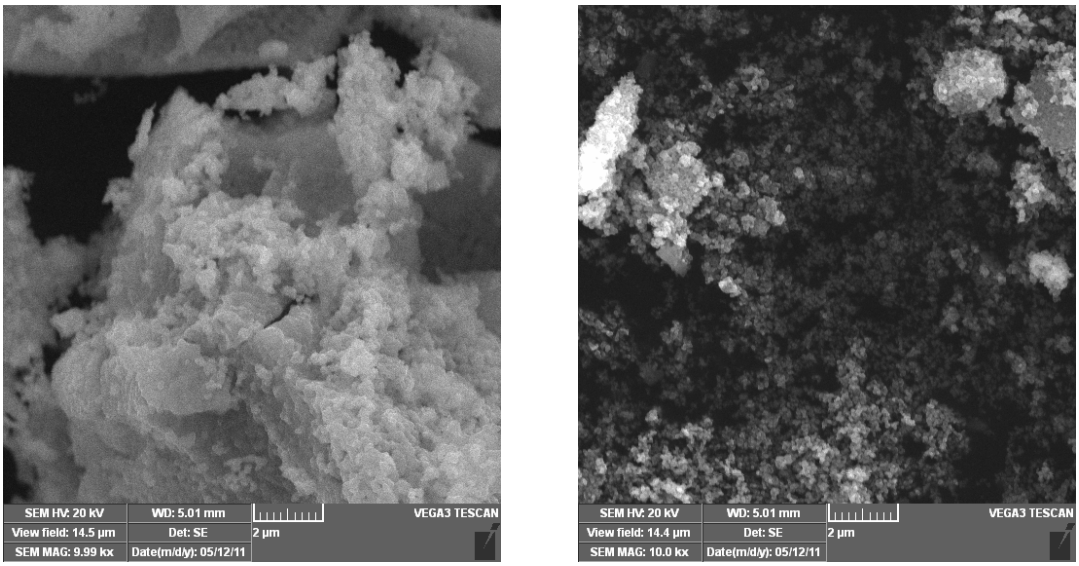

Fig. 2: SEM micrographs of grains of LN-Air (left) and LN-8/4 (right)

When using nitrogen atmosphere in the first high temperature step, organic matter in the gel cannot be oxidized to CO_2 and decomposes only to produce amorphous carbon. This carbon prevents the aggregation of oxide grains. Only after then, oxygen atmosphere allows the oxidation of carbon to carbon dioxide – for this reaction to occur, lower temperature is sufficient. In addition, second step temperature is not high enough to allow sintering of the grains and thus the precursor obtained is much more suitable for preparation of denser targets for PLD.

The precursor with the smallest grain size was used for a target preparation. The pellet of 1 inch diameter was pressed and sintered 24 hours at 700 °C. The target was used at PLD. The prepared layer was characterized by XRD and AFM and, next, compared with the properties of layers prepared from i) commercially available target and ii) target prepared by sol-gel under standard conditions (gel decomposed on air).

This work was financially supported by the Czech Science Foundation, the project No. P106/10/1477.

[1] 1 Arizmendi, L. Photonic applications of lithium niobate crystals. *physica status solidi (a)* **201**, 253-283, doi:10.1002/pssa.200303911 (2004).

IS THE CRYSTAL STRUCTURE DETERMINATION FROM POWDER SAMPLE USEFUL FOR "COORDINATION" CHEMIST?

V. Jorík

Institute of Inorganic Chemistry (FCHPT), Slovak University of Technology,
812 37 Bratislava, Slovakia

The application of X-Ray crystal structure determination from powder diffraction data is increasing everywhere where can not be met the requirements for single crystal of suitable size and quality. Although the single crystal and powder diffraction data contain essentially the same information, the single crystal data are distributed in three dimensions, while the powder data are superimposed in one-dimensional powder diffraction pattern. The effect of this superposition is usually a strong overlap in the powder diffraction pattern, which makes it difficult to obtain reliable information necessary to solve the crystal structure (position and intensity of the diffraction maxima). Considering the large number of important materials that can be prepared only as polycrystalline powders, considerable emphasis is placed on the development of this methodology, focused just to overcome the problem of diffraction overlap.

Determination of crystal structures from powder diffraction data is a three step process: *(i)* determination of lattice parameters and space group assignment, *(ii)* crystal structure solution – searching for structure model, *(iii)* crystal structure refinement. The goal of crystal structure solution *(ii)* is currently obtaining an approximate initial structure model, either by solution of crystal structure in reciprocal space - the "traditional approach" or using the method of global optimization. Both techniques exploit lattice parameters and space group determined in the first instance *(i)*. If the structure model is a good approximation of the actual crystal structure we can obtain an information on the crystal structure of good quality after refinement *(iii)*.

It will be interesting ask ourselves whether it is necessary structure analysis from powder data, as there are many years improved, perfectly functioning single crystal structure analysis with excellent experimental base. The table gives in a transparent manner comparison of advantages (✓) and disadvantages (✗) single crystal and powder structure analysis:

Single crystal structure analysis	**Powder Structure Analysis**
✓ratio "number of diffraction / number of refined parameters" is large enough to provide a stable solution by least squares method	✗ ratio "number of diffraction / number of refined parameters" is a small - to bring stability to the solution of least squares method we are forced to use soft / hard constraints
✓significantly more accurate and detailed Fourier analysis - allows to trace missing or excluded incorrectly entered atoms	✗ Fourier analysis provides a "fuzzy" information - used global optimization in direct space, the chemical composition is therefore critical

✓atomic coordinates are obtained to within fourth decimal place	× atomic coordinates are obtained to within third decimal place
✓ "meaningful" temperature factors, the possibility of their anisotropic refinement	× already isotropic temperature factors have often meaningless value
✓structural model is obtained without assumptions about its geometry, with only a basic chemical information on the substance	× structural model is obtained and refined using the known structural data (bonds, bond angles), fragments of isomers eventually polymorphic substances or optimizing the geometry of the molecule by the energy minimization method
× a need for single crystal of suitable size, often necessity of recrystallization from a solvent other than the reaction solution	✓single crystal is not necessary, in the diffraction experiment is used powdered sample
× it is uncertain to what extent represents "the only single crystal" the entire quantity of the prepared substance	✓for the diffraction experiment is used a larger quantity of the substance - better represents the entire prepared substance in analogy to the case of indirect methods - possibly allows to identify present impurities
× less accurate lattice parameters	✓more accurate lattice parameters
	✓to give the structural information about the primary product of chemical reaction

Looking to the table, it would seem that in the context of potential problems which can occur in the crystal structure determination from powder diffraction data, powder structure analysis is too complicated and not very effective method. However, there are situations where it is the only method which allows study and understanding of most aspects of the crystal structure of the solid phase, as can be demonstrated in many examples.

Grant agency is acknowledged for the financial support: VEGA 1/0562/10.

X-RAY DIFFRACTION AND BARKHAUSEN NOISE ANALYSIS FOR INVESTIGATION OF REAL STRUCTURE CHANGES FOR CAR INDUSTRY COMPONENTS

Kamil Kolařík [(a)], Nikolaj Ganev [(a)], Lucie Vrkoslavová [(b)]

(a) Department of Solid State Engineering, Faculty of Nuclear Sciences and Physical Engineering, CTU in Prague; Trojanova 13, 120 00 Prague 2, Czech Republic
(b) Department of Machining and Assembly, Faculty of Mechanical Engineering, Technical University of Liberec, Studentská 2, 461 17 Liberec 1, Czech Republic

1. Introduction

The contribution is focused on the recent experience of the authors with industrial applications of X-ray diffraction (XRD) residual stress (RS) measurement and Barkhausen noise analysis (BNA). Both methods are used for control and optimization of technological parameters during final surface machining and for assessment of case-hardened and nitrided layers used on components in car industry. Moreover, they are used to verify whether a required level of residual stresses in given subsurface areas was achieved and also serve as a fast output inspection of machine parts´ surface quality. The residual stresses have a significant influence on the fatigue limit; in the case of compressive surface stresses the effect is favourable, however the tensile residual stresses are detrimental and could lower the stress corrosion resistance of materials.

Case-hardening is a common heat treatment for steels, the subsequent quenching results in hard layer with martensitic structure. Case-hardening leads to hard case and soft core formation, and thus increases wear resistance and fatigue strength of treated components. Nitriding is a process for surface hardening of steels which takes place in saturated nitrogen atmosphere at the temperature of 500 – 550 °C. Nitriding, creating a layer of hard nitrides on the sample surface, is performed after quenching and tempering. In addition, it improves corrosion resistance and reduces friction coefficient. These heat treatments methods were chosen because they are often used in car industry.

BNA allows a simple, fast, real time, and non-destructive testing of the level of residual stresses and other structure-related parameters in camshafts, case-hardened and nitrided components in car industry. Thus, the homogeneity of the heat treatment is checked. Nevertheless, this output inspection needs to be verified and confirmed by residual stress XRD measurements.

2. Sample under Investigation

The effect of grinding and rolling on residual stresses and parameters of BNA was studied on machined surface layer of three camshafts from *16MnCrS5+HH* material for Diesel injection pump Common Rail. XRD and BNA on surfaces were performed in axial and tangential directions on two selected parts, lobe 1 and lobe 2, namely on a chosen flat surface and curved surface areas. The measured areas are depicted schematically in Fig. 1.

The six samples investigated were case-hardened and nitrided components for car industry, made of rolled steel sheet *C10* with case-hardening depth (CHD) from 0.100 to 0.225 mm and with nitrided layer depth (ND) from 0.012 to 0.014 mm. Since the surface of measured samples was dissected, sample areas to be studied were divided into several

sections. The areas are shown in Fig. 2. The reference sample (steel *C10*) without any heat treatment was investigated as well.

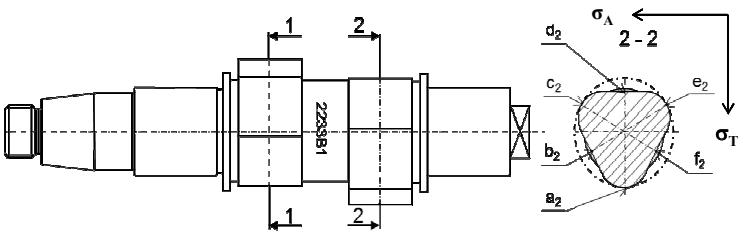

Fig. 1 Scheme of the measured areas on the camshafts with marked directions of stress determination σ_A, σ_T

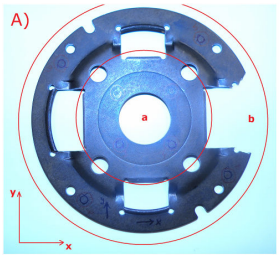

Fig. 2 Case-hardened sample areas a, b

3. Selected Results and Conclusions

The selected results of RS (XRD) gradient and *mp* (BNA) from flat surface area d_1 (see Fig. 1) obtained after gradual etching of the surface are illustrated in Fig. 3. Magnetizing voltage sweep (MVS) of case-hardened samples (see. Fig. 2) show that the voltage sweep level increases with the increasing case-hardening dept (Fig. 4).

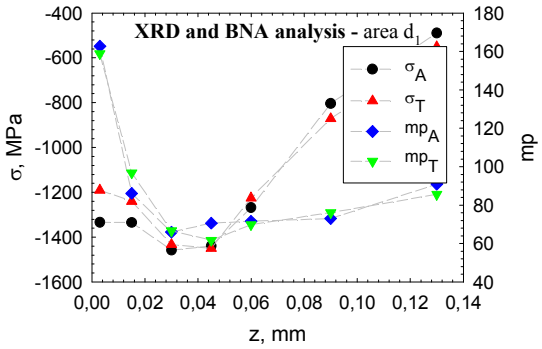

Fig. 3 Gradient of RS (σ_A, σ_T) and mp (mp_A, mp_R) determined by XRD and BN analysis

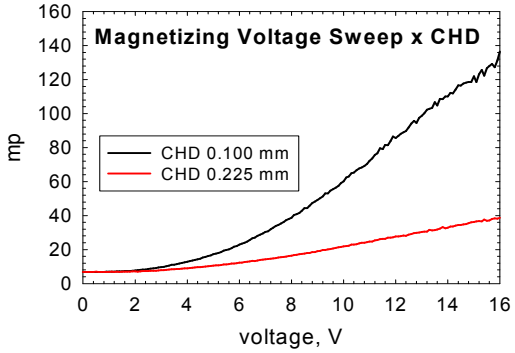

Fig. 4 Correlation of the voltage sweep level with increasing case-hardening dept

In all the studied cases of surface camshafts measurements the mp_A values are lower than mp_T ones. This effect is caused by mechanical interaction of the cutting tool, i.e. grinding wheel, with the surface of the machined camshaft. Absolute value of RS σ_A and σ_T exhibits the same relation. This finding is in accordance with the theoretical knowledge stating that compressive RS should reduce *mp* value.

Case-hardened samples showed decrease of *mp* (BNA) and full width half maximum (XRD) with increasing CHD. The MVS level decreases with increasing CHD.

Nitrided samples showed decrease of *mp* from BNA and increase width half maximum from XRD with increasing CN. The MVS and MFS level increasing with increasing CHD.

To summarize all conclusions, magnetoelastic parameter (*mp*) such as remanence (*Br*) and permeability (μ) correlates with residual stress; magnetizing voltage sweep (MVS) and magnetizing frequency sweep (MFS) correlate with case-hardened and nitrided layer depth. These relationships can be used for fast output industrial control.

The research was supported by the projects SGS of Czech Technical University in Prague and Technical University of Liberec and the project FRVŠ 2643/F1.

NEW COORDINATION COMPOUNDS OF Cu(II) WITH PYRIDYLMETHANOLS

M. Koman, J. Moncoľ, J. Maroszová, and D. Valigura

Faculty of Chemical Technology, Slovak University of Technology, 812 37 Bratislava, Slovak Republic

The syntheses and determination of the crystal structure of copper(II) coordination compounds have been the subject of many recent studies with the aim of understanding the relation among composition, structure and properties coordination compounds. The copper(II) carboxylates have been the subject of numerous investigations, especially with nitrogen donor ligands [1]. Copper(II) ions play a vital role in a number of widely differing biological processes, and their interaction with drugs administered for therapeutic reasons is of considerable interest. Some carboxylic acids and their derivatives also play an important role in biological processes [2-5]. The pyridylmethanols [2-pyridylmethanol (2-pyme), 3-pyridylmethanol (3-pyme), as well ronicol (ron) and 4-pyridylmethanol (4-pyme)] (Scheme 1) have interesting properties in biological systems as anti-inflammatory agents [6]. From structural point of view pyridylmethanols prefers definite types of structures.

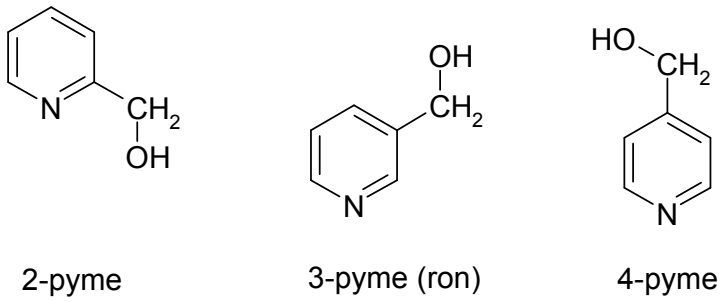

2-pyme 3-pyme (ron) 4-pyme

Scheme 1. The 2-, 3- and 4-pyridylmethanols.

The 2-pyridylmethanol in complexes of Cu(II) preferentially as chelating agent and $[Cu(2\text{-pyme})_2L_2]$ (L = anionic ligand) complexes usually formed. With 2-pyme were prepared also compounds $[Cu(2\text{-pyme})_2(3,5\text{-}(NO_2)_2bz)].(3,5\text{-}(NO_2)_2bz)$ [3,5-$(NO_2)_2$bz = 3,5-dinitrobenzoate], where Cu(II) atom is pentacoordinated, dimeric $[Cu_2(2\text{-pyme})_4].(ClO_4)_2$ and polymeric $[CuCl_2(2\text{-pyme})]_n.n(CH_3OH)$. The 3-pyridylmethanol is usually N,O-bridging ligand and its complexes are coordination polymers resulting in 1-D chains or 2-D sheets, but only for a few complexes, it is terminal ligand $[Cu(3\text{-Mesal})_2(3\text{-pyme})_2(H_2O)].(H_2O)$ [3-Mesal = 3-methylsalicylate] with monomeric structure and $[Cu(\mu\text{-}3\text{-MeOsal})_2(3\text{-MeOsal})_2(3\text{-pyme})_4]$ [3-MeOsal = 3-methoxysalicylate] with dimeric structure. The different transitional variations in this rich group of compounds will be discused. In small group of compounds with 4- pyridylmethanol as neutral ligand are monomeric compounds $[Cu(2\text{-Brbz})_2(4\text{-pyme})_2(H_2O)]$ [2-Brbz = 2-bromobenzoate] where 4-pyme is monodentate and also polymeric

$[Cu(3\text{-}NO_2bz)_2(4\text{-}pyme)_2]_n$ [3-NO_2bz = 3-nitrobenzoate] where 4-pyridylmethanol is N,O-bridging ligand.

In this paper, we present no usual crystal structures of Cu(II) complexes with pydidylmethanols.

The authors wish to thank the Slovak Ministry of Education (VEGA project 1/0562/10) for financial support.

[1] (a) M. Melník, Coord. Chem. Rev. *42*, (1982) 259. (b)Kato M., Muto Y.: ibid, 92 (1988) 5.
[2] B. Kozlevčar, N. Lah, I. Leban, Croat. Chim. Acta 73, (2000) 733.
[3] M. Melník, M. Koman, D. Hudecová, J. Moncoľ, B. Dudová, T. Glowiak, J.Mrozinski and olloway : Inorg. Chim. Acta 308, (2000) 1.
[4] M. Koman, M. Melník, J. Moncoľ and T. Glowiak: Inorg. Chem. Comm. 3, (2000) 489.
[5] J. Moncoľ, M. Palicová, P. Segľa, M. Koman, M. Melník, M. Valko and T. Glowiak, Polyhedron 21 (2002) 365.
[6] M. Melník, K. Smolander and P. Sharrock: Inorg. Chim. Acta 103, (1985) 187.

ANISOTROPIC ETCHING OF SILICON BY TMAH

P. Kostelník

ON Semiconductor, 1. máje 2230, 756 61 Rožnov pod Radhoštěm, Czech Republic

Wet etching processes are widely used in manufacturing of both silicon wafers (cleaning, stress relief etching) and silicon based electronic devices (cleaning, removal of grown/deposited layers on unmasked areas). These processes usually use isotropic wet etchants (etch rate is constant for all of the silicon crystallographic planes) such as HNA (mixture of hydrofluoric, nitric and acetic acids) for etching of silicon and diluted hydrofluoric acid for removal of silicon dioxide. On the other hand, anisotropic etchants demonstrate dependency of etch rate on the crystallographic orientation of the etched planes – selective etching. Such a behavior can be used for micromachining of micro-electro-mechanical systems (MEMS), special SOI based devices, SiO_2 membranes, etc.

There are several anisotropic etchants such as ethylenediamine-pyrocatechol (EDP), potassium hydroxide (KOH) and tetramethyl ammoniumhydroxide (TMAH). However, due to high cost and toxicity of EDP and presence of CMOS incompatible K^+ ions in KOH, TMAH remains the best choice for the above mentioned processes. TMAH as well as the rest of the anisotropic etchant shows in addition to the etching anisotropy also several other types of selectivity; a) selectivity to heavily boron doped silicon and b) selectivity to SiO_2 and Si_3N_4. Both types of the selectivity are usually combined with the etching anisotropy to form the above mentioned structures.

The etching anisotropy of TMAH can be shown on etch rates of three most common silicon crystallography planes. The {110} shows the highest etch rate, {100} medium etch rate and {111} very low etch rate. The etch rate ration between {110} and {111} planes is approximately 40:1 [1]. The difference in etch rate can be explained by different surface structure of the respective crystallographic planes [2]. The way of using this behavior for micromachining can be shown on preparation of a thin SiO_2 membrane on a Si(100) wafer (see Figure 1a). SiO_2 is used for both membrane and etch mask material. The Si(100) material is etched away and the etching is stopped on the sides of the mask window by the {111} planes and the SiO_2 layer on the other side of the wafer, thus forming a thin SiO_2 membrane. However, formation of a membrane requires a significantly larger area, than the area of the membrane itself. This is due to the 54.7° angle between the {100} and {111} planes. Such a configuration is not favorable for miniaturization and space optimization. Formation of microstructures without any additional area is however possible on the Si(110) wafer (see Figure 1b), where a set of {111} planes perpendicular to the wafer surface can be found.

We have investigated the TMAH etch conditions of the Si(110) wafers. We present data on the etch rates of the {110} and {111} planes for different composition of the TMAH etchant (see Figure 2). We further discuss the characteristics of the masks from both material and crystallographic orientation points of view, which are needed for successful micromachining.

This work is partially supported by grant FR-TI3/031 awarded by Ministry of Industry and Trade of the Czech Republic.

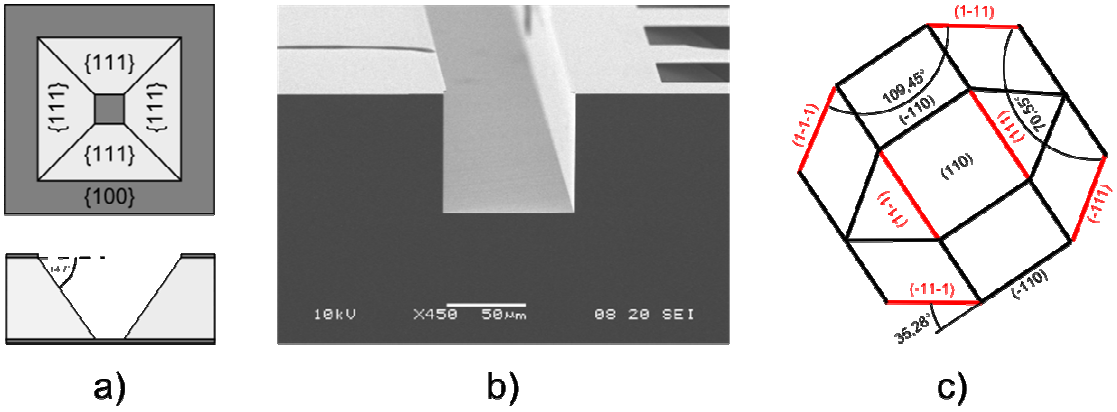

Figure 1: a) Top and side view of the SiO_2 membrane etched into Si(100) wafer, SiO_2 is shown in dark grey, silicon in light. b) Deep grove etched by TMAH into Si(110) wafer. c) Schematics of orientation of {111} planes with respect to the (110) one.

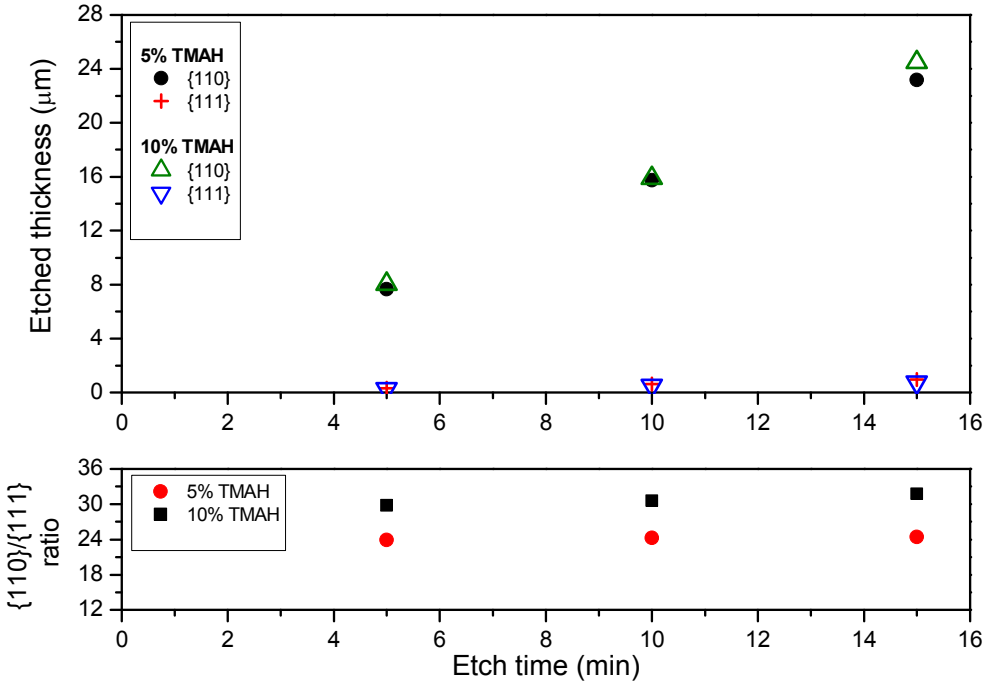

Figure 2: Etched thicknesses of Si{110} and Si{111} planes for various etch times in 5% and 10% TMAH solution at 80 °C (top) and etch rate ratio between the Si{110} and Si{111} planes (bottom).

[1] K. Sato, M. Shikida, T. Yamashiro, K. Asauni, Y. Iriye, M. Yamamoto, Sensors and Actuators, 73 (1999) 131-137.

[2] R. Charavel, Etch rate modification by implantation of oxide and polysilicon for planar double gate MOS fabrication, Dissertation Thesis, University of Louvain 2007.

CRYSTAL NUCLEATION AND GROWTH ON HETEROGENEOUS SURFACE

Z. Kožíšek [(a)], P. Demo [(a, b)], A. Sveshnikov [(a, b)], P. Tichá [(a, b)]

(a) Institute of Physics, Academy of Sciences of the Czech Republic, Cukrovarnická 10, 162 00 Prague 6, Czech Republic
(b) Czech Technical University in Prague, Faculty of Civil Engineering, Thakurova 7, 165 29 Prague 6, Czech Republic

The template-assisted formation of crystallites (i. e. nucleation and growth of nuclei up to observable sizes) is a complex phenomenon due to many concurrent processes occurring near the surface. On the surface, where heterogeneous nucleation occurs, some active centers (nucleation sites) can exist. These centers decrease the energy barrier of nucleation and thus the probability of formation of nuclei is much higher than that on homogeneous surface. In some cases it is difficult to exactly identify active centers. One can find large amount of active centers in atmosphere (product of emissions, volcano eruptions, etc.). On the other hand Kumomi and Shi [1] initiated nucleation process at the artificial nucleation sites. In some cases the nucleation agent is added to the supercooled melt to increase nucleation rate [2]. In this work we focus on vapor-solid surface nucleation on active centers.

It is well known [3] that in the case of homogeneous nucleation (nucleation occurs within volume on any site) the total number of nuclei *Z* (experimentally detectable) formed in unit volume linearly increases with time after some time delay (stationary state). Nucleation rate, i.e. the number of nuclei formed in unit volume per unit time, is equal to the time derivative of the total number of nuclei and thus it is constant (stationary nucleation rate). Stationary state is reached after some time delay. Analytical solution of the stationary nucleation rate is widely used due to its simplicity.

In the case of heterogeneous nucleation [3] the total number of nuclei at a sufficiently long time goes to the number of active centers N_A, i. e. the total number of nuclei remains unchanged after some time delay. In both cases the total number of nuclei greater than some nucleus size *m* can be expressed by:

$$Z_m\ (t) = \sum_{i>m} F_i\ (t) = \int_0^t J_m\ (t')\ dt',$$

where $F_i(t)$ denotes the number density of nuclei of size *i* (the number of molecules within cluster) at time *t* and J_m is the number of *m*-sized nuclei formed on unit surface per unit time.

Standard models [3] use one additional equation to take into account the depletion of the active centers during nucleation process. We have shown that this process is possible to model within standard model without any additional equations, but it is necessary to modify initial and boundary conditions to include depletion of the active centers [4]. The active center is not considered in the nucleation process as soon as the nucleus is formed on this site. Kinetic equations describing heterogeneous nucleation on active centers were solved numerically. Nucleation rate reaches some maximum value and goes to zero with time and thus is is not possible to use the stationary approach to nucleation rate.

In our model we have took into account not only the depletion of active centers during nucleation and growth, but also the depletion of supersaturated vapor pressure as a part of molecules is transferred from the supersaturated mother phase to a newly formed crystal phase. The total number of nuclei increases with time and goes to the number of active centers N_A- see Fig. 1.

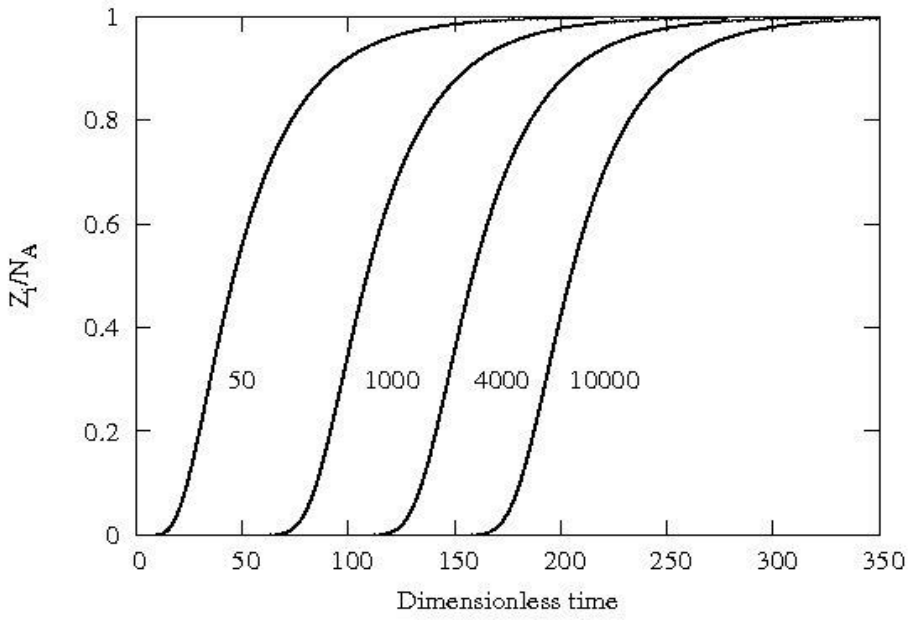

Fig. 1: The total number of nuclei Z_i as a function of dimensionless time for nucleus sizes i = 50, 1000, 4000 and 10000 molecules.

It is seen that the time delay of nucleation increases with nucleus size. Decrease in the vapor pressure is low, but it plays important role as larger nuclei are formed.

This work was supported by the Grant No. IAA100100806 of the Grant Agency of the Academy of Sciences of the Czech Republic. Scientific activities in the Institute of Physics AS CR are supported by the Institutional Research Plan No. AV0Z10100521.

[1] H. Kumomi, F. G. Shi, *Alternative Origin of Log-Normal Size Distributions of Crystallites in Controlled Solid-Phase Crystallization of Amorphou Si Thin Films*, Phys. Rev. Letts. (1999) 2717.

[2] Z. Kožíšek, M. Hikosaka, K. Okada, P. Demo, *Size Distribution of Folded Chain Crystal Nuclei of Polyethylene on Active Centers*, J. Chem. Phys. 134 (2011) 114904.

[3] D. Kashchiev, *Nucleation: Basic Theory with Applications*, Butterworth-Heinemann, 2000.

[4] Z. Kožíšek, P. Demo, M. Nesládek, *Transien nucleation on inhomogeneous foreign substrate*, J. Chem. Phys. 108 (1998) 9835.

STUDY OF GROWTH CONDITIONS INFLUENCE ON SHAPE AND POSITION OF CRYSTAL/MELT INTERFACE DURING CRYSTAL GROWTH OF TERNARY HALIDES BY VERTICAL BRIDGMAN METHOD

R. Král and A. Cihlář

Institute of Physics, Academy of Sciences of the Czech Republic, 162 00 Prague 6, Czech Republic

Single crystals of ternary alkali lead halides are promising materials with different optical properties and wide range of optical applications mainly as suitable host materials for construction of mid-infrared solid-state lasers at room temperature [1, 2]. These crystals are grown by the vertical Bridgman method but preparation of high quality single crystals is very difficult, because of low heat conductivity of solid halides [3].

This contribution deals with the study of influence of growth conditions (temperature gradient and pulling rate) on the position and the shape of crystal/melt interface. Its aim is to optimize growth conditions to reach a planar or better a little convex crystal/melt interface, what we consider as a main condition for effective crystal growth. Exploration of optimal growth conditions using $PbCl_2$ and $RbPb_2Br_5$ as model compounds was performed by studying the position and the shape of the crystal/melt interface by means of direct temperature measurements of temperature field in a specially prepared quartz ampoule filled with $PbCl_2$ during simulated crystal growth in the vertical Bridgman arrangement.

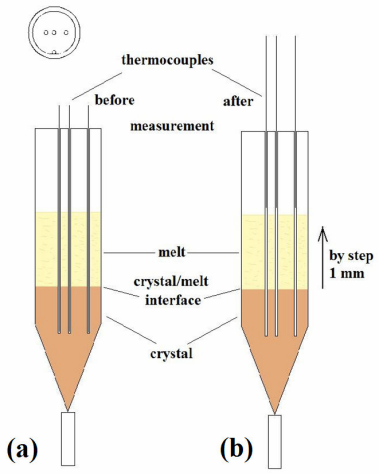

Fig.1. Illustrated temperature field measurement in the specially prepared quartz ampoule with 4 capillaries and thermocouples placed in them before (a) and after (b) the temperature field measurement.

Measurement of the temperature field during the simulated crystal growth was performed in the special quartz ampoule with 4 asymmetrically placed capillaries (inner diameter of 1.2 mm) inside the ampoule. The first capillary was centered in the axis of the ampoule, second one was placed along the inner wall of the ampoule, and other two capillaries were in two different positions between the axis and the wall. Into these capillaries were inserted 4 measuring thermocouples so that their sensors were in the same level as shown as in Fig. 1a. The temperature in the ampoule was sampled by all thermocouples every 1 second and when two successive temperature measurements of the thermocouple placed in the capillary at the inner ampoule wall were of the same value all thermocouples moved up by a step of 1.0 mm (Fig.1b). In this way the temperature was sampled from the bottom transient crystalline phase, through the crystal/melt interface, the dark yellow melt, the melt surface, and the atmosphere over it in total length of 65 mm (see Fig.2). Movement of thermocouples, the temperature measurement and its recording were software controlled.

Temperature field in the ampoule was measured in four different furnace gradients from very steep (35 K/cm) to gradual (20 K/cm) one at three different positions of the ampoule in the furnace. At the position one: there was more melt than the crystalline phase, position two:

the ratio of the crystalline phase and the melt was equal, and position three: there was more crystalline phase. Measuring procedure was as follows: the ampoule was set in the furnace in the asked position and after 3 hours, when the system was stabilized, the temperature measurement started. For each position at least 5 temperature measurements in one hour intervals were performed to be sure that temperature field in the ampoule system was stable. After every measurement the ampoule was pulled out from the furnace and the position and the shape of the crystal/melt interface were digitally captured and recorded as shown in Fig.2.

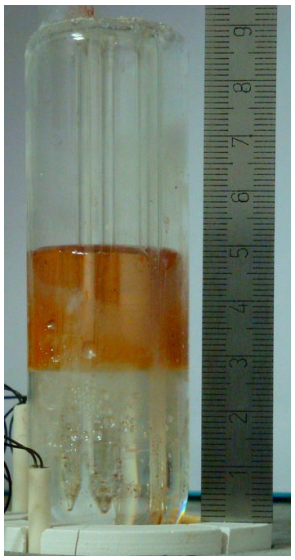

Fig. 2. Measuring quartz ampoule filled with $PbCl_2$ and captured crystal/melt interface with 4 capillaries for temperature measurements.

Obtained results of temperature measurements were set of "isolevel" temperature curves through the studied system, but for further study it was more practical to recompute these data by a linear approximation into isothermal curves. Positions and shapes of crystal/melt interfaces of all tested positions of the ampoule in gradients were determined by comparison of obtained results with taken pictures of the crystal/melt interface in the ampoule. Results of temperature field measurements were also used as boundary conditions for a mathematical modeling of a melt flow and temperature field (isotherms) in the studied system.

This work is supported by the Grant Agency of the AS CR by the Junior Research Grant Project No. KJB200100901.

[1] L. Isaenko, et. al., Mat. Sci. and Eng. B81 (2001) 188–190.
[2] K. Rademaker, et. al., J. Opt. Soc. Amer. B-Opt. Phys. 21 (2004) 2117–2129.
[3] R. Král, The 16th International Conference on Crystal Growth (ICCG-16), Beijing, China, August 8-13, 2010.

INFLUENCE OF NONSTOICHIOMETRY ON THE TRANSPORT PROPERTIES OF THE GaGeTe COMPOUND

V. Kucek, Č. Drašar, L. Beneš, P. Lošťák

Faculty of Chemical Technology, University of Pardubice, Studentská 573, 532 10 Pardubice, Czech Republic

Nowadays, we observe a boom in search of alternative power resources. One of the alternatives is use of thermoelectric effects. Research on thermoelectric (TE) materials is thus one of very active fields of research. Efficiency of a TE material is expressed in terms of so called TE figure of merit ZT, $ZT=\sigma S^2T/\kappa$ (σ- electrical conductivity, S- Seebeck coefficient, κ- thermal conductivity, T- absolute temperature) [1]. New complex so called nanostructured bulk materials are needed to further improve the efficiency of the bulk thermoelectric materials. One candidate should be GaGeTe compound which has layered complex structure much like the Bi_2Te_3 based thermoelectric materials.

In the GaTe - Ge system there is GaGeTe compound with peritectic melting point 1073 K. GaGeTe crystallizes in hexagonal crystal lattice (space group R3m) with layered structure with distinct cleavage planes perpendicular to the trigonal c –axis. According to [2] its lattice parameters are a=4.05Å, c=34.65Å. In the literature, there are studies of crystal structure [3] and an investigation of chemical bonding using Raman spectroscopy [4] only. The aim of this contribution is to present original information on transport properties of $Ga_{1+x}Ge_{1-x}Te$ and the influence of nonstoichiometry on them.

Polycrystalline samples $Ga_{1+x}Ge_{1-x}Te$ (x= -0.03 - 0.07) were synthesized from elements Ga, Ge and Te of 5N purity. The mixture of elements was heated in evacuated quartz ampoule at 1220 K for 75 minutes and quenched in air. The ampoules were further annealed at 770 K for 3 days to reach equilibrium. Products were powdered for one minute in vibrating mill and identified by X-ray diffraction analysis using D8-Advace diffractometer (Bruker AXE, Germany) with Brag-Brentano θ-θ geometry. Bulk samples with dimensions of 15x3.5x2 mm^3 were prepared from the powder using high pressure/high temperature (820K/85MPa) technique in a graphite die. Density of the samples was always higher than 90% of its theoretical value. The transport parameters we report on include electrical conductivity, Seebeck coefficient, Hall coefficient measured over a temperature range from 80 K to 450K.

XRD investigation showed that samples contain a negligible amount of the second phase (GaTe or GeTe). The traces of the foreign phases remain present also after a prolong annealing of 21 days and they are present also at the stoichiometric compound (x=0). This fact suggests GaGeTe compound deviates from stoichiometry1:1:1. This in turn suggests presence of defects in the crystal lattice. Sample with x = 0.07 contain significantly higher amount of GaTe and its volume of the unit cell is close to that of the sample with x = 0.05. This gives evidence that x = 0.05 is the solubility limit. The growing x in the $Ga_{1+x}Ge_{1-x}Te$ series leads to increase of the electrical conductivity up to x = 0.05 and to the increase of the free hole concentration up to x = 0.03. Increase of free hole concentration is confirmed by measurement of Hall coefficient. While Hall coefficient R_H at 300K decreases with increasing content of gallium up to x = 0.03, the Seebeck coefficient decreases with increasing x as evident from Table 1. Samples with $x \geq 0.05$ have slightly higher Hall coefficient probably due to the increase of the concentration of

minority light holes – due to rather high concentration of free holes second band becomes evident. Light holes should lead to a decrease of Seebeck coefficient. However, we observe a slight increase of the Seebeck coefficient for the sample with x = 0.07. This can be attributed to the increase of defect concentration and enhanced scattering of the free holes.

The observed increase of the hole concentration can be attributed to formation of point defects of type: $Ga_{Ge}^{-} + h^{+} \rightarrow Ga_{Ge}$. c-parameter of the unit cell monotonously decreases with increasing x up to x = 0.05 – this supports the idea of Gallium/Germanium substitution. Study of the temperature dependence of the thermal conductivity of the $Ga_{1+x}Ge_{1-x}Te$ samples can help to prove this idea. This is the next goal together with the study of nonstoichiometry of tellurium.

Table 1. Electrical conductivity σ, Seebeck coefficient S, Hall coefficient R_H , lattice parameters a and c and volume of unit cell V of $Ga_{1+x}Ge_{1-x}Te$ samples at 300K

Sample	σ [S/m]	S [μV/K]	R_H [cm^3/C]	a [nm]	c [nm]	V [nm^3]
$Ga_{0.97}Ge_{1.03}Te$	3554	130	0.3094	4.0508	34.7804	0.49425
$Ga_{0.99}Ge_{1.01}Te$	14440	109	0.1394	4.0485	34.7667	0.49349
GaGeTe	15378	105	0.1233	4.0486	34.7609	0.49344
$Ga_{1.01}Ge_{0.99}Te$	19136	94	0.0905	4.0493	34.7560	0.49354
$Ga_{1.03}Ge_{0.97}Te$	24288	67	0.0513	4.0492	34.7493	0.49342
$Ga_{1.05}Ge_{0.95}Te$	35389	56	0.0539	4.0592	34.7437	0.49424
$Ga_{1.07}Ge_{0.93}Te$	22673	59	0.0599	4.0524	34.7515	0.49423

This research was supported by the Ministry of Education, Youth and Sports of the Czech Republic under the project MSM 0021627501.

[1] G.S. Nolas, J. Sharp, H.J. Goldsmid, Thermoelectrics / Basic Principles and New Material Developments, Springer-Verlag Berlin Heidelberg, p. 128 (2001).
[2] G. Kra, R. Eholie, J. Flahant, Study of some selection of the gallium-germanium-tellurium ternary system. Gallium germanium telluride (GaGeTe), Comples Rendus des Seances de l´Academie des Sciences, Serie C: Science Chimiques 284 (1977) 889.
[3] D. Fenske, H. G. Von Schnering, GaGeTe the new defect tetrahedral structure, Angew. Chem. 95 (1083) 420.
[4] E. Lopez-Cruz, M. Cardona, E. Martinez, Raman spectrum and Lattice dynamics of gallium germanium telluride, Phys. Rev. B 29 (1984) 5774.

IMPEDANCE AND CONDUCTIVITY ANALYSIS OF POLYSTYRENE-CARBON BLACK COMPOSITES

J. Lipták, J. Sedláček, I. Pilarčíková, V. Bouda

Department of Electrotechnology, Faculty of Electrical Engineering, Czech Technical University in Prague, 166 27 Prague, Czech Republic

Introduction

If electrical conductive filler (carbon black (CB)) is used for polymer composite material preparation, the resulting sample electrical properties can change from insulator to conductor. When the percolation concentration of CB is reached, the continuous bulk network structure is formed in the composite. Conductivity dependence on CB concentration shows the sharp rise [1] (percolation threshold). Conductivity can change in the magnitude of several orders [1]. CB network formation is affected by many parameters as kind of polymer [2], properties of carbon black [3] (density, surface area, composition), ion concentration, external electrical field [4]. The measurement of electrical or dielectrical properties is very sensitive method for detection of conductive network or CB agglomerates formation. On the other hand, the actual measured values are strongly affected by many external (contact between electrode and CB, arrangement of measurement condenser, frequency, voltage etc.) and internal (connection of CB particles) conditions.

Experimental

The carbon black (CB) Chezacarb (Chemopetrol, Inc., Litvínov) and standard granulated non-expandable polystyrene (PS) (Kaučuk, Inc., Kralupy nad Vltavou) were used. The water content in CB was measured by drying on the hot plate HP 01 at 120 °C up to the constant weight using the analytical balance. The amount of water in CB was about 1,5 w%.

3 g of PS were mixed with the defined amount of CB in toluene. The rotational homogenizer IKA and homogenizer Sonopuls UW 3200 Bandelin were used for pulverisation and homogenisation of CB. Sample preparation procedure in more detail is described in previous paper [4]. The samples with CB content from 1 to 7 w% and the layers thickness (after toluene evaporation) from 0,1 to 0,3 mm were prepared. In this work we concentrated to differences between measurement methods and unlike electrodes arrangements. The optical microscope and AFM observations were added and compared with electrical properties.

Electrical measurement

The impedance - phase analysis in the frequency region 0 (DC) to 100 kHz was carried out with the HIOKI 3522-50 HiTESTER with 1 – 5 V measurement voltage. In normal direction the plate condenser with micro shift was used. The rigorous quantities as resistivity ρ (Ωm) for DC measurement and complex permittivity (relative) components ε' (-) and ε'' (-) for AC response were evaluated in the form:

$$\rho = \frac{S}{G \cdot d} \qquad \varepsilon' = \frac{C \cdot d}{\varepsilon_0 \cdot S} \qquad \varepsilon'' = \frac{G \cdot d}{\varepsilon_0 \cdot \omega \cdot S}, \tag{1}$$

where ε_0 is permittivity of vacuum, ω is angular frequency and d and S are the thickness and area of the sample respectively.

In addition, sheet resistance (Van der Pauw method), surface resistivity and bulk resistivity (three electrodes method with vacuum deposited Al electrodes) were measured and compared with the measurements in plate condenser.

All measured quantities ($1/\rho$, ε', ε'', sheet and surface conductivity) show reasonable increases for CB concentration higher than 2 w% (Fig.1). The frequency dependences of the complex permittivity components show the monotonically decreasing curves with increasing frequency. The decrease of ε'' at the frequency near 1 kHz is typical for space charge polarization response and DC conductivity. Therefore it can be pointed out that the major role is played by DC conductivity and relative large polarized agglomerates.

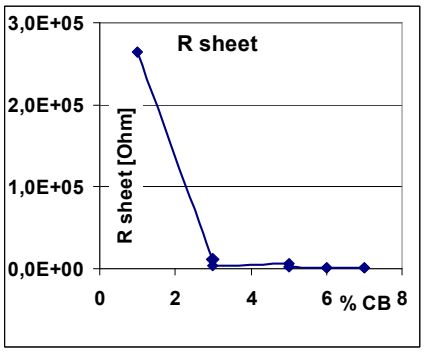

Fig. 1: Sheet resistance as a function of CB loading

Conclusions

The reasonable increases of ε', ε'' and $1/\rho$ take place with CB concentration above 2 w% CB loading. Therefore the conductive CB network formation was observed in layer samples. It was detected by different resistance measurements in normal and planar directions. The sample resistivity decreases with higher measuring voltage (Fig.2). It indicates non–ohmic mechanism of the charge carrier transport. The frequency dependences of both real and imaginary component of complex permittivity express that there is no Debye orientation relaxation mechanism. All AC results show to the space charge polarisation with a strong part of DC conductivity.

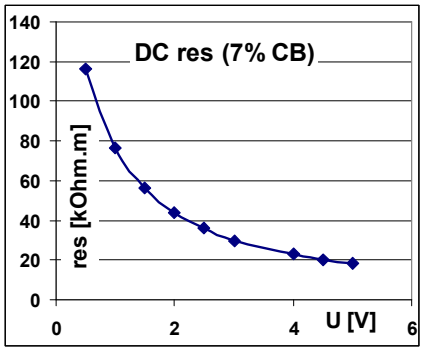

Fig. 2: DC resistivity versus measuring voltage [7% of CB]

References

[1] K. Miyasaka, et al., J. Mater. Sci. 17 (1982) 1610.

[2] G.S. Bjorklund, T.M. Baer, Photonics Spectra 2007, p. 70.

[3] T.A. Ezquerra, et al., J. Mater. Sci. Lett. 5 (1986) 10.

[4] J. Lipták, L. Turczynová, L., In: Conference Proceedings The 18th joint seminar DMSRE, Prague, Czechoslovak Association for Crystal Growth, 2008, p. 31-32.

SIMULATION OF A SURFACE PLASMON RESONANCE-BASED FIBER-OPTIC REFRACTIVE INDEX SENSOR

J. Luňáček, D. Ciprian, P. Hlubina

Department of Physics, VŠB - Technical University of Ostrava, 17. listopadu 15,
708 33 Ostrava - Poruba, Czech Republic

The prism-based surface plasmon resonance (SPR) technique has some shortcomings, such as large size of a setup and high cost, which makes it unsuitable for example miniaturized applications, etc. These troubles can be overcome by a setup with optical fiber. In this SPR-based fiber-optic sensor, the cladding is removed from the middle portion of the fiber and a metal layer is coated on the unclad portion. Polychromatic light is used either as a collimated source (light is launched into the fiber using a launching system) or the light emitting diode with a Gaussian spectral profile as a diffuse source [1]. The SPR-based fiber-optic sensor refractive sensor utilizes the dependence of the resonance wavelength on the refractive index of an analyte. The sensitivity of the sensor can be improved by various modifications [2].

This paper deals with a theoretical study of the sensitivity of the SPR-based fiber-optic refractive index sensor with a collimated source of light. Ag is used as a metal layer. Influence of the SPR spectra of the SPR fiber-optic probe on the critical angle was investigated. Influence of the additional dielectric Si-layer of high refractive index between the metal and the analyte was studied too.

If we assume the collimated beam which is focused on the face of the fiber at axial point (skew rays are not considered), the power transmitted through the fiber is given as [2]

$$P_{trans} = \frac{\int_{\theta_{cr}}^{\pi/2} R_p^{N_{ref}(\theta)} \frac{n_1^2 \sin\theta\cos\theta}{\left(1-n_1^2\cos^2\theta\right)^2} \mathrm{d}\theta}{\int_{\theta_{cr}}^{\pi/2} \frac{n_1^2 \sin\theta\cos\theta}{\left(1-n_1^2\cos^2\theta\right)^2} \mathrm{d}\theta}, \tag{1}$$

where θ is the angle of refraction at the core-cladding interface, n_1 is the refractive index of the fiber core (fused silica), R_p is the net reflectance (for *p*-polarized light) of the ray incident at the core-metal interface and n_2 is the refractive index of the fiber cladding. The critical angle of the fiber θ_{cr} and number of reflections the ray of angle θ undergoes inside the fiber are defined as

$$\theta_{cr} = \sin^{-1}\left(\frac{n_2}{n_1}\right), \tag{2}$$

$$N_{ref}(\theta) = \frac{L}{D\tan\theta}, \tag{3}$$

where L is the length of the sensing region and D is the diameter of the core. The sensitivity of the SPR sensor with spectral interrogation is defined as

$$S_n = \frac{\delta\lambda_{reson}}{\delta n_{analyte}}, \tag{4}$$

where $\delta n_{\mathrm{analyte}}$ and $\delta\lambda_{reson}$ are the refractive index difference of the analyte and the resonance wavelength shift, respectively.

Fresnel equations and data from literature for the SPR-based fiber-optic sensing structure were used for modeling. The complex refractive index of the metal thin-film was

calculated from the Drude model, the critical angle of the fiber is calculated form Eq. (2), the sensing length is 1 cm, the refractive index of analyte lies between 1.33 and 1.36.

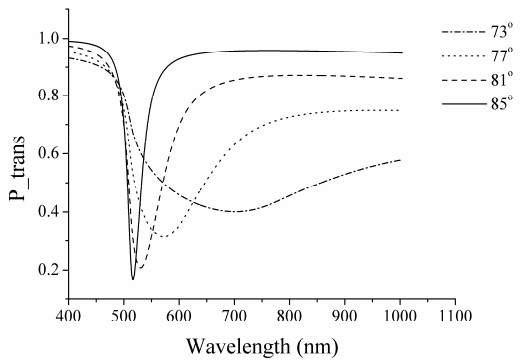

Fig. 1 Variation of the SPR spectra of the SPR fiber-optic probe with the critical angle. The core diameter of the fiber is 600 μm, the refractive index of the analyte n = 1.6, the Ag-thin film thickness is 40 nm.

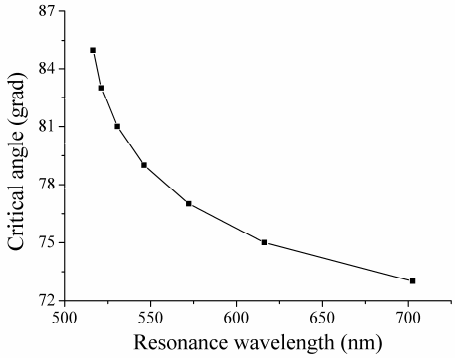

Fig. 2 Dependence of the resonance wavelength on the critical angle. The core diameter of the fiber is 600 μm, the refractive index of the analyte n = 1.6, the Ag-thin film thickness is 40 nm.

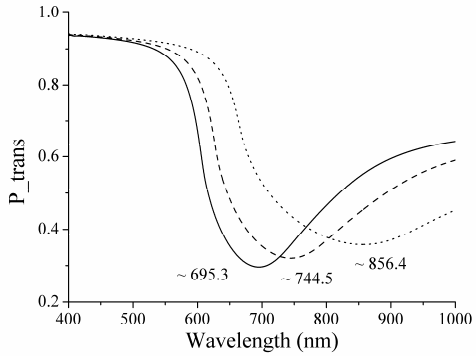

Fig. 3 SPR spectra of the SPR fiber-optic probe for a Si-layer of 4 nm thickness for refractive indexes: n = 1.33 (solid), n = 1.34 (dashed), n = 1.355 (dotted). The critical angle for all cases is 74.3°. The core diameter of the fiber is 600 μm.

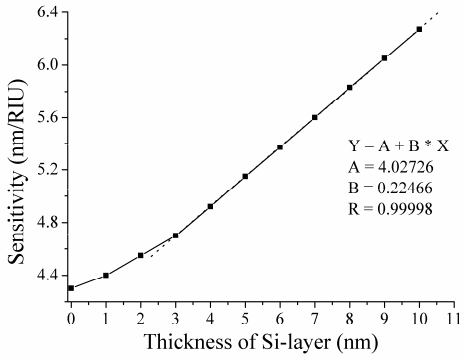

Fig. 4 Dependence of sensitivity of the SPR sensor on the Si-layer thickness. The dotted line corresponds to the linear fit for the Si-layer thickness greater than 3 nm. The critical angle for all cases is 74.3°. The core diameter of the fiber is 600 μm

This theoretical study illustrates significant variation of the SPR spectra of the SPR fiber-optic probe with the critical angle (see Figs. 1 and 2) which is important when we suppose wavelength dependence of the refractive indices of the fiber core and fiber cladding. The SPR sensor with additional Si-layer (see Fig. 3) leads to increase of sensitivity. There is linear dependence between the Si-layer thickness and the sensitivity for the Si-layer thicknesses greater than 3 nm (see Fig. 4). In addition, important advantage of the additional layer, especially for Ag, is the oxidation protection of the metal.

This work was partially supported by the Czech Science Foundation (project No. P102/11/0675) and by the regional Grant CZ. 1.05/2.1.00/01.0040.

[1] S. K. Srivastava, R. K. Verma, B. D. Gupta, Applied Optics 48 (2009) 3798.
[2] P. Bhatia, B. D. Gupta, Applied Optics 50 (2011) 2032.

SIMULATION OF A SURFACE PLASMON RESONANCE-BASED REFRACTIVE INDEX SENSOR USING SPECTRAL INTERFERENCE

J. Luňáček[(a)], M. Luňáčková[(b)], P. Hlubina[(a)], D. Ciprian[(a)]

(a) Department of Physics, VŠB - Technical University of Ostrava, 17. listopadu 15, 708 33 Ostrava - Poruba, Czech Republic
(b) Department of Mathematics and Descriptive Geometry, VŠB - Technical University of Ostrava, 17. listopadu 15, 708 33 Ostrava - Poruba, Czech Republic

In recent years, a large amount of work has been carried out in the field of surface plasmon resonance (SPR)-based sensors [1]. The SPR sensors have been showed as a useful tool for many applications, for instance in biology and chemistry [1]. One of the SPR techniques utilizes the Kretschmann configuration to excite surface plasmons. In this paper, a novel white-light spectral interferometric technique is used to retrieve the ellipsometric phase [2] from the interferograms recorded for a prism/metal/analyte sensing structure in the Kretschmann configuration. We suppose that the prism is made of fused silica, the metal is Au or Ag, and the analyte is supposed to be liquid. This technique utilizes the polarimetry configuration with a birefringent crystal, a polarizer and an analyzer that allows to obtain channeled spectrum for *p*- and *s*-polarized waves, as described in [2].

Complex reflection coefficients of *p*- and *s*-polarized components are affected by the structure and can be written by the following equation [2]

$$r_{p,s}(\lambda) = \sqrt{R_{p,s}(\lambda)}\exp[i\delta_{p,s}(\lambda)], \tag{1}$$

where $R_{p,s}(\lambda)$ and $\delta_{p,s}(\lambda)$ are the spectral reflectances and phase changes on reflection from the structure for both polarization, respectively. The two orthogonally polarized components retarded by the birefringent crystal and the structure are mixed with the analyzer oriented 45° with respect to the plane of incidence of the Kretschmann configuration and their interference is resolved by a spectrometer as a channeled spectrum (see a setup in [2]). The information retrieved from the channeled spectra is the ellipsometric phase $\Delta(\lambda) = \delta_p(\lambda) - \delta_s(\lambda)$.

In order to retrieve the wavelength-dependent phase function – the ellipsometric phase $\Delta(\lambda)$ – from the recorded channeled spectra, the measurement procedure consists of two steps. In the first step (without the analyte) – the reference channeled spectrum is recorded, and in the second step (with the analyte) – the test channeled spectrum is recorded, as was described in detail in [2]. The spectral signals from which the phase functions can be retrieved are defined as

$$S(\lambda) = V(\lambda)\cos[\Phi_{BC}(\lambda) + \Delta(\lambda)], \tag{2}$$

where $V(\lambda)$ is the visibility function and $\Phi_{BC}(\lambda)$ is the retardance of the birefringent crystal used in setup [2]. In the first step $\Delta(\lambda) = 0$ and the reference signal is measured. In the second step the test signal $S(\lambda)$ is measured and in order to retrieve the ellipsometric phase $\Delta(\lambda)$ from both spectral signals, a windowed Fourier transform (WFT) can be applied [3].

Fresnel equations and data from literature for the prism/metal/analyte sensing structure were used for modeling. The thickness of the metal thin-film is 50 nm (the complex refractive index was calculated from the Drude model), the angle of incidence is 75°, the thickness of birefringent crystal is 4 mm and the refractive index of analyte lies between 1.33 and 1.34.

The ellipsometric phases are shown in Figs. 1a) and 1b). Examples of the simulated spectral signals based on Eqs. (1) and (2) are presented in Figs. 2a) and 2b). These figures demonstrate two aspects: the fringes visibility is significantly lowered at the resonance

wavelength and the phase jump is apparent. The resonance wavelengths are in the case of Au 706.76 nm for n = 1.33 and 770.07 nm for n = 1.34, respectively, in the case of Ag 602.35 nm for n = 1.33 and 653.13 nm for n = 1.34, respectively.

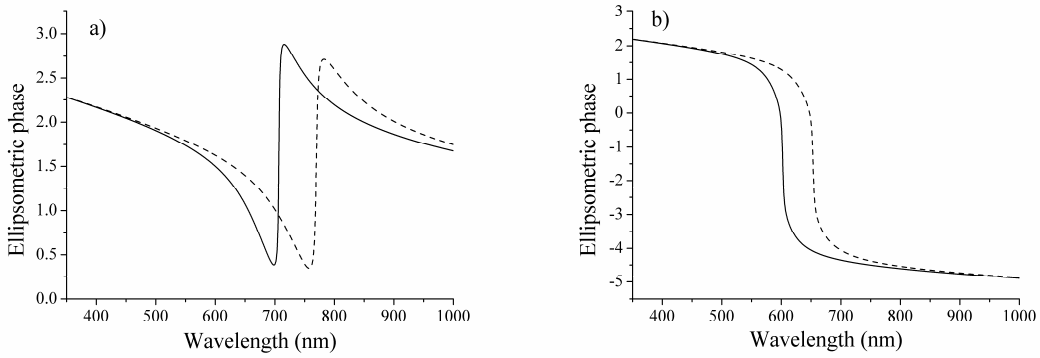

Fig. 1 Ellipsometric phase obtained from the Fresnel equations, a) Au, b) Ag. Solid lines correspond to the refractive index n = 1.33 of the analyte and the dashed lines correspond to n = 1.34.

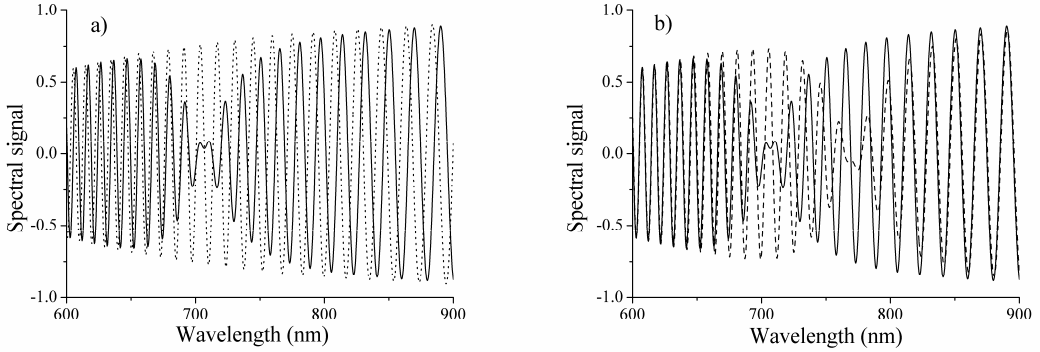

Fig. 2 Examples of the theoretical spectral signals for Au. Solid line in Fig 2a) illustrates existence of the SPR effect (the refractive index of the analyte is n = 1.33). Dotted line is without the SPR effect. Fig 2b) demonstrates the fringe shift (the ellipsometric phase shift) with the change of the refractive index of the analyte (solid line n = 1.33, dashed line n = 1.34).

The theoretical sensitivity is defined as $\delta\lambda_{rez}/\delta n_{sens}$ [4], where δn_{sens} is the change of the refractive index and $\delta\lambda_{rez}$ is the corresponding shift in the resonance wavelength. For instance, the theoretical sensitivity of our sensor configuration based on the spectral phase retrieval can be estimated for refractive indices range from 1.33 to 1.34 as 6.33 μm/RIU and 5.08 μm/RIU, for 50 nm Au and Ag films, respectively.

We have simulated a novel SPR-based refractive index sensor using the spectral phase retrieval from the spectral interference signals. The SPR sensor detects the ellipsometric phase shift which depends on the change of the refractive index of the analyte.

This work was partially supported by the Czech Science Foundation (project No. P102/11/0675) and by the regional Grant CZ. 1.05/2.1.00/01.0040.

[1] A. K. Sharma, R. Jha, B. D. Gupta, IEEE Sensors J. 7 (2007) 1118.
[2] P. Hlubina, D. Ciprian, J. Luňáček, Opt. Lett. 34 (2009) 2661.
[3] P. Hlubina, J. Luňáček, D. Ciprian, R. Chlebus, Opt. Comm. 281 (2008) 2349.
[4] P. Bhatia, B. D. Gupta, Appl. Opt. 50 (2011) 2032.

Pr^{3+}-DOPED ALUMINUM GARNET CRYSTALS AND LAYERS

J.A. Mareš [(a)], A. Beitlerová [(a)], M. Nikl [(a)], K. Nitsch [(a)], M. Kučera [(b)] and M. Hanuš [(b)]

(a) Institute of Physics, Academy of Sciences of the Czech Republic, Cukrovarnická 10, 162 53 Prague 6, Czech Republic

(b) Charles University, Faculty of Mathematics and Physics, Ke Karlovu 5, 12 116 Prague 2, Czech Republic

Ce^{3+}-doped inorganic crystals (e.g. aluminum garnets or perovskites) are used in different imaging applications as PET, PEM, gamma cameras etc. [1-4]. But a few years ago, Pr^{3+}-doped crystals started to be studied, especially Pr^{3+}-doped (Lu,Y) aluminum garnets ($Lu_3Al_5O_{12}$ – LuAG or $Y_3Al_5O_{12}$ – YAG) [4-7]. Ce^{3+}- or Pr^{3+}-doped (Lu,Y) aluminum garnets behaves similarly but their emission spectra are quite different. Ce^{3+}- doped LuAG or YAG crystals exhibit visible emission (λ_{peak} ~ 500-550 nm [1]) while those of Pr^{3+}-doped ones have UV emission peaking at ~ 310 nm [2,3]. LuAG or YAG crystals were prepared by the Czochralski method[1]) but also mixed $Lu_xY_{1-x}AG$ crystals were grown and finally also thin epitaxial layers were prepared by LPE method by some of us [6].

The aim of this talk is to present (i) scintillation properties of Pr^{3+}-doped LuAG, YAG, mixed $Lu_xY_{1-x}AG$ crystals and LPE grown epitaxial layers and (ii) to show how annealing can influence their scintillation properties.

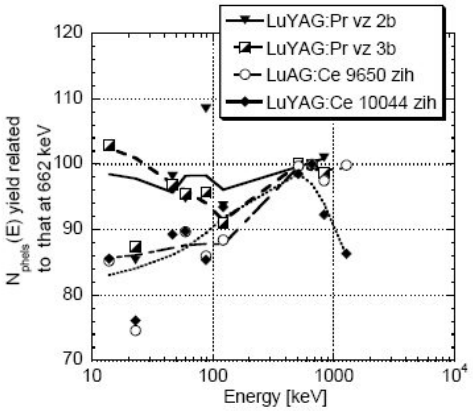

Fig. 1 Non-proportionality of $N_{phels}(E)$ photo-electron yield of selected Pr^{3+} and Ce^{3+}-doped LuAG and LuYAG crystals

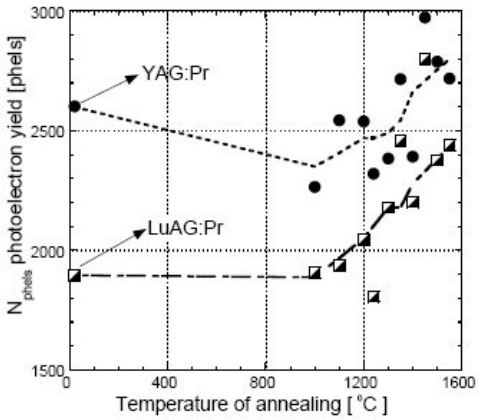

Fig. 2 Detailed studies of changes of N_{phels} photo-electron yield (per 1 MeV) of Pr^{3+}-doped LuAG and YAG crystals

One of the most important scintillating properties is so called „non-proportionality" of N_{phels} photoelectron scintillation yield. Here, $N_{phels}(E)$ photoelectron yield is measured using a HPMT in the energy range 10 – 1300 keV [1-3]. Non-proportionality means a deviation of $N_{phels}(E)$ yield measured for the same energy unit to that measured at the energy of ^{137}Cs γ-ray line (energy 662 keV [2]). Fig. 1 shows that mixed $Lu_xY_{1-x}AG$:Pr crystals exhibit small non-proportionality or low deviation from energy unit in the whole energy range 10 – 1300 keV.

[1]) Ce^{3+}or Pr^{3+}-doped LuAG, YAG or $Lu_xY_{1-x}AG$ crystals were grown at company Crytur Ltd., Palackeho 175, 511 01 Turnov, Czech Republic

Non-proportionality of LuAG:Ce and LuYAG:Ce crystals is higher compared to that observed on Lu_xY_{1-x}AG:Pr crystals (see Fig. 1) and at low energies their deviation at energy unit is less of about 10 - 20 % compared to that at 662 keV. Common observation from non-proportionality of Pr^{3+}- or Ce^{3+}-doped (Lu,Y)AG crystals resulted in observation that Pr^{3+}-doped ones exhibit much lower non-proportionality than those of Ce^{3+}-doped ones.
Table 1 present short summary of N_{phels} photoelectron and L.Y. yields and energy resolution at 662 keV. Now, this Tab. 1 shows that L.Y. of Ce^{3+}-doped pure Lu or mixed Lu_xY_{1-x} garnets are higher than those of Pr^{3+}-doped ones.

Sample	mm	N_{phels}(1μs)	L.Y.(1μs)	FWHM	N_{phels}(10μs)	L.Y.(10μs)	FWHM
LuYAG:Pr(2b)	1.3	2606.5	10639	14.1	3886.9	15865	2.1
LuYAG:Pr(3b)	1.4	3801.1	15084	7.3	4136.9	16416	3.2
LuAG:Ce al	0.8	1961.1	14420	5.1	3189.5	23471	2
LuYAG:Ce al	0.8	2093.4	18859.5	10.1	2607.4	23490	4.2

Tab. 1 N_{phels} photo-electron and L.Y.'yields (per 1 MeV) and FWHM at 662 keV of samples presented in Fig. 1 (al means that samples were annealed in air at ~ 1300 ^{0}C for 48 hours)

Besides (Lu,Y)AG:Pr crystals also thin epitaxial layers (thickness ~ 10 μm) were prepared (by LPE method) and studied. Details of their scintillation studies were presented a year ago at EURODIM'2011 conference [6]. Generally, N_{phels} photoelectron yields of both LuAG:Pr crystals and those of selected epitaxial layers are roughly the same or even a bit higher (these studies were carried out using α-particle excitation [6]). Another development of Pr^{3+}-doped LuAG is connected with development of LuAG:Pr ceramics [7] but these samples exhibit lower N_{phels} photoelectron yields that those of their crystal analogues.

Besides development of Pr^{3+}-doped crystals, layers and ceramics there are also efforts to increase their N_{phels} photo-electron yield. N_{phels} yield can be influenced due to annealing in different atmospheres. Here, we used annealing in air at different temperatures starting from 1000 ^{0}C. Fig. 2 shows an influence of annealing in air in the temperature range 1000 – 1550 ^{0}C. We clearly see that the N_{phels} yield increases both for LuAG:Pr and YAG:Pr crystals of about 26 % or 11 %, respectively. This increase should be caused due to changes in crystals on microscopic scale (more Pr^{3+} dopants change their charge state to 3+)

References

[1] J.A. Mares, A. Beitlerova, M. Nikl, A. Vedda, C.D'Ambrosio, K. Blazek and K. Nejezchleb, phys. stat. sol. (c) 4 (2007) 996.
[2] J.A. Mares and C. D'Ambrosio, Opt. Mat. 30 (2007) 22.
[3] J.A. Mares, M. Nikl, K. Blazek, K. Nejezchleb and C.D'Ambrosio, Proc. 8-th Inter. Conf. Inorganic Scintillators and their Use in Scientific and Industrial Applications - SCINT'05, NAS, Ukrajina, Kharkov (2006), p. 138.
[4] J. Pejchal, M. Nikl, E. Mihokova, J.A. Mares, A. Yoshikawa, H. Ogino, K.M. Schillemat, A. Krasnikov et al., J. Phys. D: Appl. Phys. 42 (2009) 055117.
[5] A. Yoshikawa, T. Yanagida, K. Kamada, Y. Yokota et al., Opt. Mat. 32 (2010) 1294.
[6] M. Kucera, P. Prusa, J.A. Mares, M. Nikl, K. Nitsch, M. Hanus et al., IOP Conf. Series, Materials Science and Engineering 15 (2010), pp. 012012-(1-9).
[7] Yun Shi, Martin Nikl, Xiqi Feng, Jiri A. Mares, Yiqiang Shen, A. Beitlerova, R. Kucerkova, Yubai Pan and Qian Liu, J. Appl. Phys. 109 (2011) 013522-1-7.

MEASUREMENT POSSIBILITIES OF MECHANICAL PROPERTIES OF SOLDERED JOINTS

M. Martinkovič, R. Koleňák

Slovak University of Technology Bratislava, Faculty of Materials Science and Technology in Trnava, Institute of Production Technologies, J. Bottu 25, 917 24 Trnava

Introduction

There has been significant research to improve properties of lead free-solders during last years [1]. To improve properties of lead free-solders it is necessary to measure mechanical properties of solder joints. To investigate the relations between microstructure and mechanical properties of these joints and compare new lead free-solders joints properties with led ones required exact results independent on measurement condition. Also exact technological conditions during preparation of specimens and their geometry must be complying.

Preparation of different experimental soldered joints types

Three types of experimental soldered joints were prepared on a hot plate with flux BrazeTec Soldaflux 7000. Joint material copper and solder Sn3.5Ag0.7Cu was used. The joints were created at 270°C, holding time 10 s. Finished joints were subsequently cooled on a stainless steel pad. First type of experimental soldered joint - soldereded lap joint (see fig. 1) is prepared from sheets with size 20 x 10 x 0.8 mm. To ensure immobility during the process a special facility from aluminium was designed. Second type – scarf butt joint (see fig. 2) is prepared from sheets with size 20 x 10 x 1.5 mm, scarf angle 45°. To ensure immobility during the process a special facility from aluminium was designed.

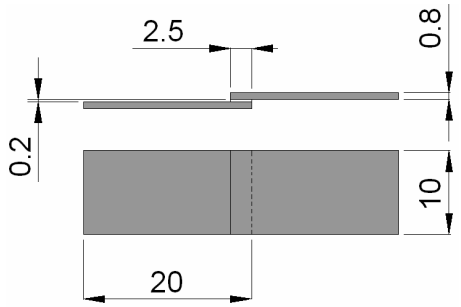

Fig. 1: Soldered lap joint

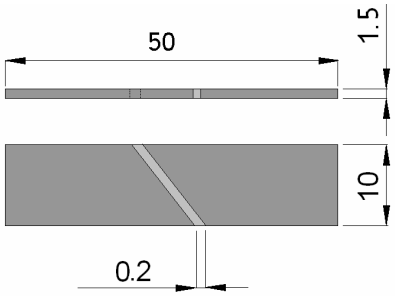

Fig. 2: Soldered scarf-butt joint

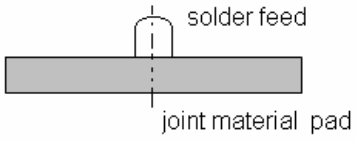

Fig. 3: Soldered feed joint

Third type - soldered feed with diameter 5 mm and high 2.5 mm on joint material pad with diameter 16mm and high 1.5mm (see fig. 3) is prepared using special facility from aluminium

Mechanical properties measurement

FPZ 100/1 universal testing machine was used. Deformation rate was 2 $mm.min^{-1}$. In case of soldered feed joint shear strength adaptor was used [2]. Shear strength and toughness – relative fracture energy of all joints were measured. Fracture toughness was calculated from area under the curve in force-displacement diagram up to maximum force. The shear strengths of solder joints were determined by dividing the maximum load by the area of the solder joints, in case of scarf butt joint by the area of the cross section of sheet an dividing by two (maximum shear stress in plane with 45° orientation to force is equal one half of normal stress). The measurement of relative fracture energy in case of lap and scarf-butt joints were not successful, the results had very great dispersion. On the other hand measurement of shear strength was successful in al three cases; dispersion was from 5 to 8%. Measured mean shear strengths of lap joint was 40 MPa, scarf-butt joint 31,5 MPa and feed joint 37 MPa.

Discussion and conclusion

These three measurement methods of mechanical properties of soldered joints can be used for experimental measurements of soldered joints mechanical properties. Soldered lap joints probe and scarf-butt joint led only to obtaining of shear strength, but solder feed probe can be used to obtain not only value of shear strength, but fracture energy – toughness of bond too. For research of solders it is necessary preparation of experimental joints with exactly defined conditions and geometry and consequential its mechanical properties measurement with exactly defined conditions too. In case of solder lap joint observance of preparation conditions is not as easy as in second ones. Observance of preparation conditions is easiest in case of solder feed joint. During mechanical testing of solder lap joint in addition to tensile load also bending moment is effected and cannot be eliminated. In case of solder feed joint shear stress load is affected by bending moment too, but its value is minimal. During mechanical testing of experimental scarf-butt joint pure tension load is affected with maximum value of shear strength in soldered joint plane.

This work was supported by VEGA Grant No. 1/0211/11 and KEGA Grant No. 327-010STU-4/2010 *which are supported by Slovak Republic Ministry of Education*

Literature

[1] Martinkovič, Maroš - Drienovský, Marián: Comparison of mechanical properties and microstructure of lead-free solders and soldered joints. In: Acta Metallurgica Slovaca Conference. No. 1, (2010), Special Issue: 14th International Symposium on Metallography, pp. 277-280

[2] Martinkovič, Maroš - Koleňák, Roman - Pocisková Dimová, Katarína: Measurement methods of mechanical properties of solders and soldered joints. In: Development of Materials Science in Research and Educations: Proceedings of 20th Joint Seminar. Praha: CSACG 2010, pp. 49-50

STRUCTURE AND PROPERTIES OF $PbO-TeO_2-P_2O_5$ GLASSES

P. Mošner [(a)], K. Vosejpková [(a)], S. Köhler [(b)], L. Koudelka [(a)]

(a) Department of General and Inorganic Chemistry, Faculty of Chemical Technology, University of Pardubice, 532 10 Pardubice, Czech Republic
(b) Otto-Schott-Institute, Friedrich-Schiller-University, D-07743 Jena, Germany

Tellurium and phosphorus oxide based glasses have been studied in recent years as promising materials for various applications because of their low melting temperature and glass transition temperature, low viscosity, high thermal expansion, high refractive indices, etc [1]. In the binary $TeO_2-P_2O_5$ system homogeneous glasses were obtained within the range of 2-26 mol% P_2O_5 [1-3]. Structural studies of tellurite glasses revealed that pure TeO_2 consists only of TeO_4 trigonal bipyramids [4]. Vitreous P_2O_5 has a three-dimensional structural network consisting of PO_4 tetrahedra interconnected by P-O-P bonds. In the $TeO_2-P_2O_5$ system within the region of homogeneous glasses TeO_4 units convert into TeO_{3+1} units with increasing P_2O_5 content [2]. Thermal studies [3] of binary $TeO_2-P_2O_5$ glasses showed, that with increasing P_2O_5 content up to ~28 mol% their thermal expansion coefficient slightly decreases, whereas the glass transition temperature increases. Additional increase of P_2O_5 content leads contrary to decrease of glass transition temperature and to an increase of thermal expansion coefficient.

The aim of this work is to study the structure, physico-chemical and thermal properties of $PbO-P_2O_5-TeO_2$ glasses as a function of TeO_2 content. $PbO-P_2O_5-TeO_2$ glasses were studied in two compositional series $(100-x)[0.5PbO-0.5P_2O_5]-xTeO_2$ (X-series) and $50PbO-(50-y)P_2O_5-yTeO_2$ (Y-series), within the compositional regions of x=0-80 and y=0-25 mol% TeO_2. The obtained glasses were characterized by the measurements of density, molar volume, chemical durability, glass transition temperature, dilatation softening temperature, crystallization temperature and thermal expansion coefficient. Their structure was studied by Raman spectroscopy.

Study of physico-chemical properties showed that glass density linearly increases with increasing TeO_2, whereas molar volume decreases in both glass series within the range 39.4-30.4 cm^3mol^{-1}. Chemical durability against water remains practically constant. Colour of the glasses changed from clear (x,y=0) to yellowish.

DSC curve of the starting metaphosphate glass $50PbO-50P_2O_5$ (Fig.1A) is characterized by a weak endothermic effect at ~331°C corresponding to the glass transition phenomenon, which is followed by a sharp exothermic peak with the onset at 377 °C ascribed to the crystallization of $Pb(PO_3)_2$ compound from the glassy matrix and finally by a broad endothermic peak with the onset at 665 °C corresponding to the melting of crystalline $Pb(PO_3)_2$ as seen from XRD pattern of the glass sample heated up to 600°C (Fig.1B). DSC curves of TeO_2-containing glasses (Fig.1A) suggest that most of their solidified melts crystallize on heating usually in 2-3 steps within the range ~370-550°C. The highest thermal stability was found for the glasses containing 20, 30, 40 and 70 mol% TeO_2 (X series of glasses), on whose DSC curves were identified no crystallization peaks.

Dilatometric curves showed that values of thermal expansion coefficient do not change significantly with the increasing TeO_2 content in the glasses. The values of glass transition temperature and dilatometric softening temperature increase with increasing TeO_2 content in both compositional series having a maximum x=50 mol% and y=20 mol%TeO_2.

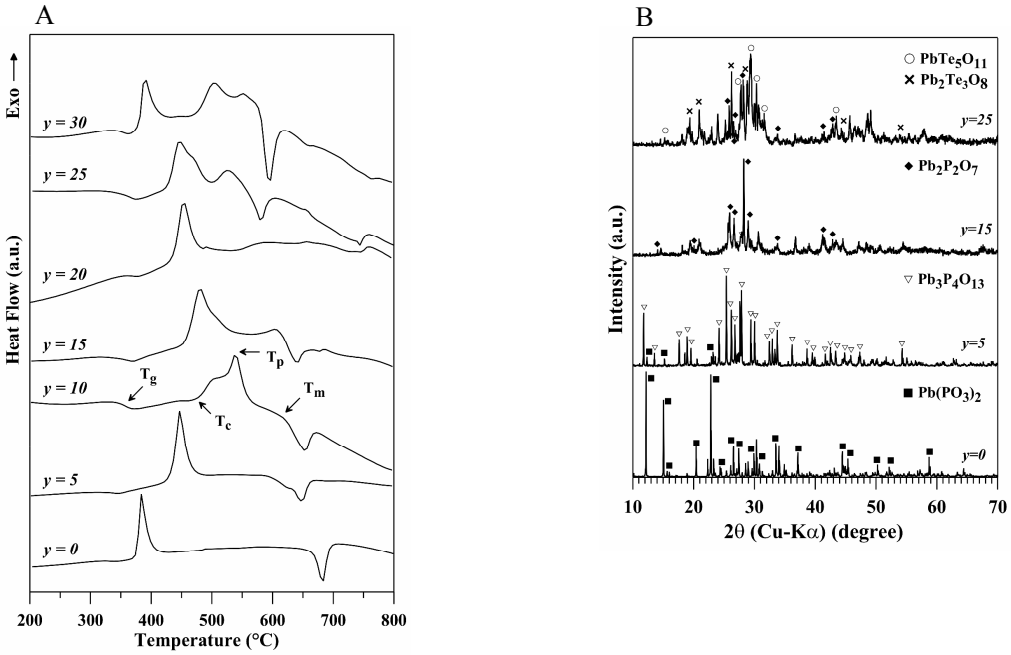

Fig.1A. DSC curves of the 50PbO-(50-y)P_2O_5-yTeO_2 glasses.
Fig.1B. XRD patterns of the crystallized samples of the series 50PbO-(50-y)P_2O_5-yTeO_2.

The Raman spectrum of the parent 50PbO-50P_2O_5 glass showed a pattern typical of metaphosphate glasses with vibrational bands at 687, 1155 and 1220 cm^{-1}. Raman spectra of the glasses containing TeO_2 revealed the incorporation of TeO_x structural units into the disordered network of the glasses and the depolymerization of phosphate chains in the glasses. At a high TeO_2 content isolated PO_4 tetrahedra are predominantly formed in the structure of glass series X, while both diphosphate O_3P-O-PO_3 and isolated PO_4 groups are present in the structure of the glass with the highest TeO_2 content in series Y. In the structure of glass series Y tellurium atoms form predominantly TeO_3 trigonal pyramids, whereas in the X glass series TeO_4 trigonal bipyramids prevail in the glass structure.

[1] El-Mallawany, Tellurite Glasses Handbook, CRC Press, Boca Raton, 2002.
[2] S. Neov, I. Gerasimova, V. Kozhukharov, M. Marinov, J. Mater. Sci. 15 (1980) 1153.
[3] N. Mochida, T. Sekiya, A. Ohtsuka, M. Tonokawa, J. Ceram. Soc. Jpn. 96 (1988) 973.
[4] T. Sekiya, N. Mochida, A. Ohtsuka, M. Tonokawa, Nippon Seramikkusu Kyokai Gakujutsu Ronbunshi 97 (1989) 1435.

The authors are grateful for the financial support from the research project No. 0021627501 of the Ministry of Education of Czech Republic and to the Grant Agency of the Czech Republic (Grant No. P106/10/0283).

STUDY ON CRYSTALLIZATION KINETICS OF UNDERCOOLED MELTS

K. Nitsch, A. Cihlář, R. Král and M. Rodová

Institute of Physics AS CR, Cukrovarnická 10, 162 00 Praha 6, Czech Republic

Experimental examination of crystallization running in un undercooled melt at temperature above the glass transformation is of great importance for both the preparation of stable glasses resistant to crystallization and the preparation of first quality glassy ceramics. The crystallization consists of two processes – nucleation and crystal growth. During the nucleation, either homogeneous or heterogeneous, stable nuclei are formed, which later grow up to a macroscopic size [1]. Under isothermal conditions both of these processes occur simultaneously and the time dependence of the crystallized volume fraction α in the undercooled melt is given by the generalized Johnson-Mehl-Avrami-Yerofyeyev-Kolmogorov (JMAYK) equation [2,3]

$$\alpha(t) = \frac{V(t)}{V_0} = 1 - \exp\left[- g \int_0^t I(t') \left[\int_{t'}^{t} U(t'')dt'' \right]^{\mathrm{m}} \mathrm{d}t' \right], \qquad (1)$$

where g is the shape factor, V_0 is the initial volume of the system, $V(t)$ the volume of the newly formed crystalline phase, I denotes the nucleation rate and $U(t'')$ is the growth rate. Both of integrals in (1) go over time. If the nucleation and growth rates are known as a function of time and temperature the dependence of the crystallized volume fraction α on these variable quantities can be calculated.

Experimental determination of number the density of nuclei and the rates of nucleation and growth in the tested undercooled melt is quite a difficult task when several measurements are performed at various temperatures and times [2]. Critical nuclei in a nanometer size are first formed at a nucleation temperature when their growth rate is extremely slow. Then the sample is heated on a higher (growth) temperature at which the nuclei are not formed but grow up to a detectable size. This method based on microscopic observation was developed by Tammann [4] many years ago and is widely used [2,3]. Due to extremely long experimental time (one experiment can often past even several days) the thermoanalytical methods such as DTA and DSC are used because of fast availability of experimental data.

The DSC or DTA measurements are performed at both constant temperature and constant heating rate but measurements under non-isothermal conditions at a constant heating rate are preferred. Of these measurements only macroscopic idea about the crystallization process can be obtained. Measured heat flow is proportional to the crystallization heat and the area of the exothermic effect registered by the thermal curve is proportional to the amount of the melt crystallized. The crystallized volume fraction α can be calculated from this area for every time and temperature intervals of the transformation process. The overall crystallization kinetics can be theoretically described by a relation proposed by Avrami in which the crystallized volume fraction α is a function of time

$$\alpha(\tau) = 1 - \exp\left[- k(t)^n \right]. \qquad (2)$$

In this so-called Johnson-Mehl-Avrami (JMA) equation t is the time, n the Avrami exponent and k is the effective overall rate constant given by $k = A\exp(-E_C/RT)$, where

E_C is the apparent activation energy for crystallization and A is the frequency factor. Description of the crystallization process is based on the determination of the Avrami kinetic exponent *n,* the activation energy for crystallization E_C, and the pre-exponential factor A [5].

The JMA theory was originally derived for isothermal condition but it can be, under some assumptions, also used for the study of the crystallization kinetics under non-isothermal conditions. During a non-isothermal DSC scan the sample temperature T increases linearly with time at a heating rate of β. After taking the JMA equation double logarithms and by inserting the temperature increase $T = \beta t + T_0$ in time, the relation is received

$$\ln\left[-\ln(1-\alpha)\right] = n\ln\left[(T-T_0)\right] + n\ln k - n\ln\beta \,, \tag{3}$$

where T_0 is the initial temperature. This makes it possible to calculate the Avrami exponent *n* and to determine the crystallization mechanism of a new phase.

The effective activation energy for the crystallization E_C can be calculated by relations proposed by Kissinger

$$\ln\ \frac{\beta}{T_P^2}\ = -\frac{E_C}{RT_P} + \ln\ \frac{AR}{E_C} \tag{4}$$

and Ozawa

$$\ln\beta = -1.0516\frac{E_C}{RT_P} - const.\,, \tag{5}$$

where T_P is the crystallization peak temperature.

Using Kissinger equation, the frequency factor A can be computed in addition..

This work was supported from the Grant Agency of the AS CR (No. KAN 300100802*).*

[1] J.E. Shelby, Introduction to Glass Science and Technology, 2nd edition, RSC 2005, Cambridge UK.

[2] V.M. Fokin, N.S. Yuritsyn, E.D. Zanotto, in Nucleation Theory and Applications, Wiley-VCH Weinheim 2005, J.W.P. Schmelzer (Ed.), pp. 74-125.

[3] V.M. Fokin, A. Cabral Jr., M.L.F. Nascimento, E.D. Zanotto, J. Šesták, in Some Thermodynamic, Structural and Behavioral Aspects of Materials Accentuating Non-crystalline States, OPS Pilsen, J. Šesták, M. Holeček, J. Málek (Eds.), pp. 286-307, ISBN 978-80-87269-06-0.

[4] G. Tammann, Z. Phys. Chem. B25 (1898) 441.

[5] K. Nitsch, Experimentální metody studia krystalizace skel, Škola růstu krystalů 2006, Valtice, K. Nitsch and M. Rodová (Eds.), str. 31-40, ISBN 80-901 748-8-4.

GROWTH AND CHARACTERIZATION OF GARNET SCINTILLATION EPITAXIAL FILMS DOPED BY RARE-EARTH IONS

Z. Onderišinová [(a)], M. Hanuš [(a)], M. Kučera [(a)], M. Nikl [(b)], K. Nitsch [(b)], J. A. Mareš [(b)]

(a) Charles University, Faculty Math. Physics, Ke Karlovu 5, 12116 Prague, Czech Republic

(b) Institute of Physics, AS CR, Cukrovarnická 10, 162 00 Prague, Czech Republic

zonderisin@gmail.com

Scintillators represent one of the most popular system for detection high energy particles and photons. Rare-earth aluminum garnets are considered perspective scintillators with high density, fast scintillation response, high quantum efficiency and good chemical and mechanical stability. Thin garnet films are promising candidates for X-ray imaging and scintillation screens with micrometer resolution [1]. In this work we studied single crystalline rare-earth doped garnet films prepared by liquid phase epitaxy (LPE). The films were grown by isothermal dipping LPE from the flux onto lutetium (LuAG) and yttrium (YAG) aluminum garnet substrates of (111) crystallographic orientation. The LPE growth temperatures, *T*G, were as low as 1000 °C, while *T*G of Czochralski grown single crystal counterparts are around 2000 °C. Lower *T*G consequently leads to lower structural disorder and lower number of intrinsic crystal defects (e.g. antisite defects and oxygen vacancies) in films compared to bulk crystals. Such defects result in electron traps, which can evoke a loss of energy due to nonradiative transitions [2] and can induce a slow component in the scintillation decay.

The rare-earth doped garnet films prepared from the $PbO–B_2O_3$ flux exhibit good optical, emission, structural, and surface properties. The major drawbacks of the PbO flux are divalent and tetravalent Pb and Pt impurity ions which come from the flux and cannot be eliminated. We have recently demonstrated that the Ce-doped garnet films prepared from the lead-free $BaO–BaF_2–B_2O_3$ flux exhibit excellent optical and emission properties comparable to the Czochralski grown bulk crystals [3].

In this work our attention was primarily focused on the study of influence of co-doping with Sc^{3+} ions on the emission properties of rare-earth ions in garnet lattice, especially Tb^{3+} or Pr^{3+}, with the aim to increase additionally the light yield of the garnet samples. We have studied in detail the photo-luminescence (PL) and radio-luminescence (RL) properties, PL decay, and the photoelectron yield excited by alpha particles. The lowest absorption bands of 4f–5d parity allowed transitions of Pr^{3+} and Tb^{3+} ions are located near 280 nm and coincide with the Sc emission in the UV range. This could supports energy transfer from Sc^{3+} sensitizer to Tb^{3+} or Pr^{3+} activator ions and may additionally increase the emission output. The goal of this work is to study the effect of Sc co-doping on emission properties of Tb^{3+} ions for a wide range of Sc concentrations in order to find out optimal Sc and Pr doping providing maximal light yield.

The LuAG epitaxial layers doped with optimized concentrations of Sc and Pr ions and grown from the BaO flux have competitive radioluminescence and scintillation properties with the Czochralski grown single crystals. The integral radioluminescence of Sc co-doped samples was significantly higher compared to samples without Sc co-doping, Fig. 1. This was explained by the combined contribution of Sc and rare-earth ions in the RL spectra and

apparent energy transfer from Sc to Tb or Pr activator ions. Terbium Tb^{3+} photoluminescence decay was strictly one exponential with decay time of 3 – 3.2 ms, Fig. 2. The decay time was independent on the Tb and Sc content. This indicates that there is not any the nonradiative energy transfer from the emission centers due to the Sc co-doping. Detailed discussion and summary of emission and scintillation properties of Tb-Sc co-doped epitaxial films and comparison with bulk single crystals will be presented.

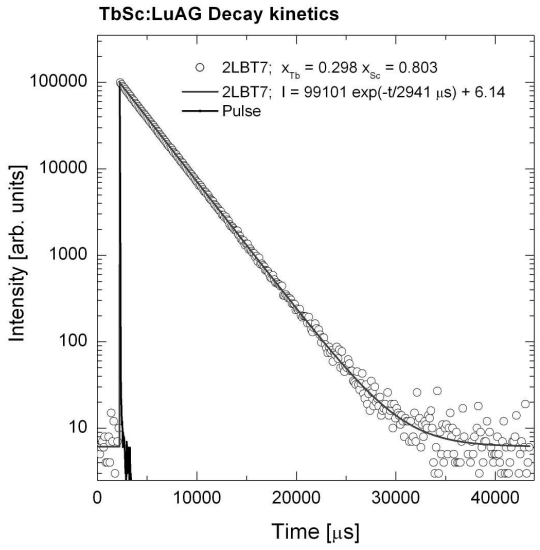

Fig. 1: Photoluminescence decay curve of TbSc:LuAG epitaxial film measured at λ_{em} = 543 nm, and excited in 5d(Tb^{3+}) band, λ_{ex} = 270 nm.

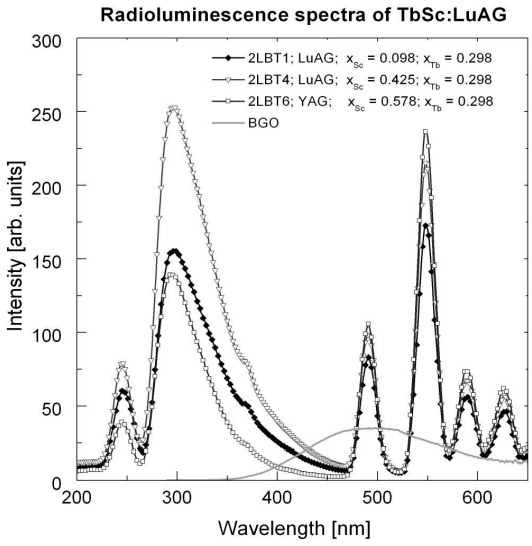

Fig. 2: X-ray excited radioluminescence spectra of TbSc:LuAG epitaxial films with various concentrations of Sc and Tb ions (shown in the legend).

[1] P. Horodyský, J. Touš, K. Blažek et al., Rad. Meas. 45 (2010) 628.

[2] M. Nikl, Phys. Status Solidi (a) 202 (2005) 201.

[3] M. Kučera, K. Nitsch, M. Kubová et al., IEEE Trans. Nucl. Sci. 55 (2008) 1201.

Acknowledgments:
This work was supported from the Grant Agency GA CR, grant 202/08/893, and by the grant SVV-2011-263306.

MATERIALS SCIENCE AND ENGINEERING —TRENDS AND ISSUES

B. Papánková

(a) Faculty of Chemical Technology, Slovak University of Technology, 812 37 Bratislava, Slovak Republic

What is Materials Science and Engineering? Materials Science and Engineering is an interdisciplinary branch of engineering that investigates the performance and properties of materials through manipulation of matter at the atomic and molecular length scales. A better understanding of structure-composition properties relations has lead to a remarkable progress in properties of materials.

Materials engineers will help to discover and synthesize materials for applications across all industries. They are involved in the extraction, development, processing, and testing of the materials used to create a diversity of products from computer chips and television screens to golf clubs and snow skis. They work with metals, ceramics, plastics, semiconductors and combinations of materials called composites to create new materials that meet certain mechanical, electrical and chemical requirements. Materials engineers have developed the ability to create and then study materials at an atomic level using advanced processes, electrons, neutrons, or x-rays and to replicate the characteristics of materials and their components with computers.

Chemists and Materials Scientists. Chemists who work in the field study how different combinations of molecules and materials result in different properties. They use this knowledge to synthesize new materials with special properties. Materials science is one of the hottest career areas in science, but to think of it as a single career is misleading. Perhaps one reason for its popularity is that it unites applications from many scientific disciplines that contribute to the development of new materials. Chemists play a predominant role in materials science because chemistry provides information about the structure and composition of materials as well as the processes to apply and synthesize them.

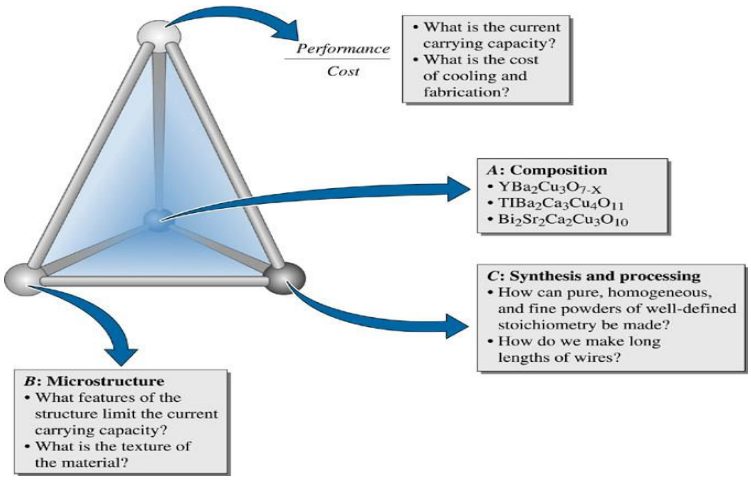

Figure 1. Application of the tetrahedron of materials science and engineering to ceramic superconductors. Note that the microstructure-synthesis and processing-composition are all interconnected and affect the performance-to-cost ratio.

Other applications of materials science include studies of superconducting materials, graphite materials, integrated-circuit chips, and fuel cells. Materials science is so interdisciplinary that preparation in a number of related areas is important.

Materials-Designated Departments - The materials science field is made up of people with various educational backgrounds. However, most projects in materials science are team efforts, and a team can include technicians, engineers, physicists, and materials scientists with Bc. or Ing. (Mgr.) degrees, as well as PhD. Chemist.

The fundamental core classes in materials-designated departments include:

»» Structures
»» Kinetics
»» Properties
»» Thermodynamics
»» Processing

Some students take additional classes outside the core. The courses selected are determined by students' research interests. Several departments require or recommend students who do not have materials background take an accelerated introductory-style course.

Materials World Modules

»»Composites
»»Concrete
»»Sports Materials
»»Environmental Catalysis
»»Introduction to the Nanoscale
»»Manipulation of Light in the Nanoworld
»»Biodegradable Materials
»»Biosensors
»»Food Packaging Materials
»»Nanotechnology Module
»»Ceramics
»»Polymers
»»Smart Sensors

Materials Chemistry Programs: There are about 20 degree programs in materials science in the United States, but most materials scientists recommend training in a more specific discipline, such as inorganic synthesis and organic chemistry, or specific materials science such as ceramic engineering. For example-University of Illinois includes two core courses - Advanced Materials Chemistry and Physical Methods in Materials Chemistry and an additional three from a list provided by the department. University of Wisconsin includes three required courses - Chemistry of Inorganic Materials; Chemistry of Organic Materials; and Materials Chemistry of Polymers , which may be substituted for another from an approved list. Faculty expertise, student composition, and institutional relationships define each department or program and its unique areas of interest.

In addition, traditional departments or programs that produce materials science specialists such as chemistry, physics, chemical engineering, electrical engineering, bioengineering, materials science and engineering, and other departments each have their own set of core concepts and have decided the appropriate breadth and depth of courses for their students.

Grant agencies are acknowledged for the financial support: VVCE 0004-07, VEGA 1/0052/11.

[1] The Future of Materials Science and Materials Engineering Education. A report from the Workshop on Materials Science and Materials Engineering Education; September 18-19, 2008 in Arlington, VA
[2] http://portal.acs.org
[3] Materials Science and Engineering for the 1990s, NRC, 1989
[4] Occupational Outlook, Bureau of Labor Statistics, 2002-2003

POSSIBILITY OF THERMODYNAMIC MODELLING OF PHASE TRANSFORMATIONS IN TOOL STEELS

M. Pašák, R. Čička, M. Behúlová

Institute of Materials Science, Faculty of Materials Science and Technology, Slovak University of Technology, 917 24 Trnava, Slovak Republic

Introduction

Recently, tool steels are very important materials used mainly for production of cutting, forming and other tools in industry. Usually they have to fulfill the extreme requirements on mechanical properties, such as hardness, strength and toughness. Often they are prepared by powder metallurgy process, when it is possible to get uniform carbide side and distribution even in large sections, and also to prepare materials with special compositions, impossible to prepare by melting and casting. The final step in producing of tool steels is heat treatment. As the properties of product are very dependent from phase composition and resulting microstructure, it is important to know the phase transitions and their kinetics, to optimize both the chemical composition and heat treatment parameters (temperatures, holding times, cooling rates). These materials processes can be described using thermodynamic models and computational thermodynamics.

Thermodynamics of phase transitions

Equilibrium state of system is characterized by minimum of Gibbs free energy, defined by G=H-TS, where H is enthalpy, T thermodynamic temperature and S entropy of system. The drivining force of all processes occurring in system is then the minimization of G. To calculate phase equilibria, computational softwares are available, e.g: Thermo-Calc, PANDAT, MTDATA, Thermosuite and FactSage. All these softwares use the same thermodynamic databases, where thermodynamic models and thermodynamic parameters of all components and phases of calculated system are given. The basic computational procedures are:

- map calculation: calculation of phase diagrams in binary systems, isoplethal (quasibinary) diagrams of higher-order systems, isothermal section or liquidus surface in ternary systems
- step conditions: calculation of selected thermodynamic quantity (phase fractions, compositions of phases, G, H, S of phases or system, heat capacity of system,…) dependent from T.

Using above mentioned software, it is possible to make only equilibrium calculations. In practice, this is rarely the case. Many phase transitions occur by diffusion processes (e.g.: precipitation) or by rapid diffusion less process (martensitic transformation). In these cases, more complex thermodynamic models have to be used [1].

Experiments

In experimental part, the phase equilibria of high-speed steel with composition given in Tab.1, were calculated using Thermocalc software TCW5, and thermodynamic database STEEL17X formulated by Kroupa [2]. The results are used at explaining the DTA measurement of powder of this steel, prepared by gas

Tab. 1: The chemical composition of tool steel

element	C	Si	Mn	Cr	Mo	V	W	Co
[wt%]	1,3	0,5	0,3	4,2	5	3	6,3	8,4

(nitrogen) atomization. DTA measurements were performed using STA NETZSCH 409 CD.

Conclusions

Computational thermodynamics is a fairly complex field, enabling to analyze phase transitions in multicomponent materials systems. The first results related to analysis of phase transitions in selected tool steel are shown.

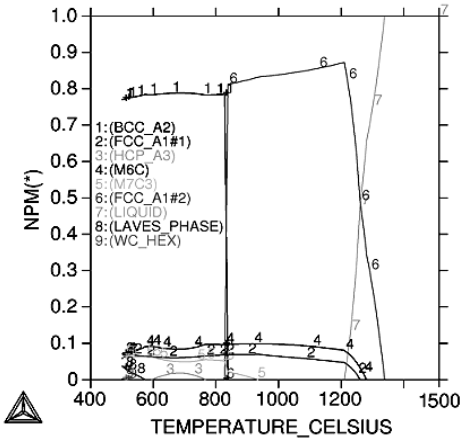

Fig. 1: Temperature dependence of molar fractions of phases in tool steel.

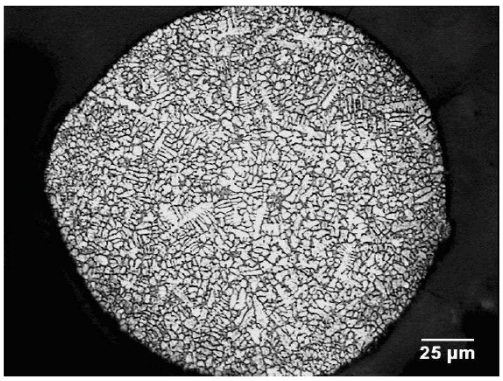

Fig. 4: Microstructure of powder particles after gas atomization; as-prepared state [3].

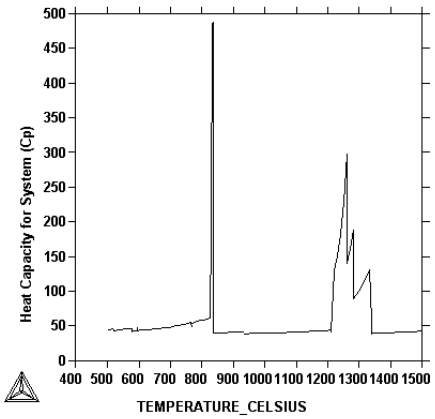

Fig. 2: Calculated heat capacity of tool steel.

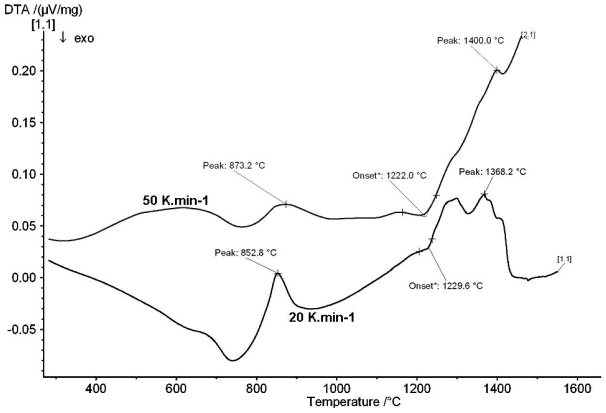

Fig. 3: DTA curves of tool steel powder; heating rate 20K.min^{-1} and 50K.min^{-1}.

[1] K. Janssens et al: Computational materials engineering, Elsevier, USA 2007, ISBN 13 978-0-12-369468-3

[2] A. Kroupa: personal communication

[3] M. Kapusňák: Influence of cobalt on internal porosity and microstructure of rapidly solidified particles and compacts of high speed steel S590 and S790 microclean, Diploma thesis, Trnava 2008.

***Acknowledgement**: Experimental works were realized within the frame of the project ITMS 26220120048 „Centre for Development and Application of Advanced Diagnostic Methods in the Processing of Metallic and Nonmetallic Materials“, and with financial support of scientific grant agency VEGA, Slovak Republic, project No. 1/0339/11.*

ANALOG AND NUMERICAL MODELING THE CONSTRICTION PHENOMENON ON COMPOSITES WITH CONDUCTIVE CARBON PARTICLES

I. Pilarčíková [(a)], S. Jirků [(a)], J. Hampl

(a) Czech Technical University, Faculty of Electrotechnical Engineering, Technická 2, 166 27 Prague, Czech Republic

The constriction phenomenon in polymer composites filled with conductive carbon particles is handled in plane and space using two models.

1st Model: Contact of spherical particles

We proceed from the fact that carbon particles can not only touch within composites (as is the case for metals), but can also mutually intergrow into each other. [1, 3]

D particle diameter
d overlay length

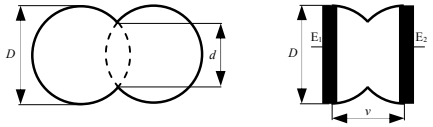

Fig. 1 Contact of two spherical particles

2nd Model: Connecting of two spherical particles by means of conductive bridge [1, 3]

A conductive bridge will formed between particles with diameter D, the bridge width is w, bridge length l.

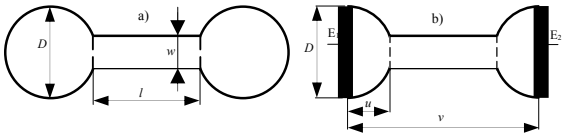

Fig. 2. Connecting of two spherical particles by means of conductive bridge

The area of the bridge in the plane case is the same as the area of the circular particles:

$$l \cdot w = \pi \frac{D^2}{4} \quad \Rightarrow \quad \frac{l}{D} = \frac{\pi}{4}\left(\frac{w}{D}\right)^{-1}$$

By analogy, the volume of the bridge for the space case is the sames as the volume of spherical particles:

$$\pi \frac{w^2}{4} l = \frac{\pi}{6} D^3 \quad \Rightarrow \quad \frac{l}{D} = \frac{2}{3}\left(\frac{w}{D}\right)^{-2}$$

The slenderness of the bridge changes for each individual model.

Analog solution

For realization of planar field analogous model, it is used direct current field in a layer of graphite paper of constant *h* thickness. One-sided graphite paper ($R_{\square} = 1.58 \cdot 10^3\ \Omega$) was used for building of analogous models for our analogous facility. Silver varnish Degussa 200 ($R'_{\square} = 0.4\ \Omega$) proved as the best for building of conductive parts of models edges (electrodes). Results of analog solution were published on DMSRE 2009. [4]

Numerical solution

For solving the above mentioned models, we will use the equation defining the electric current field in a conductive environment

$$\vec{J} = -\frac{1}{\rho}\operatorname{grad} U \quad \text{and} \quad \operatorname{div}\vec{J} = 0,$$

where U is electric potential, J is current density and ρ resistivity.

By introducing a non-dimensional potential, normalized by the difference in electrode potential, i.e. $U^* = \frac{U - U_1}{U_2 - U_1}$,

we are able to derive Laplace's differential equation for the electric field in models

$$\nabla^2 U^* = \frac{\partial^2 U^*}{\partial x^2} + \frac{\partial^2 U^*}{\partial y^2} + \frac{\partial^2 U^*}{\partial z^2} = 0.$$

The dependency on coordinate z is no longer valid for plane cases. The boundary conditions for this equation are mixed: Dirichlet conditions on electrodes, i.e. $U_1^* = 0$ or $U_2^* = 1$ respectively and Neumann conditions on the remaining boundaries, i.e. the zero derivation of potential in the direction of the normal towards the boundary.

The COMSOL Multiphysics program environment was used to resolve the stated boundary conditions for various values of overlapping particles or bridge widths. The current density and current I conducted through electrodes will be evaluated from the obtained electric fields.

The COMSOL program enables the numerical evaluation of this integral directly in the offered "Boundary Integration" procedure. [5]

For comparing the properties of fields in plane and space models, non-dimensional parameters were introduced for the monitored quantities, as the ratio of the given resistance and its reference values.

Fig. 3 and 4 give an example of the solution for electric current fields for plane and space particle contact cases with a ratio v/d = 0.9.

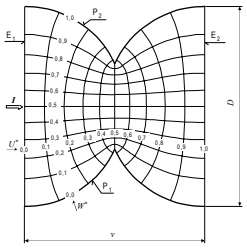

Fig. 3 Electrical field on planar Model 1 v/d = 0.9

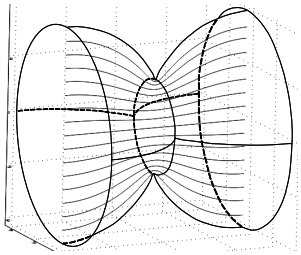

Fig. 4 Electrical field on space Model 1 v/d = 0.9

References

[1] Weber M., Kamal M.R., Estimation of the volume resistivity of electrically conductive composites. Polymer composites, 18 (1997) 711-725.

[2] Thongruang W., Spontak R.J. and Balik C.M., Correlated electrical conductivity and mechanical property analysis of high-density polyethylene filled with graphite and carbon fiber. Polymer 43 (2002) 2279-2286.

[3] Meincke O. et al. Mechanical properties and electrical conductivity of carbon-nanotube filled polyamide-6 and its blends with acrylonitrile/butadiene/styrene. Polymer 45 (2004) 739-748.

[4] Pilarčíková, I., Hampl, J., Jirků, S., Modeling of constriction phenomenon in composite containing conductive carbon particles. in Development of Materials Science in Research and Education. Bratislava: Slovak Expert Group of Solid State Chemistry and Physics, 2009, p. 62-63.

[5] Program COMSOL Multiphysic

PHOTOLUMINESCENCE OF CHROMIUM DOPED $SrTiO_3$ POWDERS

Z. Potůček [(a)], Z. Bryknar [(a)], V. Trepakov [(b)], M. Makarova [(b)]

(a) Czech Technical University in Prague, Faculty of Nuclear Sciences and Physical Engineering, Trojanova 13, CZ-120 00 Praha 2, Czech Republic
(b) Institute of Physics, Academy of Sciences of the Czech Republic, Na Slovance 2, CZ-182 21 Praha 8, Czech Republic

The study of small size and confine geometry effect on properties of ferroelectrics and related materials is presently an important topic in solid-state physics. Research is performed mainly on nanolayers, fine-grained ceramics, and nanoparticles embedded in host material. Study of nanopowders seems very attractive in this context since very small nanoparticles can be obtained and their properties are not influenced by substrate, neighboring ceramic grains or surrounding host material.

Quantum paraelectrics $SrTiO_3$ is the most popular and widely investigated model material from the perspective of highly polarizable ABO_3 oxides with perovskite-like structure and phase transition physics. $SrTiO_3$ possesses an antiferrodistorsive structural phase transition between the cubic O_h^1 and tetragonal D_{4h}^{18} phase at ~ 105 K. Dielectric constant increases at cooling with extrapolated Curie-Weiss temperature T_c ~ 35 K due to the TO_1 phonon mode softening. However, polar ordering is prevented by quantum fluctuations and dielectric constant and TO_1 soft phonon mode saturate at the lowest temperatures. Nevertheless $SrTiO_3$ practically losses stability to polar distortions and due to this inherent instability even low levels of appropriate impurities or perturbations can induce in $SrTiO_3$ ferroelectric phase transitions. These features result in very interesting and unusual optical properties of $SrTiO_3$. Very large temperature shift of the zero-phonon R-line of photoluminescence of octahedral Cr^{3+} impurity centers to lower energies was discovered at cooling in $SrTiO_3$:Cr crystals in contrast to conventional dielectric oxides where the R-line corresponding to $^2E \rightarrow {}^4A_2$ zero-phonon transition of Cr^{3+} ion shifts to higher energies with decreasing temperature [1]. The R-line splitting to the doublet (12594.3 and 12597.2 cm^{-1} at 20 K) observed at the tetragonal D_{4h}^{18} phase originates from the splitting of the ^2E excited state of Cr^{3+} ion in the tetragonal crystal field. Moreover temperature behavior of the shift of the average position of the R-lines was found in the tetragonal phase proportional to the reciprocal dielectric constant $1/\varepsilon'$ of $SrTiO_3$ and to the square ω_0^2 of TO_1 soft phonon mode frequency. Such temperature behavior of the zero-phonon R-lines of photoluminescence octahedral Cr^{3+} centers in $SrTiO_3$ was explained as a manifestation of local configurational instability of the $3d^3$ impurity ions in the degenerate ^2E excited state towards quadratic Jahn-Teller effect on a soft polarization TO mode [2].

This unusual "dielectric-related" temperature behavior of the zero-phonon R-lines of photoluminescence of octahedral Cr^{3+} centers controlled by their interaction with the TO_1 soft phonon mode that depends on the character of phase transition enables use Cr^{3+} ions in the studies of phase transitions in perovskite-type oxides with TO soft phonon modes as was successively proved on the series of chromium doped materials such as $Sr_{1-x}Ca_xTiO_3$ crystals [3] or $SrTiO_3$:Cr sol-gel ceramics with the average grain size of about 24 µm [4]. At present we studied the temperature behavior of the zero-phonon R-line of photoluminescence of Cr^{3+} impurity ions in $SrTiO_3$:Cr(0.1%) nanocrystalline powders with an average size of the particles between 13 and 100 nm in order to examine an effect of particle size on low-

temperature phase of $SrTiO_3$. The powders prepared by the Pechini-type polymeric sol-gel method contained at room temperature only single phase with O_h^1 cubic perovskite structure.

All studied $SrTiO_3$:Cr nanocrystalline powders revealed in the near infrared spectral region photoluminescence characteristic for octahedral coordinated Cr^{3+} ions substituted in Ti^{4+} sites in $SrTiO_3$. The emission spectra consisting of the zero-phonon R-line and vibronic sidebands were very similar as in the case of bulk $SrTiO_3$:Cr crystals as the spectra in Fig. 1 demonstrates. Nevertheless the zero-phonon R-line and vibronic sidebands were slightly shifted to higher energies and substantially inhomogeneously broadened so the splitting of the R-line in the tetragonal phase was hidden too. The R-line half-width observed on the powder with average particle size of 100 nm was about 20 cm^{-1} at 12 K in contrast to about 1 cm^{-1} in the case of bulk $SrTiO_3$:Cr crystals [1]. The R-line broadening increased with a decreasing size of the nanoparticles evidencing increasing inhomogeneity of the particle structure. The observed slight shift of the R-line to higher energies with a decreasing size of the nanoparticles can be connected to changes of lattice parameter that probably occur with a decreasing nanoparticle size due to increasing influence of surface effects on nanoparticle crystal structure. The R-line position continuously shifted to lower energies at cooling. This temperature shift observed on the studied $SrTiO_3$:Cr nanocrystalline powders appeared both in character and magnitude very similar as in the case of bulk $SrTiO_3$:Cr crystals. Such temperature behavior of the R-line position indicates that the nanocrystalline particles maintain properties inherent to quantum paraelectric $SrTiO_3$ crystals even at the particle size of about 10 nm.

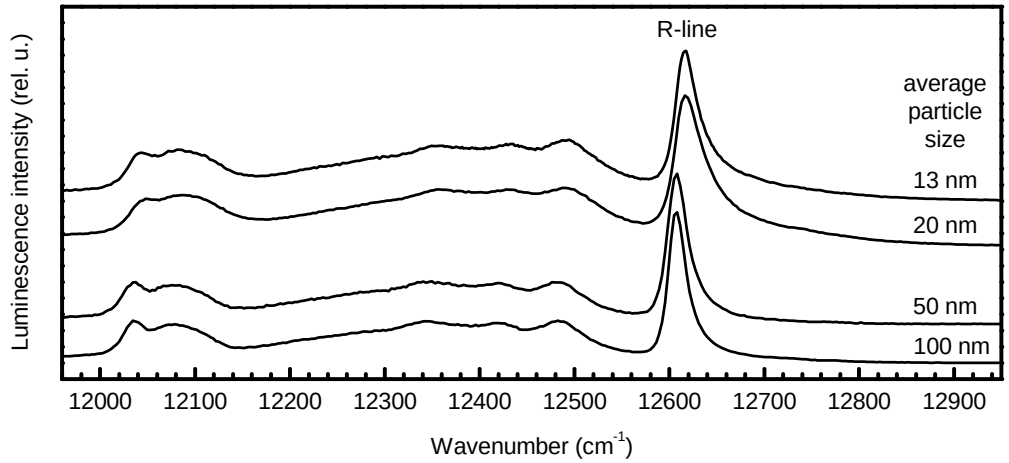

Fig. 1. Normalized photoluminescence emission spectra of the $SrTiO_3$:Cr nanopowders with the average particle size about 13, 20, 50, and 100 nm. Photoluminescence was excited with 465 nm light at 20 K.

This work was supported by the project MSM 6840770021.

[1] S. E. Stokowski, A. L. Schawlow, Phys. Rev. 178 (1969) 464.
[2] V. Vikhnin, V. Trepakov, F. Smutný, L. Jastrabík, Ferroelectrics 176 (1996) 7.
[3] V. A. Trepakov, S. E. Kapphan, J. G. Bednorz, I. Gregora, L. Jastrabik, Ferroelectrics 304 (2004) 86.
[4] V. A. Trepakov, M. E. Savinov, O. Okhay, A. Tkach, P. M. Vilarinho, A. L. Kholkin, I. Gregora, L. Jastrabik, J. Europ. Ceram. Soc. 27 (2007) 3705.

CRYSTALLIZATION KINETICS OF Er:LiY$(PO_3)_4$ GLASS

M. Rodová, A. Cihlář, R. Král, A. Sveshnikov, and K. Nitsch

Institute of Physics AS CR, Cukrovarnická 10, 162 00 Praha 6, Czech Republic

Thermal properties of glasses and features of the crystallization process, its kinetics and mechanisms, are intensively studied with the aim to acquire information about the preparation of both stable glass resistant to crystallization and glassy-ceramics. The crystallization kinetics is experimentally examined in undercooled melt arising when heating glasses above their temperature of glass transformation. Measurements are performed by thermal analysis on glass samples at both constant temperature and constant heating rate. From these measurements the time or temperature dependences of heat flow proportional to the crystallization heat are obtained giving only macroscopic idea about the crystallization process. The running crystallization process is characterized by (i) the function $f(\alpha)$, which expresses the dependence of volume crystallized fraction α on the mechanism of crystallization, temperature and time, (ii) the activation energy for crystallization E_C, (iii) the pre-exponential factor A, and (iv) the Avrami kinetic exponent n. The last one depends on the nucleation procedure, crystal growth mechanism and on the dimensionality (shape) of the crystals grown.

Málek [1], Matusita et al. [2] and [Mahadevan et al. [3] presented the values of the exponent n that are related to different crystallization mechanism and may be 4, 3, 2 and 1. For transformation which initiates nucleation on the surface and one-dimensional growth from the surface to the inside n is equal to 1. For volume nucleation and 1D growth $n = 2$, for 2D growth $n = 3$, while for volume nucleation and 3 D growth $n = 4$.

For the experimental data evaluation the standard nucleation-growth Johnson-Mehl-Avrami (JMA) model is often used. The model was designed for isothermal condition but it can be also used for non-isothermal conditions under meeting specific conditions. In order to obtain values of the Avrami exponent n from measured thermoanalytical data the relation

$$\ln\left[-\ln(1-\alpha)\right] = n\ln k + n\ln(T - T_0) - n\ln\beta \qquad (1)$$

can be used. It was received after taking the JMA model double logarithms and by inserting the temperature increase in time $T = \beta t + T_0$, where β is the heating rate and T_0 is the initial temperature. This makes it possible to evaluate the experimental data, to calculate the Avrami exponent n and to determine the crystallization mechanism of the studied undercooled melt.

Avrami exponent n can be also determined from the function

$$y(\alpha) = \Phi \exp(E_C/RT) \qquad (2)$$

where Φ is the experimentally measured heat flow and E_C is the energy of crystallization. This relation was proposed to determine so-called applicability limits of the JMA model [1,4]. The maximum of this function labeled α_M depends on the value of the exponent n. For $n \geq 1$ it is expressed by $\alpha_M = 1-\exp(n^{-1}-1)$ and the value of the exponent n can be determined.

A method describing non-isothermal crystallization was suggested by Matusita et al. [2] in the form

$$\ln\left[-\ln(1-\alpha)\right] = -n\ln\beta - 1.052\left(\frac{mE_C}{RT}\right) + const. \qquad (3)$$

where n and m are numerical factors. If nuclei formed in the tested glass during heating, Avrami exponent $n = m + 1$. If a large number of nuclei are present in a sample, $n = m$.

This contribution deals with study of the mechanisms of crystallization process in the supercooled melt of phosphate glass with a nominal composition of Er:$LiY(PO_3)_4$. Its aim is to determine the values of the Avrami exponent n by means of the JMA model, function $y(\alpha)$ [4] and the Matusita et al. [3] equation and to discuss the results obtained.

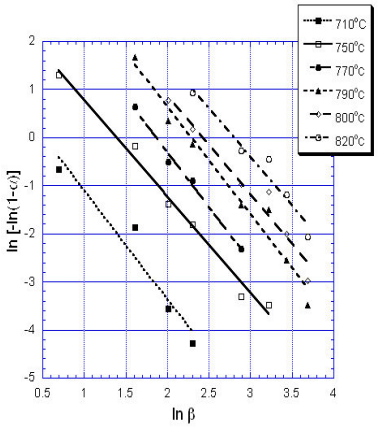

Fig. 1. Dependence of *ln[-ln(1-α)]* on *lnβ* for bulk sample at temperatures between 710 and 820 °C.

The glass with a composition of Er:$LiY(PO_3)_4$ was prepared by a direct synthesis of Li_2CO_3 and YPO_4 with some excess of P_2O_5 and doping $ErPO_4$ at 1200°C [4]. Crystallization kinetics was studied by non-isothermal DSC at heating rates of 2, 5, 8, 10, 18, 25, and 40 K/min from room temperature to 1100°C on the bulk samples in the form of cylinders 3.6 mm in diameter and 1.8 mm in height with both the top and the bottom polished.

The applicability of the JMA model to describe the crystallization kinetics of tested glass by means of $z(\alpha)$ function was verified [5] and eq. (1) can be used for the determination of the exponent n. Fig. 1 shows dependences of *ln[-ln(1-α)]* on *lnβ* for cylinders at temperatures between 710 and 820 °C. The individual dependences can be regarded as parallel straight lines. Computed values of the exponent n for individual temperatures are in the range from 2.0 to 2.26 and they do not seem to be connected with any dependence on temperature.

Using $y(\alpha)$ function and the Matusita et al. equation [2], values of n (m) depending on heating rate were computed. The values of n according to Matusita were 2.7 for heating rates of 2, 5 and 8 K/min and 3.25 for higher ones while n computed by means of the $y(\alpha)$ function reached a value of 2.1 for rates 2 and 5 K/min and a value of 1.4 for higher ones .

This work was supported from the Grant Agency of the AS CR (No. KAN 300100802).

[1] J. Málek, Thermochim. Acta 267 (1995) 61.
[2] K. Matusita, T. Komatsu, R. Yokota, J. Mater. Sci 19 (1984) 291.
[3] S. Mahavedan, A. Giridhar, A.K. Sing, J. Non-Cryst. Solids 88 (1986) 11.
[4] J. Málek, E. Černošková, R. Švejka, J. Šesták, G. Van der Plaats, Thermochim. Acta 280/281 (1996) 353.
[5] K. Nitsch, M. Rodová, R. Král, A. Sveshnikov, Sborník příspěvků z Kalorimetrického Semináře, 33 (2011), Hotel Srní, 23. - 27. 5. 2010, str. 173-176.

STRUCTURE AND PROPERTIES OF LEAD BOROPHOSPHATE GLASSES DOPED BY MOLYBDENUM OXIDE

I. Rösslerová [(a)], L. Koudelka [(a)], Z. Černošek [(a)], P. Mošner [(a)], L. Montagne [(b)], B. Revel [(b)]

(a) Faculty of Chemical Technology, University of Pardubice, 53210 Pardubice Czech Republic
(b) Université Lille Nord de France,UCCS-UMR CNRS 8181, USTL, 59655 Villeneuve d'Ascq, France

Borophosphate glasses belong among important classes of glassy materials because they offer better thermal stability and chemical durability than phosphate glasses. Zinc and lead metaphosphate glasses reveal higher chemical durability than alkali metaphosphate glasses. The reason for the improvements in the properties of borophosphate glasses is ascribed by the transformation of linear-chain structure of metaphosphate glasses into three-dimensional structure of borophosphate glasses due to the additions of B_2O_3. Doping of borophosphate glasses by heavy metal oxides like Nb_2O_5, MoO_3, WO_3 or TeO_2 are interesting due to their semiconducting properties due to the presence of transition metal ions in multivalent states.

In this study we prepared 16 glassy samples from the system $PbO\text{-}P_2O_5\text{-}B_2O_3\text{-}MoO_3$. Eight samples were obtained in the compositional series $(100\text{-}x)[0.5PbO\text{-}0.4P_2O_5\text{-}0.1B_2O_3]\text{-}xMoO_3$ and another eight samples were prepared for glasses with 0, 20, 40 and 60 mol% MoO_3 with the ratio of B_2O_3/P_2O_5 equal to 5/45 and 15/35 to study also the effect of the replacement of P_2O_5 by B_2O_3 in these glasses. Glasses were prepared by conventional melt-quenching method from analytical grade PbO, MoO_3, H_3BO_3 and H_3PO_4 using a total batch weight of 30g. The synthesis was carried out in platinum crucibles by heating up to 1000-1350°C. The obtained melt was poured into a preheated graphite mould and prepared glasses were relaxed for 2 hours at a temperature 5°C below their glass transition temperature, T_g, and then cooled to room temperature.

The obtained glasses revealed a green color due to the presence of Mo^{5+} ions the content of which was determined by electron spin resonance. Glass density increases with increasing MoO_3 content, whereas molar volume only slightly decreases. Chemical durability of glasses was investigated by the measurement of dissolution rate (DR) at room temperature, which increases with increasing MoO_3 content from $2{,}5 \times 10^{-8}$ up to $8{,}64 \times 10^{-6}$ $g.cm^{-2}.min^{-1}$ for the glass with 70 mol% MoO_3.

The values of glass transition temperature T_g was measured independently by DTA and dilatometry. The compositional dependences of T_g in the glasses of the series $(100\text{-}x)[0.5PbO\text{-}0.4P_2O_5\text{-}0.1B_2O_3]\text{-}xMoO_3$ are shown in Fig. 1 together with the values of dilation softening temperature T_d. Both dependences reveal a maximum at 30 mol% MoO_3. On the other side, coefficient of thermal expansion reveals a maximum for the glass with 40 mol% MoO_3 (Fig. 1).
Glass transition temperature in glasses with 0 a 20 mol% MoO_3 increases with B_2O_3 content, whereas in glasses with 40 and 60 mol% MoO_3 it decreases with increasing B_2O_3 content.

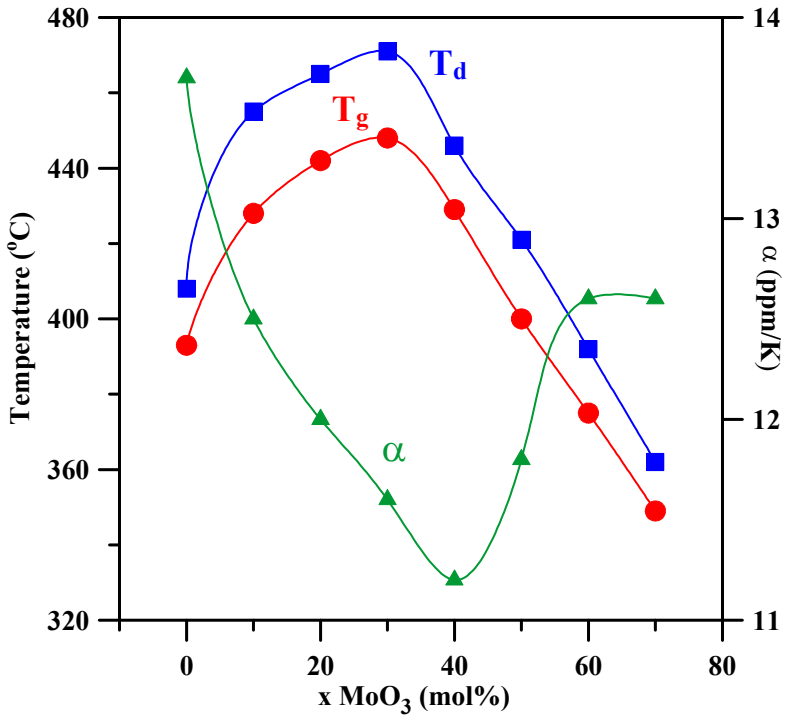

Fig. 1: Compositional dependence of glass transition temperature T_g, dilation softening temperature T_d and coefficient of thermal expansion α.

For structural study the ^{31}P and ^{11}B MAS NMR spectroscopy were applied as well as Raman spectroscopy. ^{31}P MAS NMR spectra showed on the depolymerization of phosphate chains with increasing MoO_3 content due to the formation of Mo-O-P bonds between octahedral MoO_6 structural units and tetrahedral PO_4 units [1]. ^{11}B MAS NMR spectroscopy is able to supply information on the boron coordination in the studied glasses because these spectra possess an ability to discriminate between tetrahedral BO_4 boron coordination and trigonal BO_3 coordination [2] due to the different ranges of chemical shift values for BO_4 and BO_3 units. The measurement of ^{11}B MAS NMR spectra of the studied glasses with the NMR spectrometer with a high resolution (magnetic field 18.8T) revealed the formation of $B(OP)_{4-x}(OMo)_x$ mixed structural units and the decomposition of these spectra brought relative amounts of individual mixed structural units in these glasses. Raman spectra showed on the formation of molybdate clusters composed of MoO_6 octahedra due to the formation of Mo-O-Mo bonds.

The authors are grateful for the financial support from the research project No. 0021627501 of the Ministry of Education of Czech Republic and to the project SG300001.

[1] L. Koudelka, I. Rösslerová, J. Holubová, P. Mošner, L. Montagne, B. Revel, *Structural Study of PbO-MoO_3-P_2O_5 glasses by Raman and NMR spectroscopy,* J. Non-Cryst. Solids 15 (2011) 2816.

[2] L. Koudelka, J. Šubčík, P. Mošner, L. Montagne, L. Delevoye, *Structure and properties Sb_2O_3-containing zinc borophosphate glasses*, J. Non-Cryst. Solids 353 (2007) 1828.

WATER BASED SOL-GEL METHODS USED AT Bi-Sr-Co-O THERMOELECTRICS SYNTHESIS

K. Rubešová [(a)], T. Hlásek [(a)], V. Jakeš [(a)], D. Sedmidubský [(a)], J. Hejtmánek [(b)]

[(a)] Institute of Chemical Technology Prague, Department of Inorganic Chemistry, Technická 5, Prague 6, 166 28, Czech Republic
[(b)] Institute of Physics AS CR, Cukrovarnická 10, Prague 6, 162 00, Czech Republic

One of the serious tasks for sustainable growth is energy generation and its storage. The use of thermoelectric effect is one of the promising technologies – the waste heat recovery or the use of thermoelectrics as a supplement to solar cells (they can convert also low frequency heat energy in comparison to the solar cells). Ceramics based on misfit layered cobalt oxide represent a potential thermoelectric material. In contrast to intermetalic compounds (i.e. Bi_2Te_3), they have lower thermoelectric performance but they are non toxic and stable up to higher temperatures.

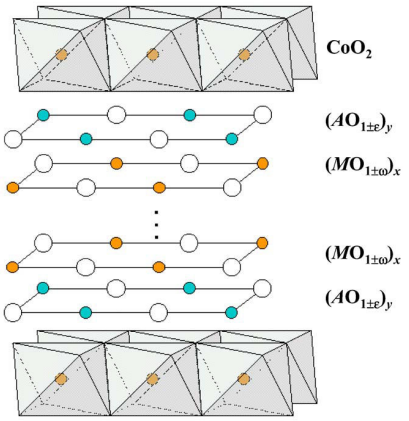

As the first, layered Na_xCoO_2 system with the high valence of cobalt was investigated[1]. Related cobalt oxides (i.e. $Ca_3Co_{3.95}O_x$, $Bi_2Sr_2Co_{1.8}O_x$) with general formula $[M_nA_2O_{n+2}]_x[CoO_2]_y$ have been developed so far. The structure generally contains two misfit subsystems (the picture adopted from[2]). The first one with rock salt structure is composed of square-planar MO layers (M = Co, Bi, Pb, Tl…) surrounded by AO planes also with square symmetry (A = Ca, Sr, Ba…). CoO_2 subsystem has hexagonal symmetry (CdI_2 crystal type) and is built from edge sharing CoO_6 octaedra. Mixed valence Co^{3+}/Co^{4+} is favored for high thermoelectric performance at the misfit cobalt oxides.

Also another Bi-Sr-Co-O material is of great technological interest: $Bi_2Sr_2CoO_x$. This oxide system was established as a possible substituted derivative of the superconducting Bi-2201 cuprate[3]. The phase has orthorhombic layered structure with a stacking distorted perovskite type block (Sr/O-Co/O-Sr/O) and a rock salt type block ($Bi/O_{1+\delta}$). The structure is modulated, but only four fold in comparison to the "parent" Bi-2201 cuprate. Extensive research aiming at spin state of cobalt (and resulting magnetism) has been realized, however, the phase is still out of interest concerning its potential thermoelectric properties.

High figure of merit ZT ($\sim S^2T/\rho\kappa$) is necessary to reach high thermoelectric performance. Therefore the thermoelectric material should meet some microstructure criteria, mainly bulk density. Methods where bulk material is prepared from a melt (i.e. flux flow sintering, spark plasma sintering) or solid state reaction with enhanced grain growth (i.e. hot pressing) are utilized. Sol-gel methods can be successfully used for preparation of oxide precursor powders that possess high chemical homogeneity and small grain size.

In this work, the both above mentioned Bi-Sr-Co-O systems ($Bi_2Sr_2Co_{1.8}O_x$ and $Bi_2Sr_2CoO_x$) were prepared using a sol-gel process. The choice of an appropriate water based method is difficult due to a presence of Bi^{3+} cation as a strong hydrolyzing species. According to our previous experience with Bi-based superconducting cuprates[4], we applied two different

sol-gel processes: an improved chelate method using the combination of ethylenediamintetraacetic acid (EDTA) and triethanolamine (TEA) and, secondly, a water soluble polymer method applying polyethylenimin (PEI) as N-donor chelating agent suitable for the bismuth cation. The process is described bellow:

a) bismuth acetate, EDTA and water were mixed up; ammonia was added to the suspension up to full dissolution of EDTA and a Bi precipitate. Sr/Co-EDTA solution was prepared using the same way. The solutions were mixed, TEA was added and the mixture was stirred at 80 °C to evaporate water (pH was controlled to prevent any precipitation). Then temperature was increased up to 100 °C to reach gelation; at the same time temperature started to increase spontaneously. Thus prepared gel was decomposed at 250 °C for 2h.

b) the process using PEI was nearly the same, only there is not the particular need of pH adjustment and also the temperature was stable during the gelation. We used 50% water solution of PEI with molecular weight 2000 g/mol.

The precursors coming from both methods were heat treated either at ambient atmosphere or step by step at pure N_2 and O_2. The final sintering procedure depended on the prepared phases. The heat treatment is summarized in the following table:

$Bi_2Sr_2Co_{1.8}O_x$				$Bi_2Sr_2CoO_x$			
EDTA/TEA method		*PEI polymer method*		*EDTA/TEA method*		*PEI polymer method*	
250°C / 2h / air		250°C / 2h / air		250°C / 2h / air		250°C / 2h / air	
500°C/2h/air	800°C/3h/N_2	500°C/2h/air	800°C/3h/N_2	500°C/2h/air	800°C/3h/N_2	500°C/2h/air	800°C/3h/N_2
800°C/2h/air	400°C/1h/O_2	800°C/2h/air	400°C/1h/O_2	800°C/2h/air	400°C/1h/O_2	800°C/2h/air	400°C/1h/O_2
sintering at 870°C, 96 h				sintering at 880°C, 48 h			

The chosen sol-gel methods and different gel decomposition regimes were compared. The influence of heat treatment at different atmosphere on grain size of a precursor powder was evaluated using SEM. Effect of the mentioned parameters was also monitored on the final samples. SEM equipped with image analysis was used for microstructure comparison. Thermoelectric transport characteristics (temperature dependence of Seebeck coefficient, resistivity and thermal conductivity) were measured. The phase composition of the prepared samples was established by XRD analysis (using Co K_α radiation). The samples were also characterized by the PPMS and DSC measurement of heat capacity at low and elevated temperatures.

This works was financially supported by the Czech Science Foundation, the Project No. 203/09/1036.

1 Terasaki, I., Sasago, Y. & Uchinokura, K. Large thermoelectric power in $NaCo_2O_4$ single crystals. *Phys. Rev. B* **56** (1997) 12685-12687.

2 Morita, Y. *et al.* Oxygen nonstoichiometry and cobalt valence in misfit-layered cobalt oxides. *J. Solid State Chem.* **177** (2004) 3149-3155, doi:10.1016/j.jssc.2004.05.023.

3 Tarascon, J. M. *et al.* Structure and magnetic properties of nonsuperconducting doped Co and Fe $Bi_2Sr_2Cu_{1-X}M_XO_Y$ phases. *Phys. Rev. B* **39** (1989) 11587-11598.

4 Rubešová, K., Jakeš, V., Hlásek, T., Vašek, P., Matějka, P. Gel stabilization in chelate sol-gel preparation of Bi-2223 superconductors. *submited to the Journal of Chemistry and Physics of Solids* (2011).

LASER WELDING OF DISSIMILAR STEELS

M. Sahul, M. Behúlová and M. Turňa

Slovak University of Technology in Bratislava, Faculty of Materials Science and Technology in Trnava, Paulínska 16, 917 24 Trnava, Slovak Republic

Welds with combinations of austenitic stainless steel and ferritic steel are utilised especially in petroleum and petrochemical industries. Problems arising during welding of austenitic stainless steel to carbon steel are related to their different physical, chemical and mechanical properties. Welding of dissimilar metals represents currently the object of extensive research [1-3]. The aim of this contribution is the analysis of laser welding of austenitic stainless steel to low carbon steel and evaluation of the quality of weld joints.

Experimental

Experimental samples were prepared in cooperation with the First Welding Company in Bratislava. Austenitic non-stabilised stainless steel (AISI 304) and DC 01 low carbon steel were selected as the base materials for this study. The thickness of the metal plates to be welded was 2 mm. Both austenitic stainless steel and low carbon steel were supplied in the cold rolled state. Butt welded joints were produced without the use of filler metal using the TruDisk 8002 laser with the maximum output power of 8 kW and the wavelength of 1.030 μm applying different welding parameters. The maximum power used in experiment was 2 kW. The laser beam was focused on the surface of welded metals (spot size - 400 μm). The focal distance reached the value of 200 mm. Argon was used as a shielding gas.

Optical microscopy, microhardness measurement and EDX microanalysis were used for evaluation of the quality of weld joints.

Results

Macrostructures of selected butt welded joints prepared with different welding parameters (laser power and welding speed) are illustrated in Fig. 1. The structure of AISI 304 stainless steel consists of austenitic grains. Increased proportion of δ-ferrite was observed in HAZ of austenitic stainless steel (Fig. 2a). The structure of low carbon DC 01 steel is comprised of polyhedral ferrite. The texture after steel cold rolling steel was found. Based on the analysis of macrostructures of weld joints, it was found that HAZ of DC 01 steel was wider. This fact is related to the higher thermal conductivity of low carbon steel.

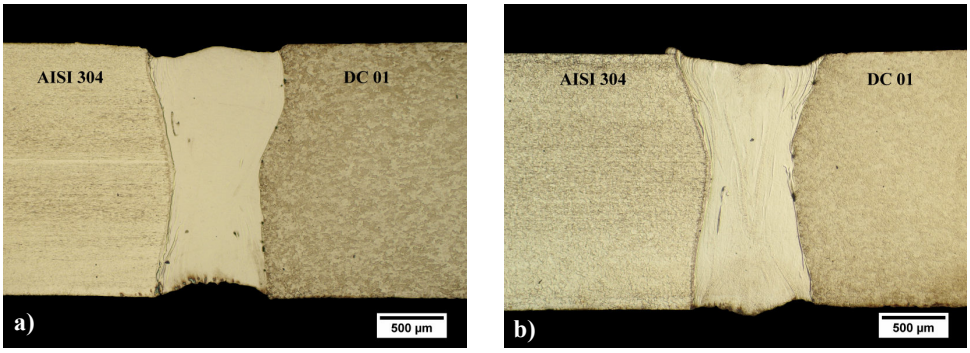

Fig. 1. Macrostructures of joints: a) P = 2 kW, v = 30 mm/s, b) P = 1.5 kW, v = 35 mm/s

In the next stage of evaluation of the quality of welded joints, Vickers microhardness measurements across welded joints were performed. Distance between indents was 100 μm. The load of 100 g was applied for 10 s. Hardness of AISI 304 steel was approximately 200 HV, while the micro-hardness of the structural carbon steel ranged in the interval from 100 to 150 HV. For example, the microhardness profile through selected weld joint is given in Fig. 2b.

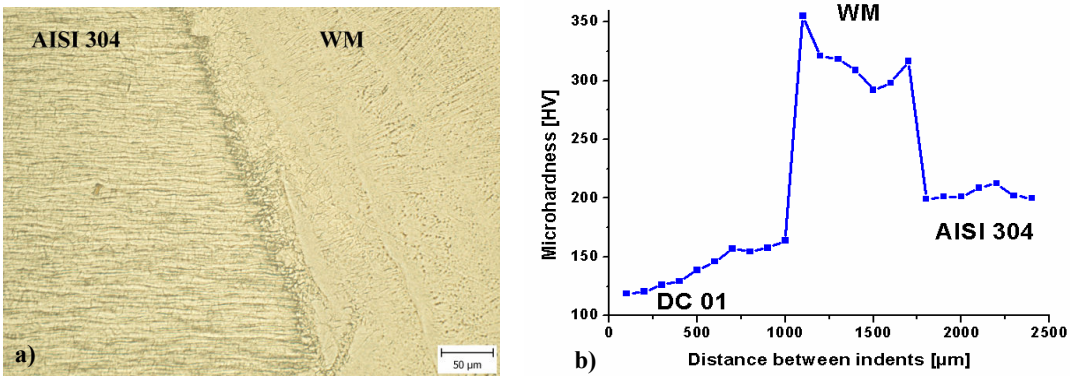

Fig. 2. a) AISI 304 - weld metal interface, b) course of microhardness across DC 01 - AISI 304 weld joint (P = 1.5 kW, v = 35 mm/s)

The aim of EDX microanalysis was to analyse the change of element concentration through produced welds. The increase in the concentration of Cr from DC 01 steel through weld metal (WM) up to AISI 304 steel was observed. Similar course was recognised according to Mn and Ni. On other hand, the concentration of Fe decreased from DC 01 steel towards AISI 304 steel. The presence of microinhomogeneities was not recorded.

Conclusion

In this study, the weld joints of dissimilar steels were examined. Using macrostructures of joints of dissimilar steels, it was documented that the increase in laser power resulted in the increase of the weld metal width and also DC 01 steel HAZ width. The maximum hardness of 355.2 HV was measured in WM of butt joint prepared with laser power of 1.5 kW and welding speed of 35 mm/s. In the case of DC 01 - AISI 304 butt welded joint, increase in the concentration of Cr, Ni and Mn from DC 01 steel through WM up to AISI 304 steel was observed.

Acknowledgement

The contribution was prepared under the support of GA VEGA MŠ SR and SAV within the projects No. 1/0842/09 and 1/1041/11. Material evaluation was realized in the framework of the project ITMS 26220120048 „Centre for Development and Application of Advanced Diagnostic Methods in the Processing of Metallic and Nonmetallic Materials“.

References

[1] Ready, J. F.: *LIA Handbook of Laser Materials Processing*. USA: LIA, 2001.
[2] Paschotta, R.: *Encyclopedia of Laser Physics and Technology*. Wiley-WCH, Weinheim, 2008.
[3] Shin, H. J., Yoo, Y. T., Shin, B. H., Kim, J. H.: *Dissimilar Metal Welding of Austenite Stainless Steel and Carbon Steel Using Nd:YAG Laser a Continuous Wave*. In Key Engineering Materials Vol. 345-346 (2007), pp. 1445-1448.

DIELECTRIC PROPERTIES OF BARIUM TITANATE PREPARED BY SPARK PLASMA SINTERING

P. Ctibor [(a)], J. Sedláček [(b)], M. Dopita[(c)], Z. Pala[(a)]

(a) Institute of Plasma Physics, Academy of Sciences of the Czech Republic, Prague, Czech Republic
(b) Faculty of Electrical Engineering, Czech Technical University in Prague, Prague, Czech Republic
(c) Bergakademie Freiberg, Germany

Introduction

Enhanced piezoelectricity in lead-free ceramics is of much interest for human health and environmental protection. In recent years, the development of lead-free piezoelectric ceramics with excellent properties has been extensively investigated in order to find an alternative for toxic lead zirconate titanate (PZT). Among the candidates, barium titanate ($BaTiO_3$, BT), which is a famous dielectric material for capacitors application nowadays, was actually lead-free and the first material practically used to fabricate piezoelectric ceramics before the discovery of high-performance PZT. Meanwhile, although $BaTiO_3$ ceramics had been reported to have a moderate piezoelectric performance for several decades, recent studies revealed that high-performance $BaTiO_3$ ceramics can be obtained [1].

The spark-plasma-sintering (SPS) system was developed in 1990-ies. It is a process which makes use of microscopic electrical discharge between particles under pressure, So it is a combination of the hot-press and the plasma generator [2].The conventional procedures as a classical liquid phase sintering however reached their limits in the preparation of the fine-grained materials, especially because of relatively long sintering times in combination with high temperatures which are necessary for the sintering of compact fully dense materials. The problems of long sintering times are significantly reduced using a modern sintering method – SPS [3]. The sintered material is surrounded by graphite elements for application of heating and for obtaining the desirable form. Therefore just rather simple shapes as tablets, cylinders and small centro-symmetrical bodies could be manufactured by SPS.

$BaTiO_3$ with different grain size ranging from 80 nm to several micrometers were prepared by controlling proper sintering conditions [2]. Investigations upon the grain size dependence of dielectric properties shows that the relative permittivity at room temperature decreased with decreasing grain size - from 4000 for 1 μm grain size to about 1500 for 100 nm grain size.

Experimental

Sintering temperature 1300 °C, pressure 80 MPa, sintering time 20 min and controlled cooling with the cooling rate 100°C/min were applied. The pressure in the sintering chamber was reduced (i.e. no protective gas used).

X-ray diffraction (XRD) was performed on SIEMENS D500™ theta-2theta Bragg-Brentano diffractometer in order to gain information about the phases present within the feedstock powder and coatings.

The microhardness was measured by a Hanemann microhardness head (Zeiss, Germany) mounted on an optical microscope with a fixed load of 1 N and a Vickers indenter. Twenty indentations from various areas of a polished surface for each sample were analyzed.

Electric measurements were performed on rectangular samples 2x5x12 mm cut from the as-sintered cylindrical sample, because it contained several cracks. The surface of

specimens was ground to eliminate surface roughness. Layers of Al as thin film electrodes were sputtered in a reduced pressure on both sides of each sample. The electric field was applied perpendicularly to the sintering pressure direction as well as parallel with it, see Fig. 1. Capacity and loss factor were measured in the frequency range from 9 kHz to 1 MHz using a precision LCR meter Agilent 4284A. Relative permittivity ε_r was calculated from measured capacities C_P and specimen dimensions.

Results

The X-ray diffraction pattern exhibit only tetragonal $BaTiO_3$ and is identical before (powder) and after the sintering. The sintered sample exhibited microhardness 4.83 ± 0.70 GPa. Main results of the dielectric measurements are presented in Fig. 1.

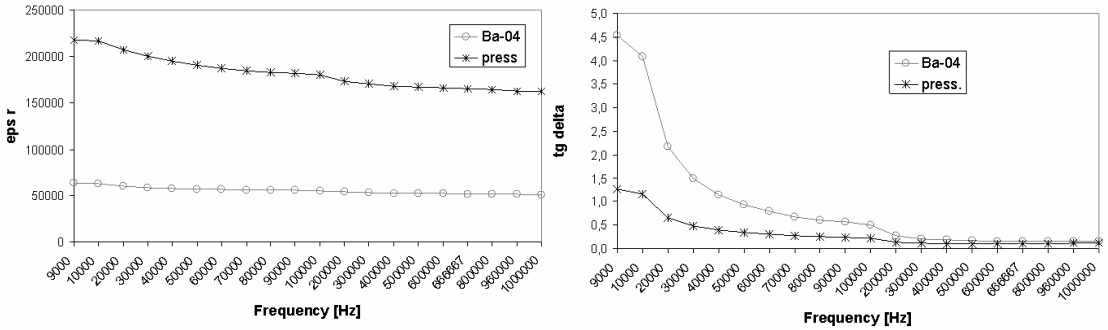

Fig. 1 – Frequency dependence of relative permittivity (left) and loss tangent measured parallel with the sintering pressure (labeled "press") and perpendicularly to the sintering pressure.

The relative permittivity is higher and in the same interval also the loss tangent is lower for the sample measured in the sintering pressure direction. This is probably associated with certain anisotropy of the porosity that should mean more flat pores in the pressure direction and therefore denser structure with easier polarization. Microstructural investigation was however not performed. The "colossal permittivity" values (over 200 000) were detected similarly to certain existing literature [4].

References

[1] Z.-Y. Shen, J.-F. Li: Enhancement of piezoelectric constant d_{33} in $BaTiO_3$ ceramics due to nano-domain structure, Journal of the Ceramic Society of Japan 118 [10] (2010) pp. 940-943.

[2] B. Li, X. Wang, L. Li, H. Zhou, X. Liu, X. Han, Y. Zhang, X. Qi, X. Deng: Dielectric properties of fine-grained $BaTiO_3$ prepared by spark-plasma-sintering, Materials Chemistry and Physics 83 (2004) 23–28.

[3] M. Dopita, C.R. Sriram, D. Chmelik, A. Salomon, H. J. Seifert: Spark plasma sintering of nanocrystalline binderless WC hard metals, Proceedings of the conference Nanocon 2010, Olomouc, Czech Republic.

[4] Z. Valdez-Nava, S. Guillemet-Fritsch, Ch. Tenailleau, T. Lebey, B. Durand, J.Y. Chane-Ching: Colossal dielectric permittivity of $BaTiO_3$-based nanocrystalline ceramics sintered by spark plasma sintering, Journal of Electroceramics, vol. 22 (n° 1 - 3) 2009, pp. 238-244.

KINETICS OF NUCLEATION ON HIGHLY CURVED SURFACES

A. Sveshnikov [a, b], P. Demo [a, b], Z. Kožíšek [a]

(a) Institute of Physics, Academy of Sciences of the Czech Republic, Cukrovarnická 10, 162 00 Prague 6, Czech Republic
(b) Czech Technical University in Prague, Faculty of Civil Engineering, Thakurova 7, 165 29 Prague 6, Czech Republic

Recent successes in the field of nanotechnology open a possibility of creation of new types of materials with exciting properties. One kind of these materials – protective layers – is based on nanotextiles. Nanotextiles are woven of nanofibers, whose diameter ranges between dozens and hundreds of nanometers, while their length is of a macroscopic size. Nanofibers themselves have a number of interesting properties, distinguishing them from ordinary bulk materials. First of all, the ratio of the surface area of a nanofiber to its volume is extremely large. This ensures a high interaction of a nanofiber with its surrounding. Then, the mode of this interaction differs from that one of the macroscopic material. For example, the characteristic radius of Van der Waals force is comparable with the radius of the nanofiber, so that nanotextile behaves quite differently from just scaled-down net of threads. Nanofibers are practically defect-free, which leads to very high strength of the material, close to the theoretical limit. Finally, the radius of curvature of the surface of a nanofiber is very small. Since the Laplace pressure is reverse proportional to the radius of curvature, the Laplace pressure on the surface of nanofiber may achieve values, which are otherwise very hard to achieve. Such high pressure can shift the state of the substance on its phase diagram to such regions, where the formation of interesting phases might become possible.

Up to last years the applications of nanotextiles were mainly the passive ones. These applications profit from the inherent properties of nanofibers and are limited mainly to different kinds of molecular filters. Still more attention is being attracted, however, by the possibility to use nanotextiles as a basis for other materials. In this way the materials with predefined desired properties can be created. An example of this type of nanotextile application is provided by a protective layer for historical buildings. The preservation of historical buildings is an important and quite complicated task. The walls of the building are subject to an aggressive influence of the atmosphere, rains, moulds, temperature differences. It is not possible to use just any substance to protect the walls from these influences, it is necessary to maintain the authentic look and feel of the material. Thus, the protective layer must be extremely thin, practically non-visible, have a good adhesion to the underlying surface and simultaneously provide a high degree of protection. It seems that protective layers based on nanotextiles can satisfy these requirements.

Nanotextiles can be converted into protective layers by nucleation of a secondary substance on its surface. Nanodiamond looks like a very prospective substance for this purpose. Nanodiamond is produced from methane at a relatively low cost. The high Laplace pressure on the surface of nanofiber makes the formation of a diamond phase preferable even under low pressure in the chamber. Nanodiamond has bactericide properties, which is quite desired, because mould growth is one of the main reasons for degradation of buildings. Also, by activation in the corresponding atmosphere, nanodiamond can be made hydrophilic or hydrophobic. Hydrophilic side of the nanotextile will have a strong adhesion to the wall, while its outer hydrophobic side will protect the building from moist.

However, a lot of research still has to be done in order to make this kind of application of nanotextile real. Among the other questions which need to be answered is the formulation

of theoretical model of nucleation on a highly curved surface of a nanofiber. Standard theory of heterogeneous nucleation assumes that the supporting surface is flat or spherical in shape [1, 2]. For surface of macroscopic curvature this assumption is working well. Unfortunately, this is not the case for the nucleation on a surface of the nanofiber. It can be readily proven, that the shape of the growing cluster in this case deviates from the spherical one, but it is much more difficult to calculate the exact shape. The knowledge of the exact shape of the growing cluster is necessary for correct calculation of the Gibbs energy of cluster formation and, consequently, for the evaluation of other important parameters of the phase transition, like the critical size of the cluster or the stationary nucleation rate. The kinetics of the phase transition strongly depends on this shape, since it directly determines the ratio of the surface area to the volume of the cluster.

In our work we make an attempt to estimate the deviation of the shape of the cluster, growing on the surface of the nanofiber, from the sphere. The equilibrium shape is determined from the variational principle of minimum of free energy. The resulting shape appears to be a function of two parameters – the contact angle and the size of the cluster. The deviation of the shape from the sphere is larger for the case of well-wetting and is growing with the increasing cluster size. The time dependence of the shape of the cluster is modeled in the way similar to kinetic Wulff shape of crystals [3].

This work was supported by the Grant No. IAA100100806 of the Grant Agency of the Academy of Sciences of the Czech Republic and the Grant No. SGS10/125/OHK1/2T/1. Scientific activities in the Institute of Physics AS CR are supported by the Institutional Research Plan No. AV0Z10100521.

[1] D. Kashchiev, *Nucleation: Basic Theory with Applications*, Butterworth-Heinemann, 2000.
[2] H. Vehkamaki, *Classical Nucleation Theory in Multicomponent Systems*, Springer, ISBN 3540292136, 2006.
[3] *Crystal Growth – From Fundamentals to Technology,* Edited by G. Muller, J.-J. Metois, P. Rudolph, Elsevier, ISBN 044451368, 2004.

MACROSCOPIC SIGNS OF CRYSTAL STRUCTURE

L. Válek

ON Semiconductor, 1. máje 2230, 756 61 Rožnov pod Radhoštěm, Czech Republic

Single-crystals of silicon for electronic industry are usually grown by the Czochralski (CZ) method [1]. The single-crystalline nature of the silicon ingot in conjunction with the growth process conditions result in a variety of interesting features and effects, which are discussed in this work.

The equilibrium shape of silicon crystal determined by the Wulff construction is bound by {111}, {100} {311} and {110} planes, with {111} planes showing the lowest surface energy. Indeed, formation of {111} facets is observed also during the CZ growth of silicon crystal. Fig. 1 shows the growth habit for common, i.e. (001) and (111) oriented crystals.

The continuous growth lines (or facets) on the crystal surface are the sign of a dislocation-free crystal growth. The surface of a (001) oriented crystal typically has four growth lines holding a four-fold symmetry around the crystal axis, which transform into flat and atomically smooth facets during the crown and shoulder growth. These will be called crystal facets hereafter. Comparing appearance of the crystal facets on the crown and shoulder with orientation of the crystal planes, it shows that the crystal facets coincide with a set of {111} planes highlighted by gray color in Fig. 1, i.e. (111), (1-11), (-1-11) and (-111).

The (111) oriented crystal typically has six growth lines during the crown growth, holding a six-fold symmetry around the crystal axis. Three of them, 120° apart, disappear during the shoulder growth; the other three (rotated by 60° with respect to the first triplet) continue to the body growth stage where they widen and transform into growth facets. During the slight diameter decrease (typically occurring in the beginning of the body), crystal facets are formed on the growth facet. Similarly, crystal facets are formed during diameter decrease in the tail growth stage. Comparing appearance of the crystal facets on the body and tail with the orientation of the crystal planes, it shows that the crystal facets coincide with a set of {111} planes highlighted by grey color in Fig. 1, i.e. (-1-11), (1-1-1), and (-11-1). Hence, it suggests itself that the crystal growth lines/facets in general result from formation of {111} facets on the surface of the crystal.

Let´s have a look on the melt-crystal interface. The (111) oriented crystals are characteristic by formation of an atomically flat facet in the center of the interface. As the central facet coincides with the (111) or (-1-1-1) plane, it is also a crystal facet similar to those found on the outer crystal surface. This crystal facet obviously appears when the melt-crystal interface becomes tangential to the (111) plane. But can the interface be tangential to the {111} sets resulting in formation of the growth lines/facets? The formation mechanism of the growth lines/facets will be discussed in the presentation in terms of 2D growth of singular surfaces, orientation-dependent growth rate and conditions on the tri-junction point.

This work is partially supported by grant FR-TI3/031 awarded by Ministry of Industry and Trade of the Czech Republic.

[1] M. Lorenc, J. Šik, L. Válek, proceedings of The 3rd School on Crystal Growth 2004, editor K. Nitsch, M. Rodová, MAXDORF Praha (2004) 48-57.

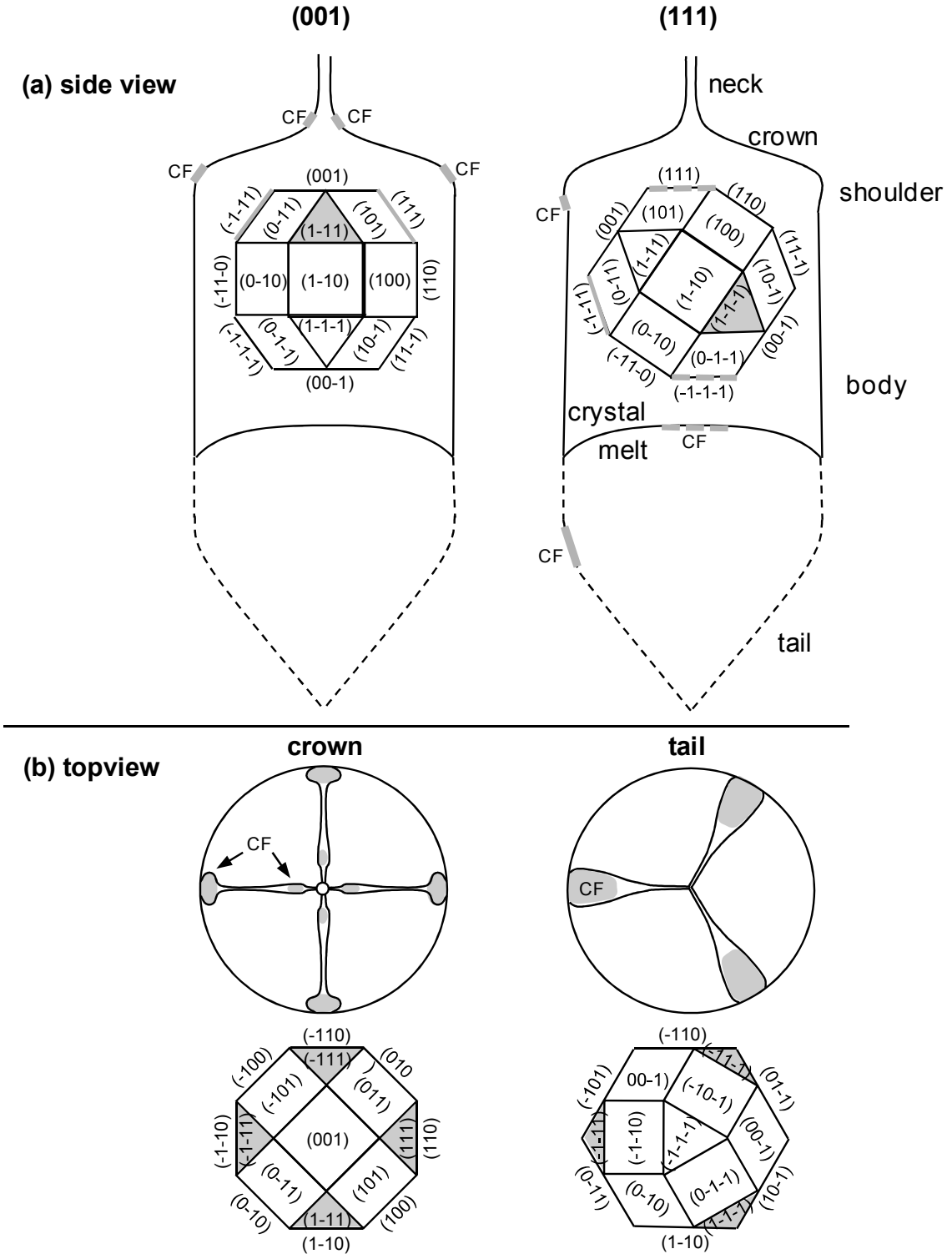

Fig. 1. Growth habit of (001) and (111) oriented CZ silicon single crystals. Crystal facets (CF) and corresponding crystal planes are drawn in grey. (a) Side view on the growing crystal from [1-10] direction. The dashed line represents the crystal to be yet grown. (b) Top view on the (001) crystal crown and (111) crystal tail with arrangement of corresponding crystal planes.

GRAPHITE BASED SCHOTTKY DIODES

R. Yatskiv [(a)], J. Grym [(a)]

(a) Institute of Photonics and Electronics, Academy of Sciences of the Czech Republic, Chaberska 57, 18251 Prague 8, Czech Republic

Schottky barriers (SB) formed at metal-semiconductor interfaces are critical components of many optoelectronics devices. Metal-semiconductor interfaces created by various conventional metal deposition techniques are known to exhibit low Schottky barrier heights due to Fermi level pinning effect caused by extrinsic damages at metal/semiconductor interfaces [1]. Recently, it has been demonstrated that highly oriented pyrolytic graphite (HOPG) forms high-quality SBs on various n-doped semiconductors such as Si, GaAs and SiC [2]. The forward-bias characteristics of these SBs at RT were described by thermionic emission. The HOPS contact can be applied at room temperature and causes minimal damage at metal/semiconductor interfaces.

In this work we use colloid graphite to create high quality Schottky diodes on the n-type InP, with the concentration of free electrons of $5x10^{15}$ cm^{-3}. Colloid graphite was deposited by painting. The graphite contact does not form a solid layer but it consists of irregular particles of sizes in the range of about one micrometer, with openings (pores) among them [3]. Ohmic contact on the back side was formed by rubbing liquid gallium with a tin rod. The diodes were characterized by measuring the current-voltage characteristics (I-V) at different temperatures in the range from 100 K to 425 K (Figure 1).

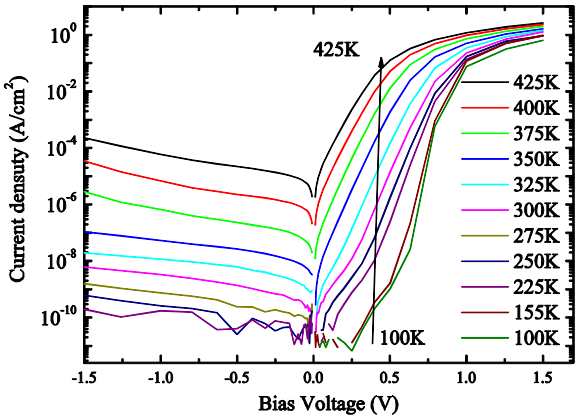

Figure 1. Current-voltage characteristics of graphite/InP measured at different temperature.

As seen from Figure 1 graphite based Schottky diodes exhibit very good rectifying ratio (about 10^8 at 1.5 V) at room temperature. The linearity of I-V characteristics in semi-logarithmic plots at forward bias corresponds to the thermionic emission model (TEM). According to TEM the forward I-V relationship of a Schottky diode at V>3kT/q can be expressed as

$$I_s = I_o \exp(qV/kT)$$

where

$$I_o = A^{**}T^2 \exp(q_B/kT)$$

where A^{**} is Richardson's constant, T is absolute temperature, k-Boltzmann constant, ϕ_B is Schottky barrier height (SBH) and η ideality factor. The saturation current density (I_0) and

ideality factor (η) can be determined from extrapolation and slope of $\ln(I_F)$ versus V plot, respectively. Table 1 shows the basic electrical parameters calculated from I-V-T characteristics for graphite/InP Schottky diodes.

Table 1 Electrical parameters calculated from I-V-T characteristics for graphite/InP Schottky diodes

Temperature T(K)	105	155	225	255	275	300	325	350	375	400	425
Rectification ration at 1.5V	-	-	5.6E9	1.5E9	5.3E8	2.1E8	6.9E7	1.4E7	6.2E5	5.8E5	1.04E4
Ideality factor (η)	2.24	1.55	1.48	1.37	1.39	1.36	1.32	1.17	1.16	1.18	1.23
SBH (ϕ_B)	0.40	0.60	0.83	0.92	0.96	1.01	1.07	1.07	1.07	1.06	1.05

The result of the C-V measurements at room temperature is shown in Figure 2. A doping concentration of $6x10^{15}$ cm^{-3} and a Schottky barrier height of 1.05eV were obtained from $1/C^2$-V relationship. The SBH calculated by C-V method is in good agreement with that by I-V method. A doping concentration calculated from CV characteristics is in the good conformity with the value obtained by the Van der Pauw Hall measurements.

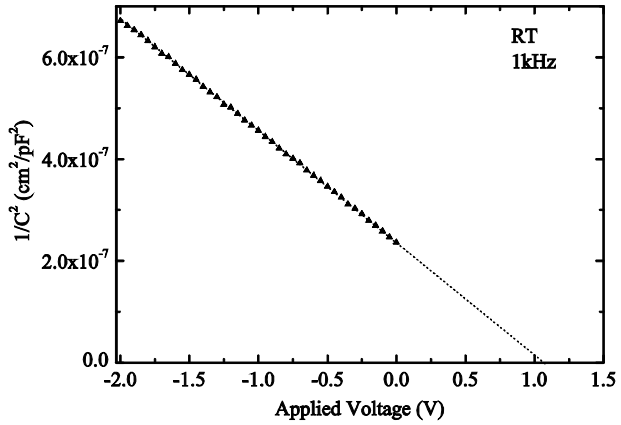

Figure 2. A plot of $1/C^2$ as a function of the applied voltage for graphite/InP measured at RT.

We have demonstrated the formation of Schottky contact by painting colloid graphite on InP substrates. The extracted values of the barrier height (ϕ_B) and ideality factor (η) from I-V (C-V) characteristics were 1.01 (1.05) eV and 1.36 at RT, respectively. The linearity of I-V characteristics in semi-logarithmic plots at forward bias corresponds to the thermionic emission model. The high values of the barrier height can be explained by the improved metal/InP interface as a result of the lower Fermi level pinning effect.

This work has been supported by the project KJB200670901 of the ASCR.

[1] H. Hasegawa, Jpn. J. Appl. Phys. 38 (1999) 1098.

[2] S. Tongay, T.Schumann and A.F. Hebard, Appl. Phys. Let. 95 (2009) 222103.

[3] K. Zdansky, R. Yatskiv, J. Grym, O. Cernohorsky, J. Zavadil, F. Kostka, in: Proceedings 2nd NANOCON International Conference, 182 (2010).

DEVELOPMENT TRENDS OF SMALL MOLECULE X-RAY DIFFRACTION SYSTEMS

J. Maršík [a]

(a) Rigaku Innovative Technologies Europe s.r.o., 142 21 Prague, Czech Republic

X-ray diffractometers dedicated to diffraction investigation of monocrystallic materials (SMX) build from a technical point of view very specific group of X-ray instruments. While conventional X-ray diffractometers dedicated to measurements of powder samples have been qualitatively changing very slowly over last decade, SMX instruments are developing much more dramatically. The reasons are coming both from customer's requirements and technological progress.

Every SMX instrument consists of following key components: X-ray source, X-ray optics, goniometer and 2D X-ray detector. Each such component can be chosen from wide variety of qualitatively and quantitatively different options which results in huge number of instrument configuration options.

Company Rigaku has been since its inception in 1951 in forefront of development of both X-ray sources, X-ray optics and X-ray detectors. All these three areas are under focus of Rigaku R&D department and new innovations and improvements are being announced every year. This contribution would like to identify to the instrument user main trends and directions in which are future SMX instruments moving.

XtaLAB mini

NEW

Benchtop X-ray crystallography system

Fully functioning benchtop X-ray crystallography system

- Robust, simple design
- Intuitive software, ideal to support non-expert users
- Exceptional data quality – ready to publish structures to or exceeding IUCr publication standards

ITES Vranov, s. r. o.
Čemernianska 137
093 03 Vranov nad Topľou, Slovenská republika

… nábytok a digestory pre laboratórium

V spoločnosti ITES Vranov s.r.o. nás zaujímajú predstavy našich zákazníkov. Na Vaše želanie pre Vás vytvoríme laboratórium presne na mieru.

Odlíšte sa od iných laboratórií nielen profesionálnym prevedením laboratórneho nábytku, ale aj napríklad jeho dizajnom a úrovňou bezpečnosti obsluhy. S použitím materiálov špičkovej kvality zároveň zvyšujeme úžitkovú hodnotu nábytku.

ITES .... partner vo Vašom laboratóriu

KONTAKT
tel: +421-57-4461961, 4431139
fax: +421-57-4422097
e-mail: ites@ites.sk
http://www.ites.sk

ANAMET Slovakia s.r.o., 1.Mája 794/29, 900 01 Modra
Tel: +421 905 249 664; igor.culak@anamet.sk
www.anamet.cz

DODÁVA MERACIU A TESTOVACIU TECHNIKU PRE LABORATÓRIA A SKÚŠOBNE

NETZSCH

Termická analýza TG, DTA, DSC, STA, TMA, DMA, DIL
Kombinované techniky (TA-MS, TA-FTIR)
Testovanie lomu materiálov (RUL, CIC, MOR)

MALVERN

Distribúcia veľkosti a tvaru častíc
Zeta potenciál, molekulová hmotnosť
Morfológia, rotačné viskozimetre, rheometre

Quantachrome INSTRUMENTS

Meranie spec. povrchu a porozity
Hg porozimetria
He pyknometria
sorpcia vodnej pary

Angelantoni

Klimatické, termostatické, šokové, vákuové, korózne a vibračné komory
ESS a HALT/HASS testy

FTT FIRE TESTING TECHNOLOGY

Požiarna odolnosť materiálov
Kalorimetre
Spaľovacie komory

RNDr . Igor Čulák, CSc.

PRELIMINARY PROGRAM DMS-RE
Kežmarské Žľaby 2011

Monday, August 29, 2011

REGISTRATION…….. 10:00 – 13:30
LUNCH……... 13:00
OPENING……... 14:00 – 14:10

LECTURES

CHAIRMAN	**B. Papánková**
14:10 – 14:40	*K. Nitsch* **STUDY ON CRYSTALLIZATION KINETICS OF UNDERCOOLED MELTS**
14:40 – 15:00	*M. Rodová* **CRYSTALLIZATION KINETICS OF Er:LiY$(PO_3)_4$ GLASS**
15:00 – 15:20	*Z. Kožíšek* **KINETICS OF NUCLEATION ON HIGHLY CURVED SURFACES**
15:20 – 15:40	*Z. Onderišinová* **GROWTH AND CHARACTERIZATION OF GARNET SCINTILLATION EPITAXIAL FILMS DOPED BY RARE-EARTH IONS**
15:40 – 16:10	**COFFEE BREAK**
CHAIRMAN	**K. Nitsch**
16:10 – 16:30	*R. Král* **STUDY OF GROWTH CONDITIONS INFLUENCE ON SHAPE AND POSITION OF CRYSTAL/MELT INTERFACE DURING CRYSTAL GROWTH OF TERNARY HALIDES BY VERTICAL BRIDGMAN METHOD**
16:30 – 16:50	*Z. Kožíšek* **CRYSTAL NUCLEATION AND GROWTH ON HETEROGENEOUS SURFACE**
16:50 – 17:10	*V. Bouda* **FRACTAL GROWTH IN COMPARISON WITH CRYSTAL GROWTH**

DINNER…… 18:00

EVENING PROGRAMME:
WELCOME PARTY……. 19:30

Tuesday, August 30, 2011

BREAKFAST……. 08:00

LECTURES

CHAIRMAN	**J. Lipták**
09:00 – 09:20	*K. Rubešová* **WATER BASED SOL-GEL METHODS USED AT Bi-Sr-Co-O THERMOELECTRICS SYNTHESIS**
09:20 – 09:40	*V. Jakeš* **LITHIUM NIOBATE PREPARED BY SOL-GEL METHODS AS TARGETS FOR PULSED LASER DEPOSITION**
09:40 – 10:00	*P. Kostelník* **ANISOTROPIC ETCHING OF SILICON BY TMAH**
10:00 – 10:30	
CHAIRMAN	**Z. Kožíšek**
10:30 – 10:50	*J.A. Mareš* **Pr^{3+}-DOPED ALUMINUM GARNET CRYSTALS AND LAYERS**
10:50 – 11:10	*J. Lipták* **IMPENDANCE AND CONDUCTIVITY ANALYSIS OF POLYSTYRENE-CARBON BLACK COMPOSITES**
11:10 – 11:30	*M. Sahul* **LASER WELDING OF DISSIMILAR STEELS**
11:30 – 11:50	*R. Yatskiv* **GRAPHITE BASED SCHOTTKY DIODES**
11:50 – 12:10	*Z. Bureš* **STABILISATION OF METALLIC NANOPARTICLES**

LUNCH…… 12:30

LECTURES

CHAIRMAN	**J. Sedláček**
14:00 – 14:30	*J. Maršík* **DEVELOPMENT TRENDS OF SMALL MOLECULE X-RAY DIFFRACTION SYSTEMS**
14:30 – 14:50	*K. Kolařík* **X-RAY DIFFRACTION AND BARKHAUSEN NOISE ANALYSIS FOR INVESTIGATION OF REAL STRUCTURE CHANGES FOR CAR INDUSTRY COMPONENTS**
14:50 – 15:10	*I. Rösslerová* **STRUCTURE AND PROPERTIES OF LEAD BOROPHOSPHATE GLASSES DOPED BY MOLYBDENUM OXIDE**
15:10 – 15:30	*P. Mošner* **STRUCTURE AND PROPERTIES OF PbO-TeO_2-P_2O_5 GLASSES**
15:30 – 16:00	**COFFEE BREAK**
CHAIRMAN	**P. Mošner**
16:00 – 16:20	*L. Válek* **MACROSCOPIC SIGNS OF CRYSTAL STRUCTURE**
16:20 – 16:40	*Z. Potůček* **PHOTOLUMINISCENCE OF CHROMIUM DOPED $SrTiO_3$ POWDERS**
16:40 – 17:00	*J. Sedláček* **DIELECTRIC PROPERTIES OF BARIUM TITANATE PREPARED BY SPARK PLASMA SINTERING**

DINNER…… 18:00
FREE EVENING

Wednesday, August 31, 2011

BREAKFAST……. 08:00

PANEL DISCUSSION
AND
JOINT MEETING OF THE
SLOVAK EXPERT GROUP OF SOLID STATE CHEMISTRY AND PHYSICS
AND
CZECH AND SLOVAK ASSOCIATION FOR CRYSTAL GROWTH

DINNER…… 18:00

Thursday, September 1, 2011

BREAKFAST……. 08:00

LECTURES

CHAIRMAN	**M. Martinkovič**
09:00 – 09:20	*J. Luňáček* **SIMULATION OF A SURFACE PLASMON RESONANCE-BASED FIBER-OPTIC REFRACTIVE INDEX SENSOR**
09:20 – 09:40	*M. Luňáčková* **SIMULATION OF A SURFACE PLASMON RESONANCE-BASED REFRACTIVE INDEX SENSOR USING SPECTRAL INTERFERENCE**
09:40 – 10:00	*I. Pilarčíková* **ANALOG AND NUMERICAL MODELING THE CONSTRICTION PHENOMENON ON COMPOSITES WITH CONDUCTIVE CARBON PARTICLES**
10:00 – 10:30	**COFFEE BREAK**
CHAIRMAN	**J. Luňáček**
10:30 – 10:50	*M. Pašák* **POSSIBILITY OF THERMODYNAMIC MODELLING OF PHASE TRANSFORMATIONS IN TOOL STEELS**
10:50 – 11:10	*V. Kucek* **INFLUENCE OF NONSTOICHIOMETRY ON THE TRANSPORT PROPERTIES OF THE GaGeTe COMPOUND**

11:10 – 11:30	*M. Martinkovič* **MEASUREMENT POSSIBILITIES OF MECHANICAL PROPERTIES OF SOLDERED JOINTS**
11:30 – 11:50	*J. Gutwirth* **DATA STORAGE - CURRENT AND APPROACHING TECHNOLOGIES, PHYSICAL PRINCIPLES & USED MATERIALS**

LUNCH…… 12:30

LECTURES

CHAIRMAN	**M. Rodová**
14:00 – 14:20	*B. Papánková* **MATERIALS SCIENCE AND ENGINEERING —TRENDS AND ISSUES**
14:20 – 14:40	*L. Dlháň* **SQUID MAGNETIC STUDIES OF BASAL GANGLIA EXTRACTED FROM HUMAN BRAIN**
14:40 – 15:00	*V. Jorík* **IS THE CRYSTAL STRUCTURE DETERMINATION FROM POWDER SAMPLE USEFUL FOR "COORDINATION" CHEMIST?**
15:00 – 15:20	*M. Koman* **NEW COORDINATION COMPOUNDS OF Cu(II) WITH PYRIDYLMETHANOLS**
15:20 – 15:50	**COFFEE BREAK**
16:00	**CLOSING**

EVENING PROGRAMME:
FAREWELL PARTY……..…….. 19:30

Friday, September 2, 2011

BREAKFAST……. 08:00

DEPARTURE (*individual)*……...…….. 09:00

Programming Committee is authorized to necessary changes in the time table.

AUTHORS INDEX

REMARKS

REMARKS

REMARKS